

Department of Physics and Astronomy

University of Heidelberg

Master thesis

in Physics

submitted by

Lukas Gerhard Gerritzen

born in Offenbach am Main

2017

**Reconstruction of Two-Prong Signatures
with a Linearised Multiple Scattering
Vertex Fit for Mu3e**

This Master thesis has been carried out by

Lukas Gerritzen

at the

Institute of Physics

under the supervision of

Prof. André Schöning

“The Answer to the Great Question
of Life, the Universe and Everything
is...

Photon Conversion Electrons.”

Reconstruction of Two-Prong Signatures with a Linearised Multiple Scattering Vertex Fit for Mu3e:

The goal of this study is the development of an algorithm for the reconstruction of two-prong signatures in the Mu3e detector.

The Mu3e detector is an electron spectrometer designed to search for the charged lepton flavour violating (cLFV) decay $\mu^+ \rightarrow e^+e^-e^+$. Four cylindrical layers of thin silicon pixel sensors are used to track electrons and positrons.

In addition, the detector can be used to search for other processes such as the cLFV decay $\mu^+ \rightarrow e^+\gamma$ and the neutral pion Dalitz decay $\pi^0 \rightarrow e^+e^-\gamma$ if the photon can be reconstructed. For this, the photon needs to convert to an e^+e^- pair.

A linearised vertex fit based on a multiple Coulomb scattering model is used in the scope of this thesis to reconstruct vertices of simulated photon conversion events from two oppositely charged electron tracks.

Despite the narrow opening angles of the two tracks, fit convergence in over 95 % of the cases is achieved. The vertex resolution parallel to the photon momentum is in the order of up to 3 mm, while the resolution perpendicular to the photon momentum is well below 100 μm . The direction of the photon can be reconstructed with an uncertainty of about 10 mrad.

By application of the algorithm to the primary e^+e^- pairs from Dalitz decays, a resolution of the invariant mass of about 1.6 MeV is achieved. Measurements of the invariant mass spectrum can be used to improve theoretical predictions of the anomalous magnetic moment of the muon and to search for massive dark photons.

This master thesis demonstrates that the reconstruction of two-prong signatures is feasible with high precision using a multiple scatteringvertex fit, which has a wide range of applications in precision measurements and searches for physics beyond the standard model that can be performed using the Mu3e detector.

Rekonstruktion von Zwei-Spur-Signaturen mit einem linearisierten Vertexfit basierend auf Mehrfachstreuung für Mu3e:

Das Ziel dieser Studie ist die Entwicklung eines Algorithmus für die Rekonstruktion von Zwei-Spur-Signaturen im Mu3e-Detektor.

Der Mu3e-Detektor ist ein Elektronenspektrometer, das für die Suche nach dem Lepton-Familienzahl (LF) verletzenden Zerfall $\mu^+ \rightarrow e^+e^-e^+$ entwickelt wird. Vier zylindrische Lagen dünner Siliziumpixelsensoren werden verwendet, um Elektronen und Positronen zu detektieren.

Zusätzlich kann der Detektor genutzt werden, um nach weiteren Prozessen wie dem LF-verletzenden Zerfall $\mu^+ \rightarrow e^+\gamma$ und dem Dalitz-Zerfall des neutralen Pions $\pi^0 \rightarrow e^+e^-\gamma$ zu suchen, falls das Photon rekonstruiert werden kann. Dazu muss das Photon in ein e^+e^- -Paar konvertieren.

In dieser Arbeit wird ein linearisierter Vertexfit basierend auf einem Modell der Mehrfachstreuung verwendet, um Vertices von simulierten Photonkonversionsereignissen aus zwei Elektronenspuren zu rekonstruieren.

Trotz des kleinen Öffnungswinkels der beiden Spuren wird eine Konvergenz des Fits in über 95 % der Fälle erreicht. Die Vertexpföfung entlang der Photonrichtung ist in der Größenordnung von bis zu 3 mm, während die Auflösung senkrecht zum Photonimpuls deutlich unter 100 μm liegt. Die Richtung des Photons kann mit einer Unsicherheit von etwa 10 mrad rekonstruiert werden.

Mit Hilfe des Algorithmus lässt sich die invariante Masse von primären e^+e^- -Paaren aus Dalitzzerfällen mit einer Auflösung von ungefähr 1.6 MeV rekonstruieren. Messungen des Spektrums der invarianten Massen können verwendet werden, um die theoretische Vorhersage des anomalen magnetischen Moments des Myons zu verbessern und um nach massiven dunklen Photonen zu suchen.

Diese Masterarbeit demonstriert, dass die Rekonstruktion von Zwei-Spur-Signaturen mit Hilfe eines Vertexfits basierend auf Mehrfachstreuung möglich ist. Diese Rekonstruktion hat zahlreiche Anwendungen für Präzisionsmessungen und die Suche nach Physik jenseits des Standardmodells, die mit dem Mu3e-Detektor möglich sind.

Contents

I. Introduction	1
1. Introduction	3
2. Theory	5
2.1. Standard Model of Particle Physics	5
2.2. Muon Physics	7
2.2.1. Muon Decays	7
2.2.2. Anomalous Magnetic Moment of the Muon	8
2.3. Neutral Pion Physics	9
2.3.1. Charge Exchange Reaction	9
2.3.2. Dalitz Decay	10
2.4. Photon Conversion	11
3. The Mu3e Experiment	13
3.1. The Decay $\mu \rightarrow eee$	13
3.1.1. Standard Model Channel	14
3.1.2. Beyond Standard Model Channels	14
3.1.3. Kinematics of $\mu \rightarrow eee$	14
3.1.4. Backgrounds	15
3.2. Photons in Mu3e	16
3.3. The Mu3e Detector	18
3.3.1. Stopping Target	19
3.3.2. Pixel Tracker	19
3.3.3. Timing Detector	20
3.3.4. Data Acquisition	20
3.4. Possible Modifications to the Mu3e Experiment	21
3.4.1. Mu3e-Gamma	21
3.4.2. Neutral Pions at PSI	22
3.5. Track Reconstruction	23

4. The Multiple Scattering Vertex Fit	27
4.1. Introduction	27
4.2. Coordinate System	28
4.3. Multiple Coulomb Scattering	28
4.4. Least Squares Method	30
4.4.1. The Error Matrix	32
4.5. Initial Vertex Finding	33
II. Studies	35
5. Photon Studies	37
5.1. Simulation and Reconstruction	38
5.2. General Challenges	39
5.3. Chi-squared in Space	40
5.3.1. Orientation of the Error Ellipsoid	40
5.3.2. Chi-squared Maps	41
5.3.3. Existence of a Second Minimum	41
5.4. Photon Vertex Fit Studies	42
5.4.1. Convergence	42
5.4.2. Number of Steps and Correction Size	47
5.4.3. Resolutions	48
5.4.4. Spatial Resolution	49
5.4.5. Angular Resolution	54
5.4.6. Energy Resolution	55
5.4.7. Invariant Mass Resolution	57
5.4.8. Chi-squared Revisited	58
5.4.9. Summary	59
5.5. Photons from Muon Decays in $\text{Mu}3e$	61
5.5.1. Geometrical Acceptance for Radiative Decays	61
5.5.2. Bhabha Scattering Background	62
5.5.3. Internal Conversion Background	63
6. Dalitz Decay Studies	65
6.1. Simulation	65
6.2. Acceptance for Dalitz Decays	66
6.2.1. Geometric Acceptance of the Electron-Positron Pair	66
6.2.2. Acceptance Including Photons	67
6.3. Dalitz Pair Vertex Fit	68
6.3.1. Vertex Resolution	68
6.3.2. Invariant Mass	69

6.4. Reconstruction of Pion Decays	70
6.5. Signal vs. Background	71
6.6. Conclusion	73
III. Discussion	75
7. Discussion	77
7.1. Summary and Discussion	78
7.2. Outlook	79
IV. Appendix	83
A. Additional Calculations for the Vertex Fit	85
A.1. Calculating the Scattering Angles	85
A.1.1. Transverse Scattering	85
A.1.2. Longitudinal Scattering	87
A.2. First Derivatives of Scattering Angles	88
B. Additional Figures for Photons	91
C. Additional Figures for Dalitz Pairs	97

Part I.

Introduction

1. Introduction

With the discovery of neutrino oscillation, lepton flavour violation (LFV) has been observed in the neutral lepton sector. In the past, several experiments have searched for lepton flavour violation in the charged sector (cLFV), but cLFV has not been observed to date.

The primary goal of the Mu3e experiment at *Paul Scherrer Institute* (PSI) in Villingen, Switzerland is the search for the cLFV decay $\mu^+ \rightarrow e^+e^-e^+$ with an unprecedented sensitivity of one in 10^{16} muon decays [1].

Four barrel-shaped layers of pixel sensors and two timing detector systems are used to track electrons⁽¹⁾ originating from the target region. The Mu3e detector is optimised for electrons with energies up to half the muon mass $m_\mu/2 \approx 53 \text{ MeV}$ ⁽²⁾. Electrons with transverse momenta of less than about 10 MeV will not reach the outermost pixel layer and cannot be reconstructed.

Although Mu3e has been designed with a very specific goal in mind, a wide range of other searches and studies can be performed using Mu3e's electron tracking capabilities. Many searches require reconstruction of events with two tracks. This thesis focuses on the reconstruction of two-prong events in the Mu3e detector, namely electron-positron pairs from photon conversion and Dalitz decays. Photons in Mu3e can only be detected when they convert to an electron-positron pair. To find the conversion vertex, a linearised vertex fit based on multiple scattering is used. The same linearised fit is also performed on the e^+e^- pair from the pion decay. Multiple approaches to combine these pairs with reconstructed photons are discussed.

In the scope of this thesis it was possible to demonstrate that the direction and

⁽¹⁾In this thesis, the term *electron* is used for both the negative electron e^- and its antiparticle, the positron e^+ . If necessary, the charge is explicitly mentioned. The same applies to all other elementary particles.

⁽²⁾When appropriate, natural units are used in this thesis, setting $\hbar = c = 1$.

1. Introduction

energy of photons can be reconstructed with a high precision. The lateral vertex position can also be determined with a high precision, only the position along the photon direction has uncertainties of the order of millimetres.

2. Theory

2.1. Standard Model of Particle Physics

The Standard Model of particle physics (SM) describes matter particles (fermions) and all their interactions mediated by bosons, except gravitation. The fermions of the SM consist of quarks and leptons, which come in six flavours each, and their antiparticles. The electromagnetic interaction between electrically charged particles is mediated by photons. The strong interaction that confines quarks in hadrons is described by quantum chromodynamics with eight gluons as the force carriers. All fermions interact weakly. The weak interaction, responsible e.g. for the beta decay of radioactive nuclei, is mediated by charged and neutral currents with the massive W^\pm and Z^0 bosons. Furthermore, the Higgs mechanism and the associated Higgs boson are responsible for the masses of the W and Z bosons and

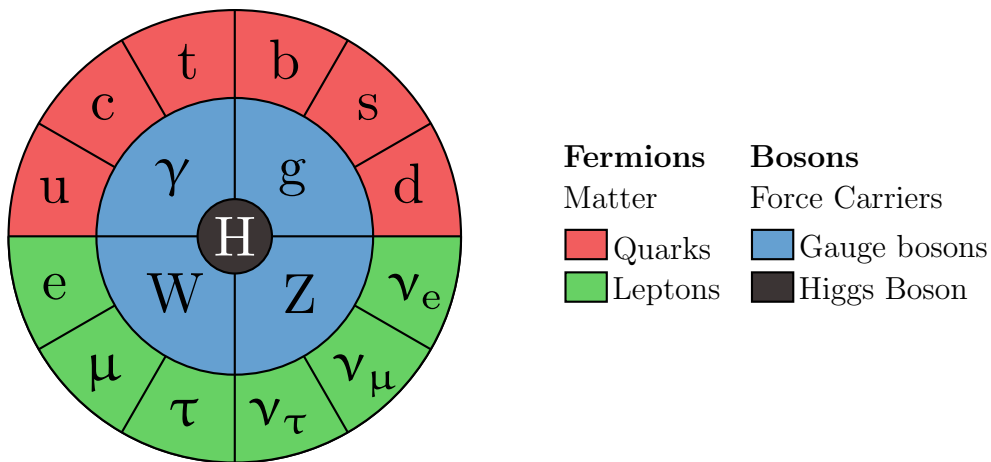


Figure 2.1.: Representation of the SM particles. For each fermion f , there exists a corresponding antifermion \bar{f} . The W boson comes either with positive or negative charge. Adapted from [2].

2. Theory

the fundamental fermions. The particles of the SM are presented in figure 2.1.

Quark and lepton flavours are conserved by both the electromagnetic and the strong interaction, only the charged current of the weak interaction breaks the corresponding symmetry. In the case of quark flavour, the flavour violation is described by the Cabibbo–Kobayashi–Maskawa matrix which allows for quark mixing.

In the case of leptons, only transitions between a lepton ℓ and its corresponding neutrino ν_ℓ are possible via the weak interaction (and the same for antileptons $\bar{\ell}$ and their antineutrinos $\bar{\nu}_\ell$). Therefore, not only the total lepton number L is conserved, but also the lepton family number for each of the three generations: L_e , L_μ and L_τ , where $L_\ell = 1$ for negative leptons ℓ^- and neutrinos ν_ℓ . Antileptons ℓ^+ and antineutrinos $\bar{\nu}_\ell$ carry negative lepton family numbers $L_\ell = -1$.

The observation of neutrino oscillation [3–5] shows that the lepton family numbers are not conserved for neutrinos. Neutrino mixing is possible if the SM is modified to allow nonzero neutrino masses. This modification is sometimes called ν SM. The ν SM relates the three weak neutrino eigenstates to the mass eigenstates by the Pontecorvo–Maki–Nakagawa–Sakata matrix.

However, there are observations which cannot be explained by such a modification to the SM. Only about 5% of the energy-matter in the universe is baryonic matter. Another 23% is in the form of cold dark matter for which the ν SM offers no description or particle candidate. The remaining 72% are in the form of dark energy, also not explained by the ν SM [6]. Furthermore, gravitation cannot be expressed as a renormalisable quantum field theory and is therefore not included in the ν SM. Another open issue is the unexplained imbalance in baryonic matter and antibaryonic matter. No SM process allows baryogenesis, i.e. the production of the observed unequal amount of baryons and antibaryons.

The existence of these unexplained phenomena motivates the search for physics beyond the SM (BSM) either by searches for possible new heavy particles produced in high energy collisions or by precision tests of the SM.

2.2. Muon Physics

With a mass of $m_\mu = 105.658\,374\,5(24)$ MeV [7], the muon is the second lightest charged lepton. Its mean lifetime is $\tau = 2.196\,981\,1(22)$ μs . In the context of Mu3e, antimuons are considered rather than muons, but the properties are valid for both the muon and the antimuon if one exchanges particles and antiparticles in the decays.

2.2.1. Muon Decays

The muon decays predominantly via the Michel decay $\mu^+ \rightarrow e^+ \bar{\nu}_\mu \nu_e$ with a branching ratio of nearly 100%. The radiative decay with an additional photon in the final state is the second most common decay mode with a branching fraction of $\mathcal{BR} = (1.4 \pm 0.4) \times 10^{-2}$ for a photon energy $E_\gamma > 10$ MeV and $\mathcal{BR} = (3.3 \pm 1.3) \times 10^{-3}$ for $E_\gamma > 20$ MeV [7]. With a small probability, this photon is created off-shell and converts internally. The branching fraction of this radiative decay with internal conversion is $\mathcal{BR} = (3.4 \pm 0.4) \times 10^{-5}$ [7]. These three decays are shown in figure 2.2.

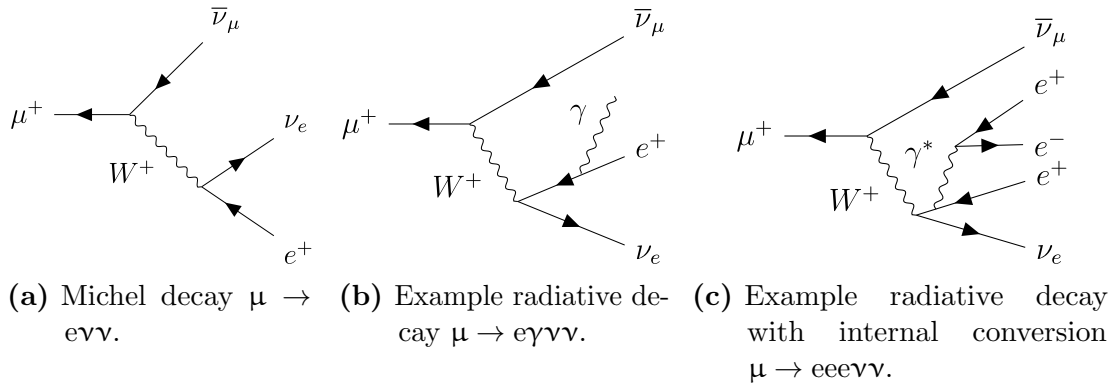


Figure 2.2.: Leading-order Feynman diagrams for the three most common muon decays.

2. Theory

2.2.2. Anomalous Magnetic Moment of the Muon

According to Dirac theory, the magnetic moment \vec{M} of the muon is

$$\vec{M} = g \frac{q}{2m_\mu} \vec{S} \quad (2.1)$$

where \vec{S} is the spin, q is the electric charge, and m_μ is the muon mass. The gyromagnetic ratio g is predicted to be exactly 2 by the Dirac equation [6]. When considering quantum loop effects, a small deviation from $g = 2$ can be calculated, commonly parameterised by the anomalous magnetic moment, in the case of the muon

$$a_\mu = \frac{g - 2}{2}. \quad (2.2)$$

The SM prediction can be divided into three parts. Photonic and leptonic loops contribute to a_μ^{QED} , loops containing heavy W^\pm , Z and Higgs bosons are summarised in the electroweak part a_μ^{EW} and hadronic contributions involving quarks and gluons are taken into account by the hadronic part a_μ^{Had} :

$$a_\mu^{\text{SM}} = a_\mu^{\text{QED}} + a_\mu^{\text{EW}} + a_\mu^{\text{Had}}. \quad (2.3)$$

The main theoretical uncertainty of a_μ^{SM} arises from the hadronic part a_μ^{Had} , which cannot be calculated from first principles [8]. The hadronic part itself can be divided into three parts: leading order (LO) and higher order (HO) vacuum polarisation (VP) contributions as well as light-by-light (LBL) scattering contributions:

$$a_\mu^{\text{Had}} = a_\mu^{\text{Had,LO VP}} + a_\mu^{\text{Had,HO VP}} + a_\mu^{\text{Had,LBL}}. \quad (2.4)$$

Currently, measurements of $g - 2$ disagree with theoretical predictions with a significance of 3.4σ [7]. This discrepancy hints at BSM physics and can be explained by several models involving supersymmetric particles or *dark photons*, light vector bosons that mainly couple to dark matter but could also couple to matter via kinetic mixing with the photon [9]. To obtain more conclusive results, more precise measurements of a_μ and better theoretical predictions are necessary.

The current SM prediction a_μ^{SM} and world average a_μ^{exp} are

$$a_\mu^{\text{SM}} = 1\,165\,917.63(46) \times 10^{-9}, \quad (2.5)$$

$$a_\mu^{\text{exp}} = 1\,165\,920.91(63) \times 10^{-9}. \quad (2.6)$$

2.3. Neutral Pion Physics

The neutral pion is the lightest meson ($m_{\pi^0} = 134.9766(6)$ MeV) [7] and decays almost instantly ($\tau = 8.52(18) \times 10^{-17}$ s) via the electromagnetic interaction. With $\mathcal{BR}(\pi^0 \rightarrow \gamma\gamma) \approx 98.82\%$ the decay to two photons is dominant.

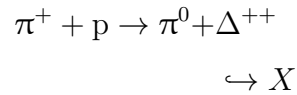
2.3.1. Charge Exchange Reaction

Because of their short lifetime, neutral pions have to be produced directly in the detector to study them. The most commonly used process is the charge exchange reaction (CEX) of a negative pion that is stopped in a target with an abundance of protons (typically liquid hydrogen):



About 60% of the stopped pions in a liquid hydrogen target produce a neutral pion [10]. Since this is a two-body reaction, the kinematics are fixed with final state momenta of 28.5 MeV in opposite directions. In the case of radiative capture $\pi^- + \text{p} \rightarrow \text{n} + \gamma$, a highly energetic photon is emitted.

Another way to create neutral pions is via the production of delta baryons using a high-energetic positive pion.



Due to the high mass of the delta baryon of 1232 MeV, the positive pion beam needs a momentum of more than 497 MeV. The pions are not stopped in the detector. However, the cross section is small compared to the 60% π^0 production

2. Theory

with CEX. The produced Δ^{++} baryons decay into nucleons and pions which are a source of background avoided by CEX.

2.3.2. Dalitz Decay

The second most common decay of the neutral pion with a branching fraction of $\mathcal{BR} \approx 1.17\%$ [7] is the Dalitz decay $\pi^0 \rightarrow e^+e^-\gamma$ shown in figure 2.3a. One of the two photons is created off-shell and converts internally to an electron-positron pair.

Commonly used kinematic variables for the Dalitz decay are [11]

$$x = \left(\frac{M_{ee}}{m_{\pi^0}}\right)^2 = \frac{(p_{e^+} + p_{e^-})^2}{m_{\pi^0}^2} \quad \text{and} \quad y = \frac{2p_{\pi^0}(p_{e^+} - p_{e^-})}{m_{\pi^0}^2(1-x)}, \quad (2.8)$$

where M_{ee} is the invariant mass of the e^+e^- system and p_{π^0}, p_{e^+} and p_{e^-} are the four-momenta of the respective particles. The physical constraints on x and y are given by

$$r^2 = \left(\frac{2m_e}{m_{\pi^0}}\right)^2 \leq x \leq 1, \quad |y| \leq \sqrt{1 - \frac{r^2}{x}}. \quad (2.9)$$

Normalised to the decay width of the dominant decay $\Gamma(\pi_{2\gamma}^0)$, the Dalitz decay width has the following form [12]:

$$\frac{d^2\Gamma(\pi_D^0)}{dx dy} = \frac{\alpha}{4\pi} \Gamma(\pi_{2\gamma}^0) \frac{(1-x)^3}{x} \left(1 + y^2 + \frac{r^2}{x}\right) (1 + \delta(x, y)) |\mathcal{F}(x)|^2, \quad (2.10)$$

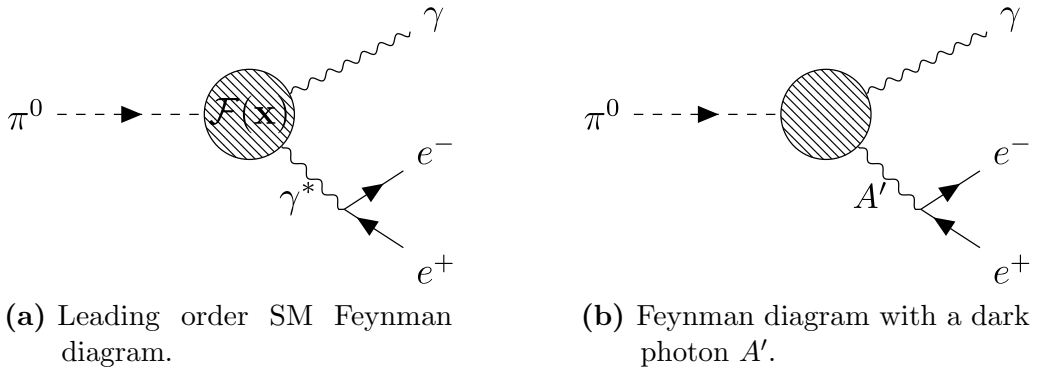


Figure 2.3.: Two Feynman diagrams for the decay $\pi^0 \rightarrow e^+e^-\gamma$.

where $\delta(x, y)$ accounts for radiative corrections and $\mathcal{F}(x)$ is the semi-off-shell electromagnetic transition form factor (TFF) of the π^0 .

This TFF weakly depends on the kinematic variable x and is therefore commonly described with a linear approximation $\mathcal{F}(x) \approx 1 + ax$ with the slope parameter a . Among other calculations, the TFF enters into the hadronic light-by-light contribution to the anomalous magnetic moment of the muon $g-2$ (see section 2.2.2). The value of the TFF slope is $a = 0.032(4)$ [7] and can be measured from Dalitz decays via reconstruction of the kinematic variable x [11]. Therefore, improved TFF measurements with Dalitz decays would reduce the uncertainty of the predictions for $g - 2$.

Measurements of the Dalitz decay of the neutral pion are also suited for other searches for new physics. For example, the γ^* in the Dalitz decay could be replaced by a massive dark photon (see figure 2.3b). This would produce a bump in the invariant mass spectrum of the e^+e^- system. A similar search by the NA48/2 collaboration has resulted in new exclusion limits in the mass range of the dark photon $9 \text{ MeV} < m_{A'} < 70 \text{ MeV}$ [13]

2.4. Photon Conversion

The dominant interaction of high-energy photons ($E_\gamma \gg m_e$) with matter is the conversion to an electron-positron pair. Conversion in the Coulomb field of electrons is heavily suppressed compared to conversion in the field of nuclei.

The radiation length X_0 is a material constant and describes the mean distance over which an electron's energy is reduced to $1/e$ by Bremsstrahlung. It is also related to the mean free path λ of pair production of photons [6]:

$$X_0 = \frac{7}{9} \lambda. \quad (2.11)$$

The electron and positron created by photon conversion do not necessarily have the same kinetic energy. In fact, the distribution of the energy-partition parameter $x = E_+^{\text{kin}}/E_{\text{pair}}^{\text{kin}}$ is almost uniform in the energy range of photons in Mu3e of $E_\gamma < 53 \text{ MeV}$ (see figure 2.4). E_+^{kin} denotes the kinetic energy of the positron and $E_{\text{pair}}^{\text{kin}}$ denotes the kinetic energy of the electron-positron pair.

2. Theory

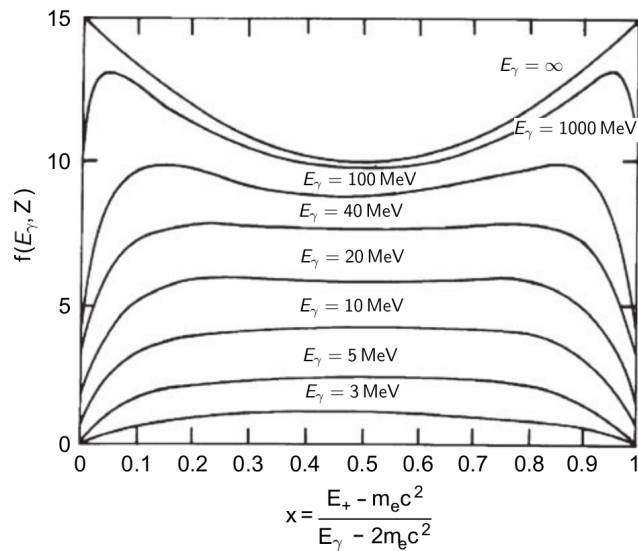


Figure 2.4.: Energy-partition function $f(E_\gamma, Z)$ with the atomic number Z and the photon energy E_γ as parameters as a function of x . The total cross section can be obtained by multiplying the area under the curve with $Z(Z+1)\alpha r_e^2$ where α is the fine structure constant and r_e is the classical electron radius [14] (modified).

The opening angle between electron and positron is generally small with a characteristic opening angle of $\Theta \approx m_e/E_\gamma$ [14].

3. The Mu3e Experiment

The Mu3e experiment has been designed for the search for the cLFV decay of an antimuon into two positrons and an electron. A previous search by the SINDRUM collaboration published in 1988 has resulted in an upper limit for the branching ratio of 1.0×10^{-12} (90% CL) [15]. The goal for Mu3e is a single event sensitivity of 2×10^{-15} in phase I and 1×10^{-16} in phase II of the experiment [1]. To achieve these goals in a reasonable amount of time, a high-rate muon beam is needed.

For phase I, a muon rate of up to 10^8 s^{-1} is provided by the $\pi\text{E}5$ beam line at PSI. To reach the aimed sensitivity, a run time of $2.5 \times 10^7 \text{ s}$ (290 days) is required. Higher rates require a new beamline currently under study by the HiMB (*high intensity muon beam*) project [16].

For well-defined kinematics of the decays, the muons are stopped on a target where they decay at rest. One of the main challenges is multiple Coulomb scattering (MS) of decay electrons in the detector material, which limits the momentum resolution. To minimise the amount of MS, a low material budget inside the detector is required.

This chapter provides an overview over the decay $\mu \rightarrow eee$ and the expected backgrounds, the detector design and briefly discusses possible modifications to the detector.

3.1. The Decay $\mu \rightarrow eee$

In order to achieve the desired sensitivity, backgrounds need to be suppressed below that level. Therefore, the signatures of signal and background events must be well understood.

3. The Mu3e Experiment

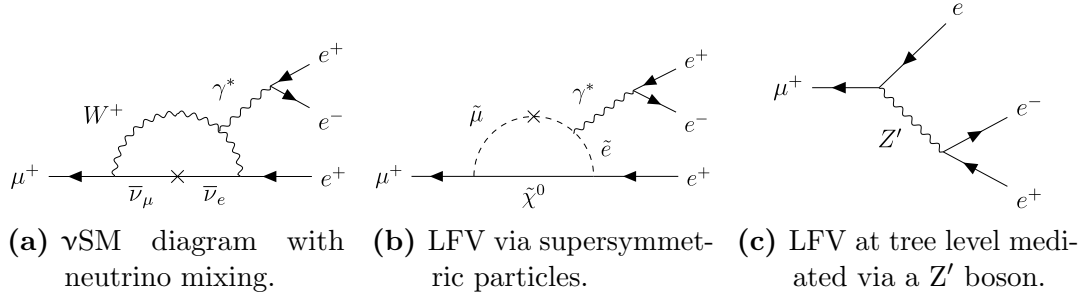


Figure 3.1.: Different Feynman diagrams for the decay $\mu^+ \rightarrow e^+e^-e^+$.

3.1.1. Standard Model Channel

In the ν SM, cLFV decays are only allowed via loops as shown in figure 3.1a. This process is suppressed with a branching ratio $\mathcal{BR} < 10^{-54}$ [17] and cannot be observed in the Mu3e experiment since the sensitivity is still many orders of magnitude above the branching ratio. Therefore, any observation would be the discovery of a physics process not described by the ν SM.

3.1.2. Beyond Standard Model Channels

Several theories predict cLFV in experimentally observable occurrences. Examples are grand unified models, models with an extended Higgs sector and supersymmetric models [18]. Two exemplary processes are shown in figure 3.1b and 3.1c.

3.1.3. Kinematics of $\mu \rightarrow eee$

The following characteristics of the decay $\mu^+ \rightarrow e^+e^-e^+$ are used to separate it from background processes.

- **Momentum conservation in muon decay at rest.**

The momenta of all decay particles add up to zero: $\sum_i \vec{p}_i = 0$.

- **Energy conservation in the muon decay.**

The energies of all decay particles add up to the rest mass of the muon:

$$\sum_i E_i = m_\mu.$$

- **All decay particles have the same origin.**

A common vertex for all three particle tracks can be found and they are

emitted in time coincidence.

Background events violate some or all of these criteria.

3.1.4. Backgrounds

There are two types of background in Mu3e: accidental background due to superposition of different processes, and muon decays with three electrons among other particles in the final state (irreducible background).

Accidental Background

Particles from a combination of unrelated processes can mimic the $\mu \rightarrow eee$ signal of two positrons and one electron. The probability of these coincidental overlays increases with higher muon rates.

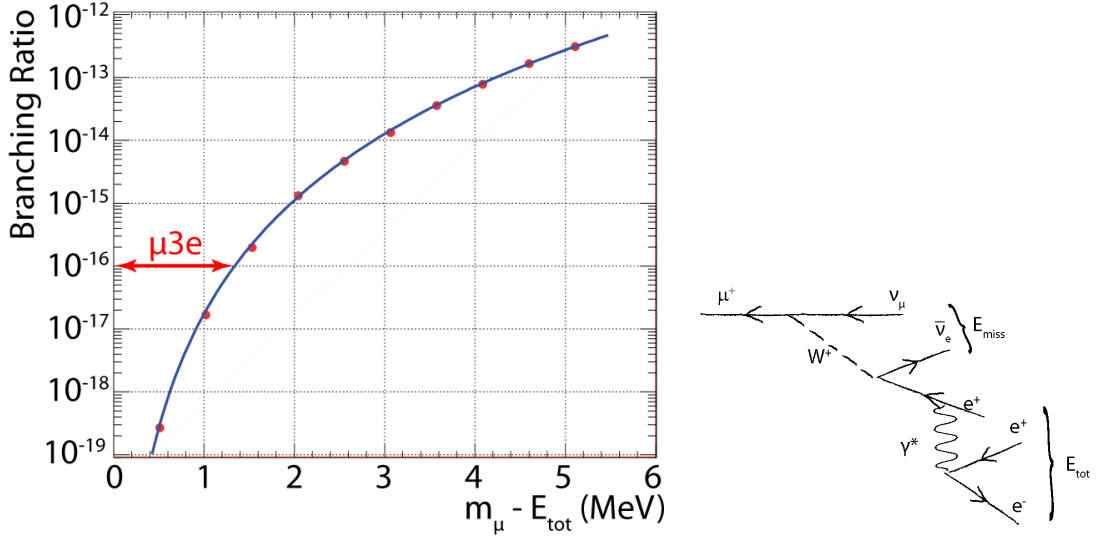
With a positive muon beam, there is an abundance of positrons from the Michel decay. Sources for (negative) electrons are Bhabha scattering of positrons with electrons in the stopping target and interactions of photons with the target material (Compton scattering and photon conversion). These effects can be reduced by minimising the material budget of the stopping target. Furthermore, three generic tracks from these processes do not have a common vertex and are not generally coincident in time. Misreconstruction of either positron tracks that are reconstructed backwards or hits that were not produced by the same particle, can also mimic electron tracks.

Therefore, a good vertex and timing resolution can suppress accidental backgrounds. The vertex resolution is limited by the amount of multiple Coulomb scattering in the target material and at the innermost pixel layer [19]. Also, a larger distance between the target and the detector layers worsens the vertex resolution.

Radiative Decay With Internal Conversion

The other source of background is the radiative muon decay with internal conversion $\mu^+ \rightarrow e^+ \bar{\nu}_\mu \nu_e (\gamma^* \rightarrow e^+ e^-)$ shown in figure 3.2b (see also section 2.2.1). The three tracks from this decay have the same vertex and are coincident. As shown in figure 3.2b, some energy leaves the detector in the form of the undetected neutrinos

3. The Mu3e Experiment



(a) For small missing energies $m_\mu - E_{\text{tot}}$ the branching ratio for the decay $\mu \rightarrow eee\nu\nu$ is heavily suppressed [20]. (b) Feynman diagram for the radiative muon decay with internal conversion.

Figure 3.2.: The total energy E_{tot} is the energy that can be reconstructed from the electrons. The missing energy E_{miss} gets carried away by the neutrinos and is not detectable.

(missing energy). Therefore, the sum of the reconstructed electron energies is less than the muon rest mass $\sum_i E_i = E_{\text{tot}} < m_\mu$.

A good energy resolution is needed to suppress this background. The branching ratio for this decay is small for small missing energies (see figure 3.2a). For missing energies $m_\mu - E_{\text{tot}}$ smaller than five times the electron mass, the cumulative branching ratio is $4.660(46) \times 10^{-15}$ [20], which is still larger than the sensitivity goal of Mu3e.

3.2. Photons in Mu3e

Photons need to convert to a pair of an electron and a positron that each carry a transverse momentum large enough to reach the outermost detector layer to be reconstructed. In the following, several processes creating photons in Mu3e are described. Most of these photons are low-energetic, though, and cannot produce

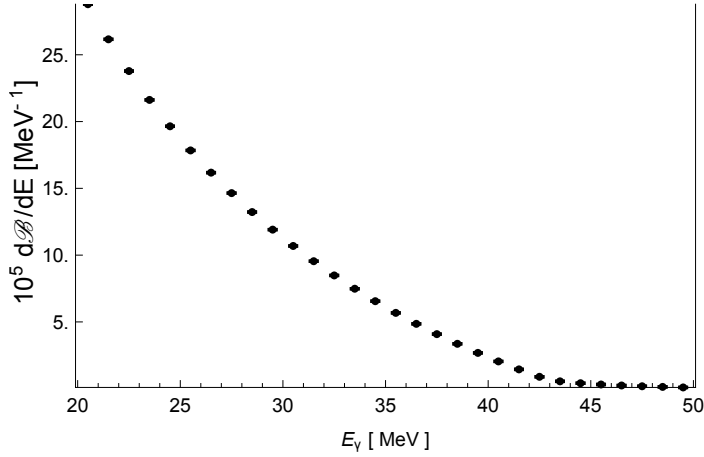


Figure 3.3.: Next-to-leading order calculations for branching ratio for the radiative muon decay with respect to the photon energy. A muon polarisation of 85% is assumed, cuts on the electron energy of $E_e > 10$ MeV and a on the polar angle of the photon of $\cos(\theta) < 0.8$ are applied. The branching ratio is exclusive (exactly one photon is visible).

By courtesy of Yannick Ulrich (personal communication, March 2017 and [21]).

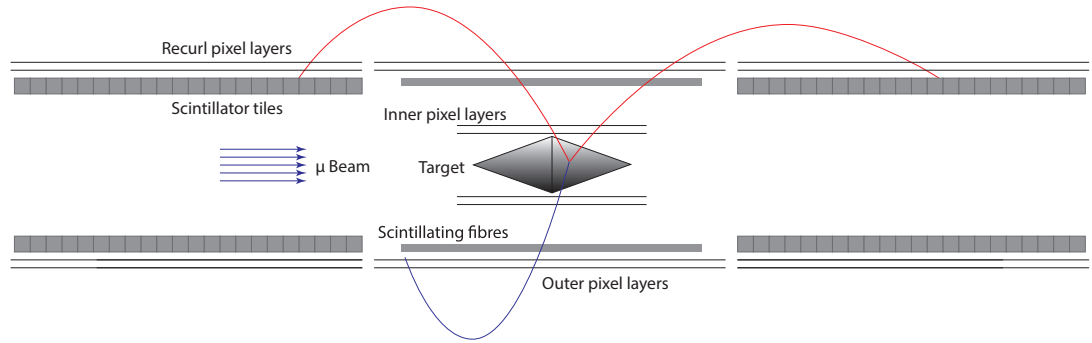
two reconstructable daughter electrons.

The main source of high-energy photons in Mu3e is the radiative muon decay $\mu^+ \rightarrow e^+ \nu_e \bar{\nu}_\mu \gamma$ (see also section 2.2.1). As shown in figure 3.3, most photons from the radiative decay only carry little energy E_γ .

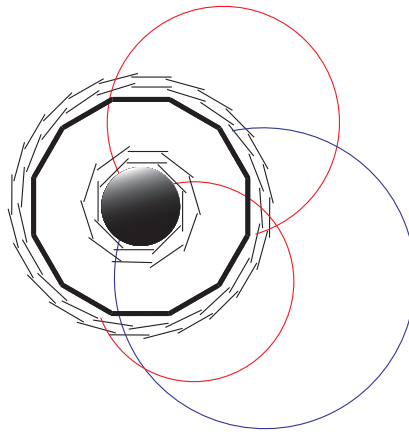
The two other main processes that produce photons are bremsstrahlung and positron annihilation. Due to the low material budget of the Mu3e detector and the low energy of these photons, bremsstrahlung and positron annihilation are neglected in the studies of this thesis.

Bhabha scattering $e^+ + e^- \rightarrow e^+ + e^-$ of Michel positrons with electrons from inside the detector material has the same signature as photon conversion: two electrons with opposite charge from the same vertex that lies in material.

3. The Mu3e Experiment



(a) Lateral view.



(b) Transverse view.

Figure 3.4.: Schematic of the phase I Mu3e detector. Two positron tracks and one electron track from the same vertex are shown: a candidate for $\mu \rightarrow eee$.

3.3. The Mu3e Detector

The Mu3e detector [1] consists of a stopping target that is surrounded by four barrel-shaped layers of pixel detectors, grouped in two double layers as shown in figure 3.4. For better timing resolution, two additional timing systems are used. A solenoid provides a homogeneous magnetic field with a strength of 1 T parallel to the muon beam. The active pixel sensors are cooled with a gaseous helium flow.

Simulations using this geometry are used for the studies presented in this thesis.

3.3.1. Stopping Target

The stopping target in the shape of a hollow double-cone has a length of 10 cm and a maximum radius of 19 mm. The target is made out of Mylar foil with a thickness of 75 μm in upstream direction and 85 μm downstream. Suspension is realised by three nylon wires at each tip with a diameter of 250 μm . Furthermore, one additional nylon wire runs through the target connecting the two tips.

3.3.2. Pixel Tracker

Two cylindrical pixel layers are positioned close to the target to maximise the vertex resolution with the minimal radius of the innermost layer being 23.3 mm. These inner layers consist of six pixel sensors in length with a total length of 12 cm.

The outer pixel layers are built from the same pixel sensors as the inner layers but have a length of 34 and 36 cm for the third and fourth layer, respectively. The minimum radius for the outermost layer is 86.3 mm.

Furthermore, as shown in figure 3.4, there are two additional detector stations with double layers of pixel sensors and timing detectors placed down- and upstream of the central detector. These recurl stations increase the accuracy for high-momentum tracks by measuring two additional hits and additional timing information in the tile detector. Tracks that traverse the recurl station are stopped in the tile detector.

It is foreseen that in phase II two more recurl stations are added to accept even tracks with the highest possible momentum of half the muon mass and a transverse momentum small enough to overshoot the first recoil station.

Pixel Sensors

The pixel layers in Mu3e are based on High-Voltage Monolithic Active Pixel Sensors (HV-MAPS) [22] of size $20 \times 23 \text{ mm}^2$. The active area of one sensor is $20 \times 20 \text{ mm}^2$ with pixel sizes of $80 \times 80 \mu\text{m}^2$ corresponding to 250×250 pixels. By thinning the sensors to 50 μm , multiple Coulomb scattering is minimised. Together with a polyimide support structure and a high density interconnect (HDI) providing aluminium data and power lines, each layer has a total radiation length fraction of

3. The Mu3e Experiment

$$X/X_0 = 0.115 \%$$

3.3.3. Timing Detector

The purpose of timing detectors in Mu3e is the suppression of accidental background. Since in the central part of the detector, spatial resolution and low material budget are more important than in the recoil stations, two different timing detector systems have been chosen.

In the central detector part, scintillating fibres are placed just inside the third pixel layer (see figure 3.4). The timing resolution for this detector is better than 500 ps, allowing charge identification for tracks. Timing resolution improves with a higher number of fibres. However, in a low-material detector like Mu3e, scintillating fibres contribute significantly to the overall material budget. The current design foresees using three fibre layers corresponding to 0.3% of the radiation length in total.

The second timing detector located in the recoil stations consists of scintillating tiles with a size of $6.5 \times 6.5 \times 5 \text{ mm}^3$ and provides the most precise timing information of tracks with an accuracy of 100 ps. Multiple Coulomb scattering in the tiles does not affect the tracking resolution. Therefore, higher amounts of material can be afforded. The electrons are stopped in the beam pipe on which the tile detector is located.

3.3.4. Data Acquisition

All subdetectors continuously send zero-suppressed hit information to the data acquisition system which consists of three layers: front-end FPGAs, switching boards and a filter farm.

The front-end FPGAs collect, sort and package data that is streamed from the pixel and timing detectors. Switching boards act as switches between these FPGAs and the filter farm. They allow each farm-PC to evaluate data from the full detector in overlapping time frames. The farm PCs are equipped with high-end GPUs on which track fits and vertex selection are performed. Only $\mu \rightarrow eee$ candidates are kept whereas most of the background tracks are already filtered out at this stage.

3.4. Possible Modifications to the Mu3e Experiment

In total, the filter farm reduces the output from about 80 Gbit/s to a data rate of 50–100 MBytes/s which is then saved to mass storage.

3.4. Possible Modifications to the Mu3e Experiment

The electron tracking capabilities of the Mu3e detector can be used for other measurements, some of which require modifications to the Mu3e detector.

3.4.1. Mu3e-Gamma

Upgrades to the Mu3e detector for the search for the cLFV decay $\mu \rightarrow e\gamma$ have been proposed. This section will briefly discuss this decay and the experimental possibilities to search for it with Mu3e.

The Decay $\mu \rightarrow e\gamma$

Like the decay $\mu \rightarrow eee$, the decay $\mu \rightarrow e\gamma$ violates lepton flavour conservation. The current upper limit on this decay has been established by the MEG collaboration with $\mathcal{BR} < 4.2 \times 10^{-13}$ (90 % CL) [23] and will be improved by the upgraded MEG II experiment [24]. Diagrams contributing to the process $\mu \rightarrow e\gamma$ also contribute to $\mu \rightarrow eee$ by internally converting the photon into an electron-positron pair. The sensitivity in the search for $\mu \rightarrow eee$ of these diagrams is suppressed by a factor of 0.006 with respect to $\mu \rightarrow e\gamma$ [25].

Possible Upgrades to the Mu3e Detector

To enable the Mu3e detector to detect photons efficiently, modifications to the baseline design are necessary and have been studied in [27]. A new proposal foresees two additional pixel layers at radii much larger than the outer pixel layers in Mu3e and an increased magnetic field of 2 T (see figure 3.5).

The radii of the additional layers are chosen to be large enough that positrons from the target region with momenta of less than 53 MeV cannot reach the outer layers. Photons can be reconstructed if they convert in a converter foil underneath these additional layers and the conversion electrons recurl in the magnetic field. An

3. The Mu3e Experiment

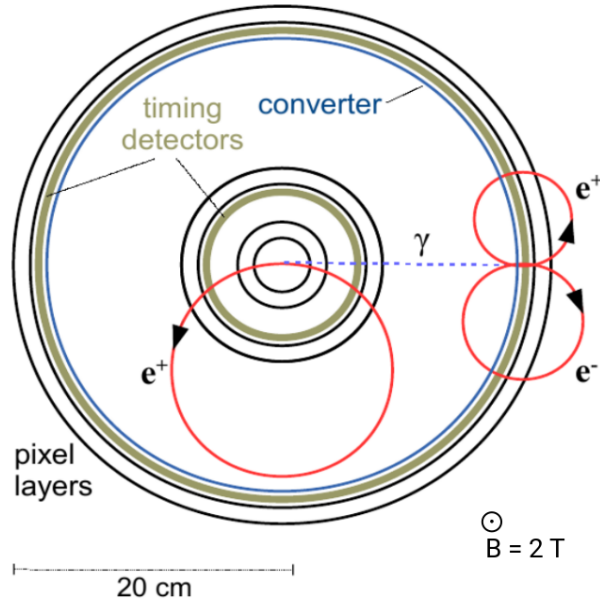


Figure 3.5.: Schematic of the Mu3e-Gamma proposal. Photons convert in a converter foil and the conversion electrons recurl multiple times. For timing information, another timing detector is placed between the converter and the pixel layers [26].

additional timing detector in the outer layers provides precise timing information for background suppression and correct hit assignment to recurling electrons.

The vertex fit algorithm for photon conversion to an electron and a positron studied in this thesis can also be deployed in the case of Mu3e-Gamma.

3.4.2. Neutral Pions at PSI

PSI offers multiple beam lines for negative and positive pions that could be used to produce neutral pions. In principle, three beam lines are candidates for neutral pion generation: π M1, π E1 and π E5, the beam line for Mu3e phase I. The possible rates at the entrance to the areas are summarised in table 3.1. An overview of the experimental hall at PSI is shown in figure 3.8.

A liquid hydrogen target is desirable because it would provide a high yield of neutral pions. To stop pions in a liquid hydrogen target small enough to fit inside the Mu3e detector, pions need to have a momentum of less than 70 MeV. Therefore a degrader is necessary to slow down pions with higher momenta. A

Table 3.1.: Rates and electron backgrounds for different pion beams suitable for neutral pion production at different momenta. By courtesy of Peter-Raymond Kettle (personal communication, March 2017), [28, 29].

Beam Lines	Pion Rate [s^{-1}]	e/π Ratio
πM1		
210 MeV π^-	2.2×10^7	1:1
111 MeV π^-	4×10^4	175:1
500 MeV π^+	4×10^7	negligible
πE1		
210 MeV π^-	4×10^8	1:2
111 MeV π^-	2×10^7	10:1
500 MeV π^+	1×10^8	< 1?
πE5		
109 MeV π^-	1.5×10^8	4:1

thicker degrader causes more multiple Coulomb scattering which leads to higher losses in the beam, especially for a small target. An alternative target material would be CH_2 .

Furthermore, electron/positron backgrounds are expected in significant amounts (see table 3.1). At π M1 and π E5, electron/pion separation is not possible due to the existing separators being insufficient for the necessary momenta and due to spatial constraints considering the Mu3e detector. Therefore, only at the π E1 beam line, electron/pion separation is feasible.

Beam momenta of 500 MeV are at the very edge of the spectrum at PSI. Taking this, the small cross section and the backgrounds from the reaction $\pi^+ + p \rightarrow \pi^0 + \Delta^{++}$ into account leads to the conclusion that π^0 production via CEX is strongly preferred at PSI.

3.5. Track Reconstruction

Tracks in Mu3e are reconstructed from hit positions in the pixel detector [30] and matched with additional timing information from the two timing detector systems. A free, charged particle describes a helical trajectory in a homogeneous magnetic

3. The Mu3e Experiment

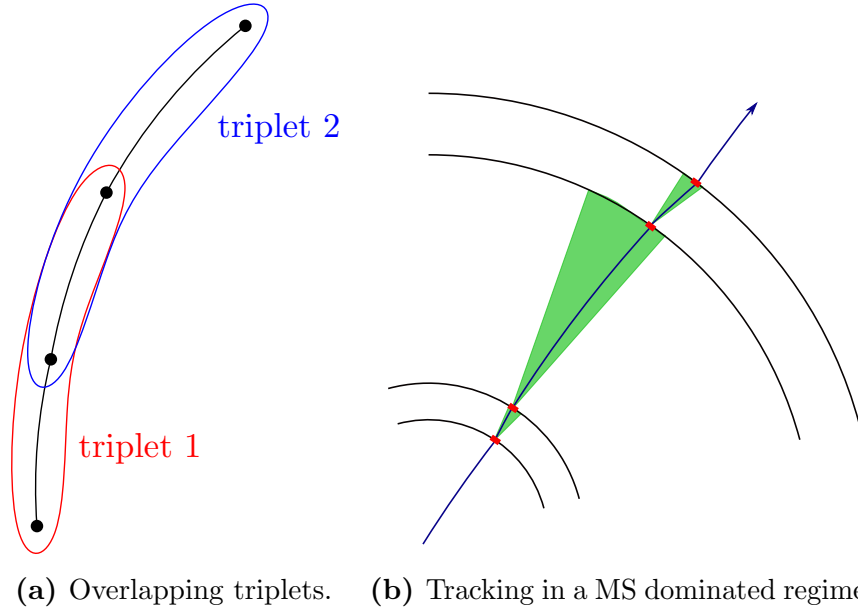


Figure 3.6.: Illustrations of the triplet fit.

field. With a good spatial resolution, multiple Coulomb scattering in the detector layers is the dominant source of tracking uncertainties (sketched in figure 3.6b). A track fit can thus be formulated as a combination of independent hit triplet fits.

Using the hit positions of an initial triplet of hits, a helical trajectory with multiple Coulomb scattering at the middle detector layer is reconstructed. Multiple Coulomb scattering theory (see chapter 4.3) provides the necessary variances for the fitted scattering angles Φ_{MS} and Θ_{MS} . The fit is performed by finding a 3D bending radius $R_{3\text{D}}$ that minimises the χ^2 function [30]

$$\chi^2(R_{3\text{D}}) = \frac{\Phi_{\text{MS}}^2(R_{3\text{D}})}{\sigma_{\Phi}^2} + \frac{\Theta_{\text{MS}}^2(R_{3\text{D}})}{\sigma_{\Theta}^2}. \quad (3.1)$$

To use the hit information of an additional layer to the track, another triplet is constructed using the two outer hits from the first triplet and a hit from the next layer (see figure 3.6a). Scattering in different layers is independent, therefore a global χ^2 function can be expressed as a sum

$$\chi_{\text{global}}^2 = \sum \chi_{\text{triplet}}^2. \quad (3.2)$$

3.5. Track Reconstruction

Minimisation of this sum is performed to find a 3D track radius that is constant under the assumption of negligible energy loss in the layers.

If a track recurls in the magnetic field, it can produce up to two additional hits in one of the recurl stations or four and more additional hits in the central detector. The momentum resolution for six- and eight-hit tracks is higher than for four-hit tracks because of the larger lever-arm. Timing information improves the track finding performance and suppresses reverse reconstruction of eight-hit tracks.

Modifications of the track reconstruction allow for tracks to be reconstructed starting with a hit in the second pixel layer [31]. These tracks can be used to enhance the sensitivity in searches with displaced vertices such as decays between the first and second layer or photon conversion in the second layer.

The radius of the outermost layer and the magnetic field are optimised to minimise the effect of multiple scattering for recurling particles in first order (see figure 3.7).

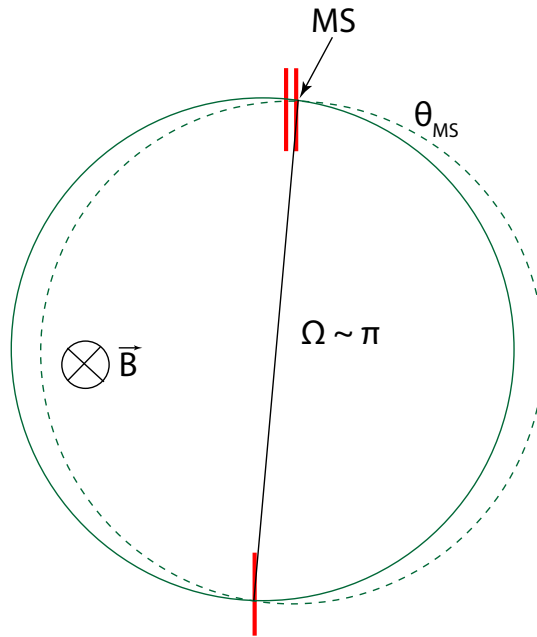


Figure 3.7.: The effect of MS is minimised for semi-circular trajectories.

3. The Mu3e Experiment

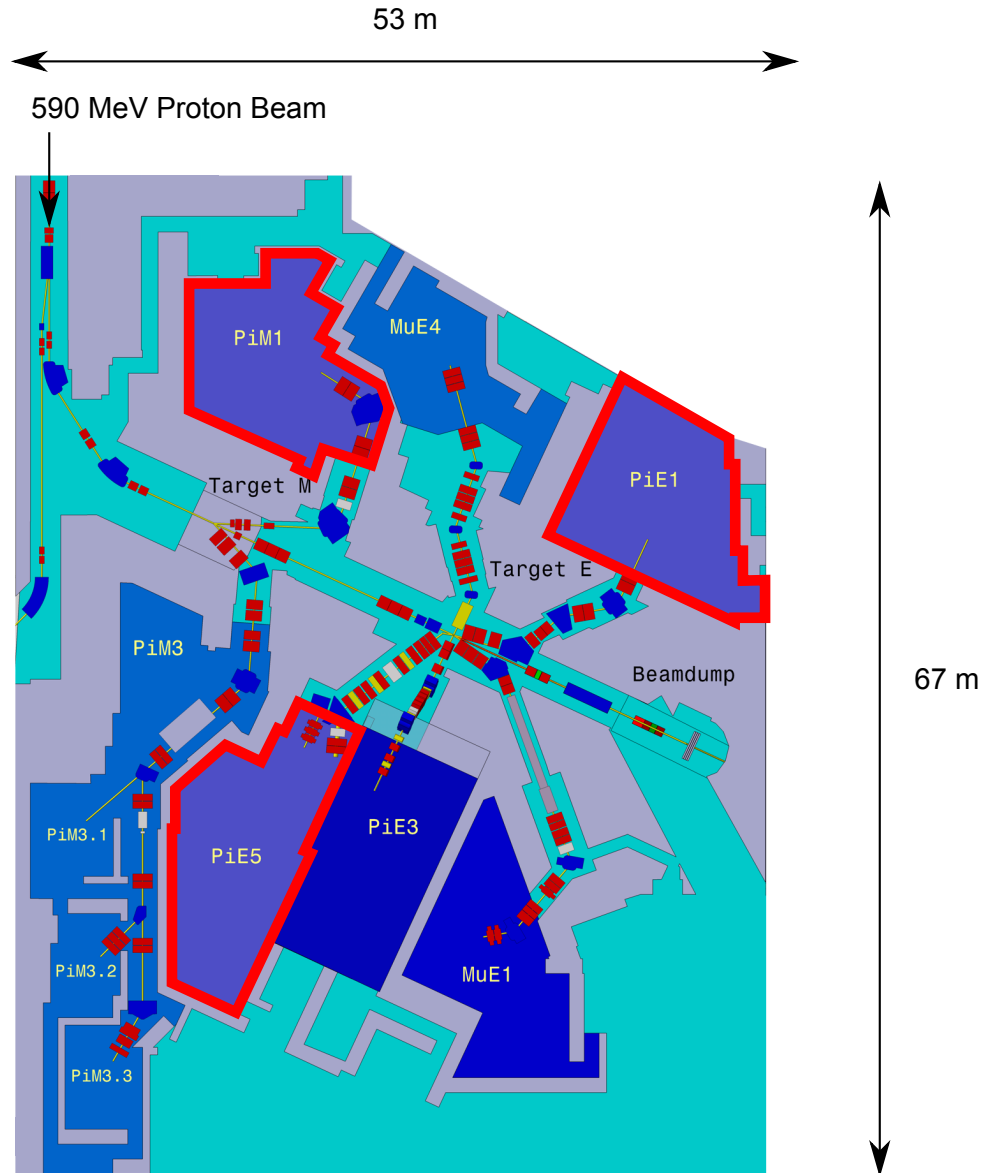


Figure 3.8.: Section of the experimental hall at PSI Potential beam lines for pion measurements with Mu3e are highlighted (red borders). By courtesy of Markus Lüthy, Wolfgang Burkert and Thomas Rauber (edited).

4. The Multiple Scattering Vertex Fit

The following chapter describes the multiple Coulomb scattering (MS) vertex fit [19]. Within the scope of this thesis, this fit has for the first time been performed with two-track events and, on that account, the derivations have been reviewed and the implementation has been improved.

4.1. Introduction

Almost all detectors currently used in high energy physics use a semiconductor-based inner tracking system. Due to the good spatial resolution of pixel detectors— $80\ \mu\text{m}/\sqrt{12} \approx 23\ \mu\text{m}$ in the case of the Mu3e experiment—hit uncertainties become less and less important. Particles in Mu3e have a low momentum compared to tracks in collider experiments such as LHC. Therefore MS is much more pronounced in Mu3e (see section 4.3).

Low-momentum tracks are highly bent in magnetic fields and cannot be approximated by straight tracks in the inner vertex region. In Mu3e, momenta range up to 53 MeV and the homogeneous magnetic field has a strength of 1 T. A more adequate track model is a helical track model. Highly bent trajectories create nonlinearities which have to be taken into account when linearising by iterative fitting.

The aim of the linearised vertex fit described in this chapter is to exploit the high precision of modern pixel detectors and handle the challenges of highly bent tracks that are subject to MS. It is assumed that all tracks of an event originate from the same vertex. The position of this vertex \vec{v} is reconstructed using only the track parameters and no additional information like opening angles between the

4. The Multiple Scattering Vertex Fit

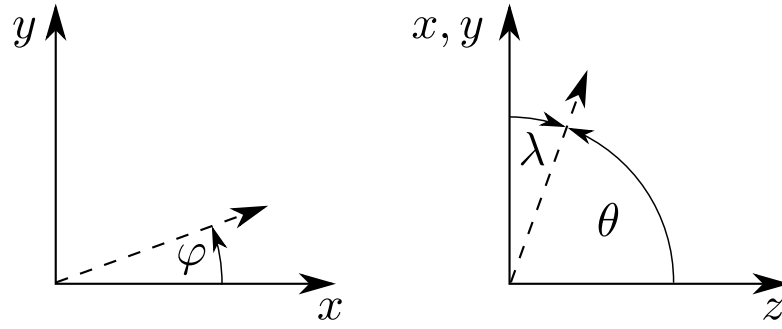


Figure 4.1.: Sketch of the azimuthal angle φ and the polar angles θ and $\lambda = \theta - \frac{\pi}{2}$.

tracks or the position of a target. Therefore, the vertex fit is suited to reconstruct particle decays and conversions of any mass and is not limited to photon conversion.

4.2. Coordinate System

A right-handed Cartesian coordinate system is chosen with the z -axis pointing in the direction of the homogeneous magnetic field and the beam. The x - and y -axes are then defined as horizontal and vertical, respectively. Furthermore, scattering angles are usually studied in a spherical coordinate system where θ and λ denote the polar angles, and φ the azimuthal angle (see figure 4.1).

4.3. Multiple Coulomb Scattering

For extrapolation of tracks into the vertex region, MS at the innermost pixel layer is the only uncertainty considered. Spatial and directional uncertainties of the reconstructed tracks as well as the uncertainty of the bending radius are neglected. By introducing the *right* kink angles $\Phi_{\text{MS},i}$ and $\Theta_{\text{MS},i}$ at the first layer for each track i , the tracks are forced to intersect with a common vertex position \vec{v} (see figure 4.2).

Multiple Coulomb scattering in material is caused by multiple deflection of a charged particle in the Coulomb field of nuclei. In contrast to deflection off electrons (ionisation), there is no significant energy transfer in multiple Coulomb

4.3. Multiple Coulomb Scattering

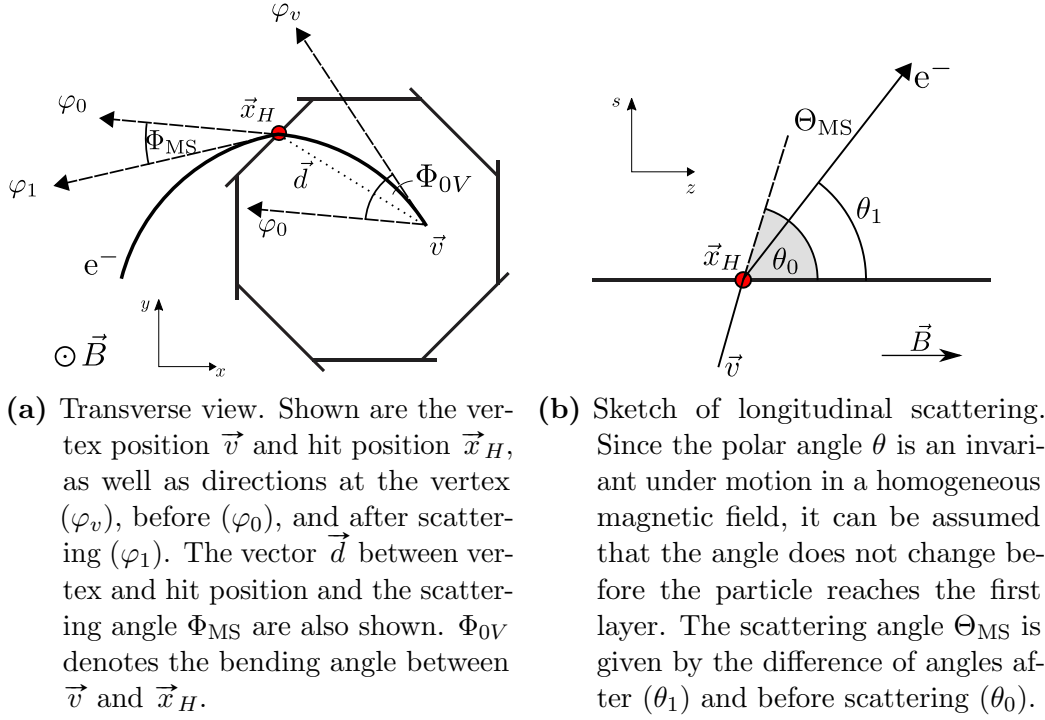


Figure 4.2.: Sketches of scattering at the first layer in different views. The vertex position \vec{v} and hit position \vec{x}_H as well as the relevant directional vectors are shown.

scattering. For tracks in a homogeneous magnetic field, this means that only the direction is changed by MS, while the 3D bending radius provided by the track reconstruction is conserved.

For tracks with energies well between the electron and proton mass $m_e \ll E \ll m_p$, single scattering on nuclei is described by *Mott scattering*. The differential cross section $\frac{d\sigma}{d\Omega}$ as a function of the scattering angle ϑ and the electron energy E is given by [6]:

$$\left(\frac{d\sigma}{d\Omega}\right)_{\text{Mott}} = \frac{\alpha^2}{4E^2 \sin^4(\vartheta/2)} \cos^2 \frac{\vartheta}{2}, \quad (4.1)$$

where α is the fine-structure constant.

The distribution of scattering angles for multiple Coulomb scattering is described by *Molière's theory*. For small scattering angles ϑ , the central 98% of the distribution can be described as Gaussian with a mean $\langle\vartheta\rangle = 0$ and a projected

4. The Multiple Scattering Vertex Fit

root mean square given by the Highland representation [14]:

$$\sigma_{\text{MS}} = \frac{13.6 \text{ MeV}}{\beta p} q \sqrt{\frac{\delta_{\text{eff}}}{X_0}} [1 + 0.038 \ln(\delta_{\text{eff}}/X_0)], \quad (4.2)$$

where p is the particle momentum in MeV, β is the velocity in units of the speed of light and q is the charge of the scattered particle ($|q| = 1$ for electrons and positrons). δ_{eff}/X_0 is the effective thickness of the scattering material $\delta_{\text{eff}} = d/\cos \alpha$ in units of the radiation length X_0 that depends on the thickness d and the inclination angle α . For Mu3e, δ_{eff}/X_0 is in the order of 0.1 % per layer for perpendicular tracks.

The variances of the two scattering angles Θ_{MS} and Φ_{MS} are then given by $\sigma_{\Theta}^2 = \sigma_{\text{MS}}^2$ and $\sigma_{\Phi}^2 = \sigma_{\text{MS}}^2/\sin^2 \theta$ where θ is the polar angle of the track direction [30]. In the local coordinate system of the track, the variances are equal and the transformation to the global coordinate system results in the additional factor $1/\sin^2 \theta$ for the azimuthal angle.

4.4. Least Squares Method

To find the best estimate for a common vertex position \vec{v} , the χ^2 -function of the kink angles is minimised:

$$\chi^2(\vec{v}) = \sum_{i=\text{tracks}} \frac{\Phi_{\text{MS},i}(\vec{v})^2}{\sigma_{\Phi,i}^2} + \frac{\Theta_{\text{MS},i}(\vec{v})^2}{\sigma_{\Theta,i}^2} \quad (4.3)$$

to obtain the most probable common vertex position \vec{v} for all tracks. Decoupling of Φ_{MS} and Θ_{MS} is a result of coordinate transformation from the moving orthonormal frame to the global coordinate system [32]. Mean scattering angles of zero are directly given by scattering theory.

In the notation of [33], the scattering angles of a single track can be expressed as the vector of kink angles

$$\vec{\alpha} \equiv \vec{\alpha}(\vec{v}) = \begin{pmatrix} \Theta_{\text{MS}}(\vec{v}) \\ \Phi_{\text{MS}}(\vec{v}) \end{pmatrix}. \quad (4.4)$$

4.4. Least Squares Method

Linearisation around an initial vertex estimate \vec{v}_0 , i.e. $\vec{v} \approx \vec{v}_0 + d\vec{v}$, yields

$$\vec{\alpha}(\vec{v}) = \vec{\alpha}_0 + d\vec{\alpha} \quad \text{with} \quad d\vec{\alpha} = \underline{\mathbf{J}}d\vec{v}, \quad (4.5)$$

where $\vec{\alpha}_0 := \vec{\alpha}(\vec{v}_0)$ is the set of initial kink angles and

$$(\underline{\mathbf{J}})_{ij} = \left. \frac{\partial(\vec{\alpha})_i}{\partial(\vec{v})_j} \right|_{\vec{v}=\vec{v}_0} \quad (4.6)$$

is the Jacobian matrix evaluated at the initial vertex position \vec{v}_0 .

In order to calculate the scattering angles for N tracks, one can extend the initial scattering angles and Jacobian matrices in the following block matrix form:

$$\underline{\vec{\alpha}}_0 = \begin{pmatrix} \vec{\alpha}_0^0 \\ \vec{\alpha}_0^1 \\ \vdots \\ \vec{\alpha}_0^{N-1} \end{pmatrix} \quad \text{and} \quad \underline{\mathbf{J}} = \begin{pmatrix} \mathbf{J}_0 \\ \mathbf{J}_1 \\ \vdots \\ \mathbf{J}_{N-1} \end{pmatrix} \quad (4.7)$$

with dimensions $2N \times 1$ for the initial scattering angles $\underline{\vec{\alpha}}_0$ and $2N \times 3$ for the Jacobian block matrix $\underline{\mathbf{J}}$.

Equation 4.3 with correlations in block matrix notation yields the objective function

$$S = \left(\underline{\vec{\alpha}}_0 + \underline{\mathbf{J}}d\vec{v} \right)^T \underline{\Sigma}^{-1} \left(\underline{\vec{\alpha}}_0 + \underline{\mathbf{J}}d\vec{v} \right). \quad (4.8)$$

Herein, $\underline{\Sigma}$ denotes the block-diagonal covariance matrix

$$\underline{\Sigma} = \begin{pmatrix} \Sigma_0 & & & \\ & \Sigma_1 & & \\ & & \ddots & \\ & & & \Sigma_{N-1} \end{pmatrix} \quad \text{with} \quad \Sigma_i = \begin{pmatrix} \sigma_{\Theta_{\text{MS},i}}^2 & \text{cov}(\Theta, \Phi)_i \\ \text{cov}(\Theta, \Phi)_i & \sigma_{\Phi_{\text{MS},i}}^2 \end{pmatrix}. \quad (4.9)$$

The variances σ^2 are obtained from scattering theory (section 4.3) and $\text{cov}(\Theta, \Phi)$ denotes the covariance of the two angles, which is zero in the chosen coordinate system. The inverse of the error block matrix is the weight block matrix $\underline{\mathbf{W}} = \underline{\Sigma}^{-1}$.

4. The Multiple Scattering Vertex Fit

The objective function is minimised by solving $\frac{\partial S}{\partial(\vec{d}v)} = 0$, which yields

$$\underline{\mathbf{J}}^T \underline{\mathbf{W}} \vec{\alpha}_0 + \underline{\mathbf{J}}^T \underline{\mathbf{W}} \underline{\mathbf{J}} \vec{d}v = 0. \quad (4.10)$$

Solving these normal equations determines the best-fit vertex correction $\vec{d}v$ and its error matrix $\underline{\Sigma}_{\vec{d}v}$:

$$\vec{d}v = -(\underline{\mathbf{J}}^T \underline{\mathbf{W}} \underline{\mathbf{J}})^{-1} \underline{\mathbf{J}}^T \underline{\mathbf{W}} \vec{\alpha}_0 \quad (4.11)$$

$$\underline{\Sigma}_{\vec{d}v} = (\underline{\mathbf{J}}^T \underline{\mathbf{W}} \underline{\mathbf{J}})^{-1}. \quad (4.12)$$

The block-diagonal structure of the covariance matrix allows a straightforward calculation of these matrix products:

$$\underline{\mathbf{J}}^T \underline{\mathbf{W}} \underline{\mathbf{J}} = \sum_{i=0}^{N-1} \underline{\mathbf{J}}_i^T \underline{\mathbf{W}}_i \underline{\mathbf{J}}_i \quad (4.13)$$

$$\underline{\mathbf{J}}^T \underline{\mathbf{W}} \vec{\alpha}_0 = \sum_{i=0}^{N-1} \underline{\mathbf{J}}_i^T \underline{\mathbf{W}}_i \vec{\alpha}_{0,i}. \quad (4.14)$$

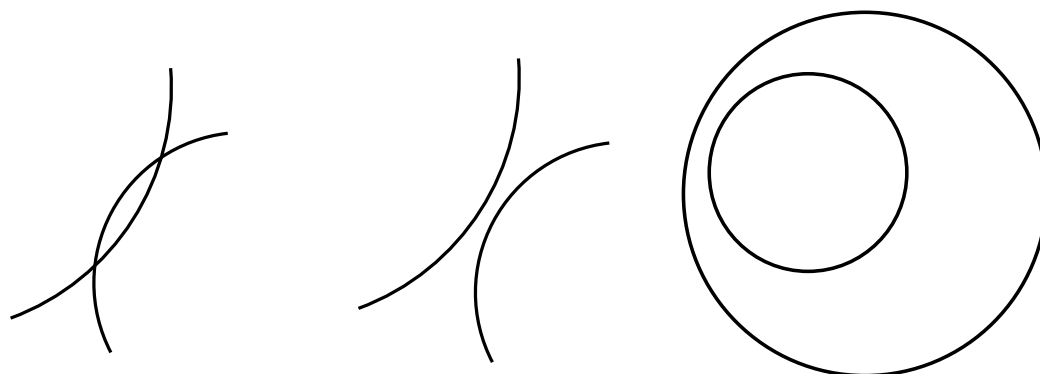
To account for nonlinearities, one can perform this fit iteratively by using the sequence $\vec{v}_{n+1} = \vec{v}_n + \vec{d}v_n$.

4.4.1. The Error Matrix

Every covariance matrix is diagonalisable [34], which means that a linear transformation to a set of uncorrelated variables can be found. Since all eigenvalues are non-negative, a covariance matrix can be interpreted as an ellipsoid with the length of the semi-principal axes corresponding to the standard deviations in the new basis $\sigma_{1,2,\dots,n}$. This so-called *error ellipsoid* represents the volume of uncertainty for the fitted parameters.

A three-dimensional ellipsoid with two equal semi-diameters is called a spheroid. If one semi-diameter is smaller than the other two, the spheroid is called an *oblate spheroid*, if it is larger, it is called a *prolate spheroid*.

For the small opening angles between the tracks of photon conversion, the error ellipsoid is expected to be a spheroid. The shape of the ellipsoid is studied in



(A) The two tracks intersect in two points. (B) The tracks do not intersect and lie outside of each other. (C) One track encloses the other.

Figure 4.3.: The three possible configurations for two helical tracks in the transverse view (not possible for photon conversion).

section 5.3.

4.5. Initial Vertex Finding

In the case of two tracks, initial vertex finding can be performed geometrically by assuming helical tracks and separating the track in a transverse and a longitudinal component. In transverse view, helical tracks are circular. Three different configurations are possible (see figure 4.3):

- (A) The tracks intersect in two points.
- (B) The tracks do not intersect and lie outside of each other.
- (C) One track encloses the other.

Configurations with only one touching intersection are possible when two tracks graze in one point. In these cases, the touching intersection is chosen to be the initial vertex estimate.

In case A, when there are two intersections in the transverse view, the distances in z at both transverse intersections are compared. The intersection with the smaller z -distance is then chosen as the initial guess for the vertex fit. The x - and y -position of the initial guess are directly obtained from the transverse intersection.

4. The Multiple Scattering Vertex Fit

The z -component of the initial guess is chosen to be the mean of the z -coordinates of the tracks at the point of transverse intersection. In case B and C, a transverse point of closest approach can be found, from which the x - and y -position of the initial guess are calculated. The z -component is again obtained by taking the average z -positions of both tracks at the point of closest approach. If there is only one intersection, this is also the point of closest approach. The question how to treat these transitional cases is merely technical and the result does not depend on the implementation.

Part II.
Studies

5. Photon Studies

This chapter covers the application of the vertex fit (see chapter 4) to two tracks that belong to a photon conversion event. As photons only convert in matter, conversion events in Mu3e can be divided into two groups. Either, the photon converts in passive material, such as the target, and the conversion electrons cover a significant distance before they produce hits in the pixel detector, or the conversion occurs in one of the pixel detector layers. The former will be called *conversion in the target*, the latter will be called *conversion in a layer*. If photons convert in one of the layers, the two electron tracks produce hits either in the same pixel or in two pixels next to each other.

If the energy deposition from ionisation in the active part of the pixels is less than 5 keV, no hit is registered in the simulation. For photon conversion within the silicon, this means that the probability for producing a hit becomes small if the electrons only cover short distances. The mean total energy loss including bremsstrahlung is about 0.4 keV/ μm per particle in silicon [14]. In the case that less than 5 keV are deposited in the silicon, no hits are produced in the first layer. Thus, the conversion vertex is spatially well separated from the first hit position (then in the second layer). These events are therefore not regarded as converted in a layer.

A very small contribution⁽¹⁾ also comes from conversion in the gaseous helium. Conversion in the helium in the target region is treated the same way as conversion in the target material. Conversion in between the pixel layers is not regarded as conversion in one of the two layers for the same reasons as above.

First of all, general challenges of vertex reconstruction using a linearised vertex fit with highly parallel tracks are explained. Behaviour of the fit itself and ways to

⁽¹⁾The probability for conversion in helium is very small due to the radiation length of $X_0 = 5.67 \times 10^5 \text{ cm}$ [7].

5. Photon Studies

ensure convergence are discussed. The main part of this chapter consists of the study of reconstructed quantities for photon conversion events. In the end, a brief estimate of the expected amount of converted photons from radiative muon decays is given.

5.1. Simulation and Reconstruction

Results shown in this chapter are obtained using an extended version of the Mu3e framework [1]. The reconstruction is modified to also reconstruct tracks starting from the second detector layer with five or seven hits in total [31] and tracks can share a common pixel hit.

The vertex fit itself is implemented in the `watson` tracking library [35]. The development version `0.6-dev` features a reimplementaion of the vertex fit using a different track parametrisation. It supports Tikhonov regularisation [36] to allow for an effective cut-off of vertex changes above a certain length scale. For future compatibility, this version is used in the studies presented here. The implementation is tested and improved by comparing to the previous implementation and by using MINUIT, an alternative minimisation program [37].

Except for the studies of radiative muon decays in section 5.5, photons are generated isotropically in radial direction on a spherical surface around the centre of the target. The centre of the target is omitted to avoid conversion and scattering in the nylon wire (see section 3.3.1). The photon energies are uniformly distributed between 50 and 55 MeV. For the radiative muon decays, a minimum photon energy of 20 MeV is chosen which corresponds to a branching fraction of 0.437%.

Tracks with different numbers of pixel hits enter the vertex fit. The shortest tracks have four hits in the central part of the detector, the longest tracks reconstructed have eight hits. No differentiation between tracks that enter the vertex fit with different numbers of hits were made. Tracks with an even number of hits are reconstructed starting from the innermost detector layer. Tracks with an odd number of hits have their first hit in the second detector layer. For different length of tracks, different cuts on the χ^2 of the tracks are applied. These cuts are summarised in table 5.1.

Table 5.1.: χ^2 -cuts for tracks reconstructed from different numbers of hits as used in this thesis. For 5- and 7-hit tracks, optimised by [31].

# hits	$\chi_{\text{track,max}}^2$
4	32
5	13
6	48
7	22
8	48

5.2. General Challenges

As described in chapter 4, the χ^2 -function of the kink angles of all tracks is minimised by linearising the kink angles $\vec{\alpha}$ around an initial vertex position estimate \vec{v}_0 using the Jacobian matrix \mathbf{J} :

$$\vec{\alpha}(\vec{v}) \approx \vec{\alpha}(\vec{v}_0) + \mathbf{J}d\vec{v} \quad \text{with} \quad (\mathbf{J})_{ij} = \left. \frac{\partial \vec{\alpha}_i}{\partial v_j} \right|_{\vec{v}=\vec{v}_0}. \quad (5.1)$$

Higher order contributions are omitted by linearisation, particularly the next term of the series expansion $\frac{1}{2}(d\vec{v})^T \mathbf{H} d\vec{v}$ with the Hessian matrix $(\mathbf{H})_{i,j} = \frac{\partial^2 \vec{\alpha}}{\partial v_i \partial v_j}$.

Tracks from photon conversion events are very parallel at the true conversion vertex, which poses a difficulty on the vertex fit, since the derivative of $\vec{\alpha}$ with respect to the direction of the tracks nearly vanishes for both tracks. This leads to an overestimation of the vertex corrections $d\vec{v}$. In case of perfect parallelity the corrections would become infinite. The same applies to the shape of the error ellipsoid obtained from the covariance matrix of the vertex correction (equation 4.12).

Single large overestimations of the correction can cause the position \vec{v}_i used in the next iterative step to be so distant from the hit positions that no physical kink angles can be found to force the tracks on the vertex position \vec{v}_i (see also appendix A.1). Overestimation can also cause the fit to *overshoot* the χ^2 minimum repeatedly, which results in oscillation around the minimum (see section 5.4.1).

To limit too large vertex corrections, Tikhonov regularisation is implemented to effectively limit the magnitude of $|d\vec{v}|$. Unless stated otherwise, an upper limit of 1 mm is chosen. Furthermore, oscillations are damped as explained in section 5.4.1.

5.3. Chi-squared in Space

The vertex fit provides an error estimate in form of a covariance matrix that can be represented as an error ellipsoid (see section 4.4.1).

The shape of this ellipsoid can be studied using the ratios of the lengths of the semi-principal axes of the error ellipsoid. With the length of the largest semi-principal axis σ_1 and the second and third largest axes σ_2 and σ_3 , respectively, one can define the ratios

$$r_{12} = \frac{\sigma_1}{\sigma_2} \quad \text{and} \quad (5.2)$$

$$r_{23} = \frac{\sigma_2}{\sigma_3}, \quad (5.3)$$

$$\text{with } \sigma_3 \leq \sigma_2 \leq \sigma_1. \quad (5.4)$$

The error ellipsoids of 774 converged fits from conversion events in the stopping target material are studied without Tikhonov regularisation. The average ratios are calculated to:

$$r_{12}^{\text{on target}} = 29.316 \pm 0.038 \quad \text{and} \quad (5.5)$$

$$r_{23}^{\text{on target}} = 1.006588 \pm 0.000008. \quad (5.6)$$

The results $r_{12} \gg r_{23}$ and $r_{23} \approx 1$ imply a prolate spheroidal shape of the error ellipsoids. For conversion in layers, the covariance matrix is ill-defined and no ratios can be provided (see section 5.4.1).

5.3.1. Orientation of the Error Ellipsoid

A comparison of the angle between the major semi-axis of the error ellipsoid and the photon momentum shows that the major axis of the error ellipsoid and the photon are well aligned (see figure 5.1). Since the parallelity of the two tracks near the true vertex is the cause for the long shape of the error ellipsoid, it is clear that the orientation of the ellipsoid and the photon momentum are correlated.

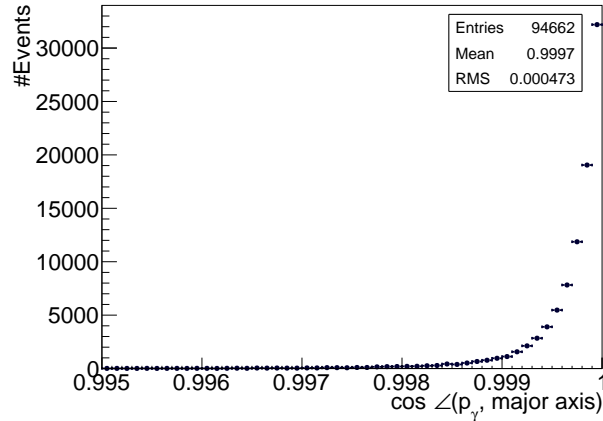


Figure 5.1.: Histogram of the cosine of the angle between the photon momentum and the major axis of the error ellipsoid.

5.3.2. Chi-squared Maps

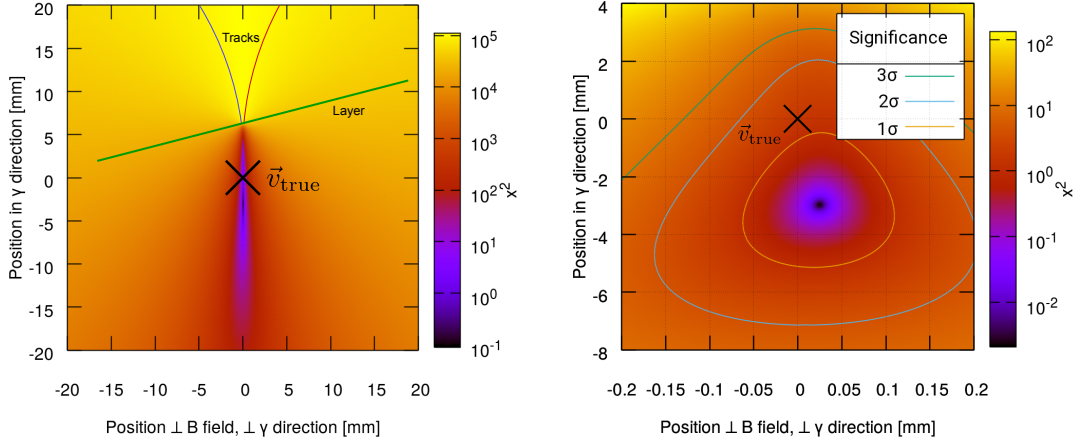
To visualise the shape of the χ^2 -minimum, χ^2 -maps are created. For this, one defines a *pseudo decay plane* in which the tracks are bent after conversion. The plane is spanned by the direction of the photon and a vector perpendicular to both the magnetic field \vec{B} and the photon momentum.

One characteristic map is shown in figure 5.2. Two effects are visible: In photon direction, the minimum is much broader than in the other direction, and even though the true conversion vertex is well within the 2σ region, the χ^2 minimum is displaced by almost three millimetres, which matches well the RMS of the residual distribution (see section 5.4.4).

5.3.3. Existence of a Second Minimum

In some cases, the electron and the positron can scatter in a way that results in two local χ^2 -minima. The existence of a second minimum cannot be detected by the MS vertex fit. Since a second minimum can only form if there are two intersections in the transverse plane (configuration A), table 5.2 suggests that the fit still converges in one of the minima. However, these two minima are embedded in the same long *valley* (see figure 5.3). No event with a separation of more than

5. Photon Studies



- (a) Full view of the event. The innermost detector layer and the two tracks are shown. (b) Close-up view of the region around the minimum. Contour lines for 1σ , 2σ , and 3σ are shown.

Figure 5.2.: χ^2 map for a single event in 2D. The grid is chosen to be on the *pseudo decay plane*. Note that the origin is the true point of conversion.

1σ has been observed in the studies of this thesis, therefore even the *wrong* local minimum is still within the uncertainties of the global minimum.

5.4. Photon Vertex Fit Studies

This section covers studies of the behaviour and results of the vertex fit. First, convergence of the fit is discussed, then resolutions of reconstructed quantities are presented.

5.4.1. Convergence

Successful fitting is not guaranteed, even for the correct combination of tracks. A fit is regarded as converged if within a finite number of iterations $n_{\text{steps,max}}$ a vertex correction below a certain threshold δ_{max} is reached. For the following studies, $n_{\text{steps,max}}$ is chosen to be 1000 and δ_{max} to be $1\mu\text{m}$. If two consecutive vertex corrections cancel each other out, the fit is most likely oscillating around

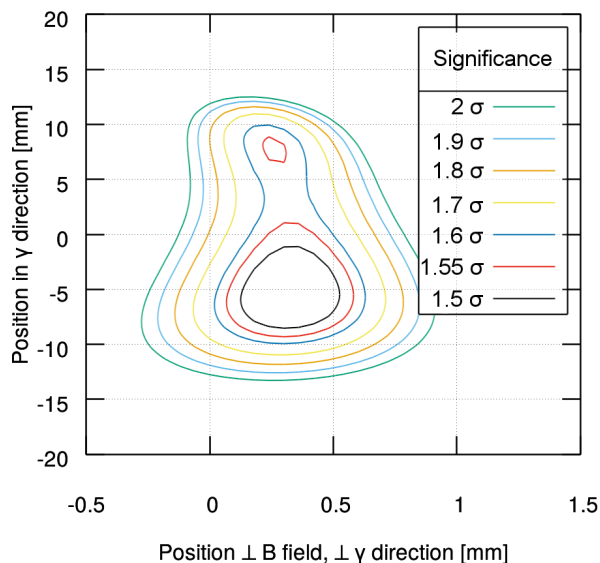


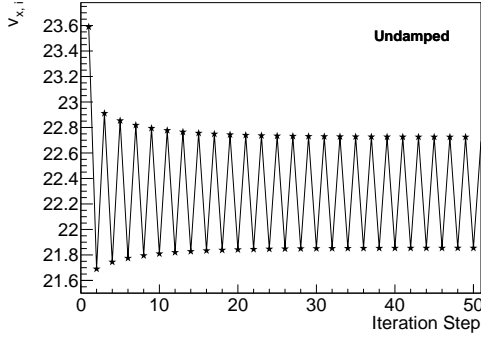
Figure 5.3.: Contour plot for photon conversion with two local χ^2 -minima. The true conversion vertex is at the origin in this figure.

the χ^2 -minimum. Oscillation between two points can be prevented by comparing the difference of the vertex correction of the i -th iteration and the correction of the previous step. To prevent the fit from overshooting, the i -th vertex correction $d\vec{v}_i$ can be artificially damped, if an oscillation is detected. In the context of this thesis, a damping factor of 0.1 is chosen:

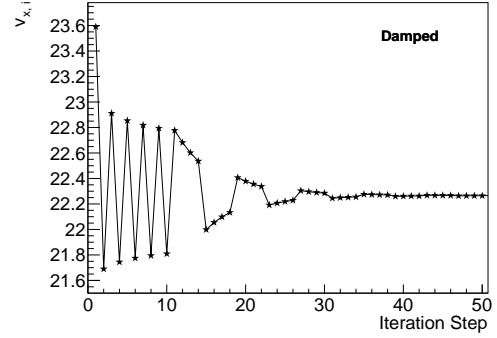
$$\vec{d}v \rightarrow 0.1 \cdot \vec{d}v. \quad (5.7)$$

More complex oscillations can be taken into account as well. In the context of this thesis, the corrections of the three last iterations are considered. If one of the following conditions is fulfilled after the tenth iteration, the current vertex

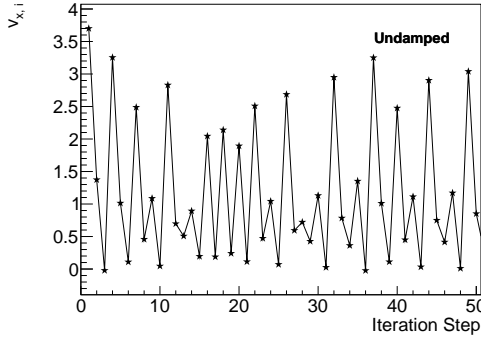
5. Photon Studies



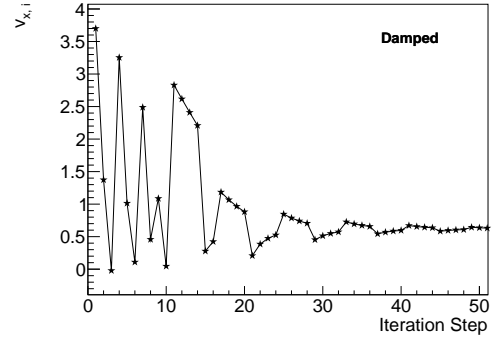
(a) Undamped two-point oscillation, no convergence after 1000 iterations.



(b) Damped two-point oscillation, converged after 53 iterations.



(c) Undamped irregular oscillation, no convergence after 1000 iterations.



(d) Damped irregular oscillation, converged after 93 iterations.

Figure 5.4.: Examples of the vertex fit not converging without damping. Shown is only the x -component of the vertex fit position. 5.4a and 5.4b show the same event, so do 5.4c and 5.4d. For demonstration purposes, no limit on the vertex correction via Tikhonov regularisation is implemented here. Damping is implemented from the 10th iteration onwards.

correction is scaled down:

$$|d\vec{v}_{i-1} + d\vec{v}_i| < |d\vec{v}_i| \quad (5.8)$$

$$|d\vec{v}_{i-2} + d\vec{v}_{i-1} + d\vec{v}_i| < |d\vec{v}_i| \quad (5.9)$$

$$|d\vec{v}_{i-3} + d\vec{v}_{i-2} + d\vec{v}_{i-1} + d\vec{v}_i| < |d\vec{v}_i|. \quad (5.10)$$

The effect of damping can be seen in figure 5.4 for two-point oscillation (5.4a and 5.4b) and a more irregular oscillation (5.4c and 5.4d).

An appropriate choice for the Tikhonov regularisation scale is a maximum vertex correction of 1 mm. A single overestimation of the vertex correction cannot cause the fit to fail by moving the fit position to unreachable distances, if the corrections are limited.

With these countermeasures against fit failure, convergence is achieved in 95.6 % of the time. The effects of different conversion locations and configurations of the tracks are broken down in table 5.2. Conversion can occur in the stopping target or one of the silicon pixel layers. Only tracks beginning in the first and second layer are reconstructed, thus only conversion in the first and second layer can be found. For the different locations, conversion events are divided by the initial configuration of the tracks, i.e. whether there are intersections in the transverse projection (configuration A) or not (configuration B). Furthermore, the two electrons from photon conversion in one of the pixel layers can be so close that the same pixel is traversed by both particles. Then, the two tracks share their first hit.

The column *occurrence* denotes the occurrence in the respective group. The occurrence of conversion at each location is to be understood globally, i.e. 7.8 % of the reconstructable conversion events occurs in the target. In 60.9 % of these events, the two tracks had transverse intersections, etc.

Conversion in Target

The fit converges in 99.1 % of the cases in which a photon converts in the material of the stopping target. In nearly all cases in which the fit does not converge, at one point, the iterative fit has arrived at a point which could not be reached by introducing kink angles at the first layer.

The fit convergence for photon conversion in the target material depends on the configuration of the two tracks (see section 4.5). For two intersections in the transverse projection (configuration A), 98.6 % of the fits converged. For events without a transverse intersection (configuration B), the fit converges in over 99.9 % of the time. Configuration A occurs slightly more often than configuration B with 60.9 %.

5. Photon Studies

Table 5.2.: Convergence of the vertex fit for different configurations of the tracks. The fit can fail due to exceeding of the maximum number of steps $n_{\text{steps}} = 1000$ or because no initial kink angles could bend the tracks on one of the vertex positions \vec{v}_i during the iterative fit. In configuration A, the two tracks have two intersections in the transverse view, in configuration B, there are no intersections.

	occurrence	converged	n_{steps} exceeded	no kink angles
Conversion in Target				
total	7.8 %	99.1 %	< 0.1 %	0.9 %
config. A	60.9 %	98.6 %	< 0.1 %	1.4 %
config. B	39.1 %	99.9 %	< 0.1 %	< 0.1 %
Conversion in Layer 1				
total	44.3 %	96.9 %	0.2 %	2.9 %
config. A	98.4 %	97.0 %	0.2 %	2.8 %
config. B	1.6 %	90.6 %	2.1 %	7.3 %
shared hit	94.0 %	98.8 %	0.2 %	1.0 %
shared hit & A	100 %	98.8 %	0.2 %	1.0 %
shared hit & B	0 %	—	—	—
no shared hit	6.0 %	66.5 %	1.5 %	32.0 %
no shared hit & A	73.9 %	58.0 %	1.3 %	40.7 %
no shared hit & B	26.1 %	90.6 %	2.1 %	7.3 %
Conversion in Layer 2				
total	38.8 %	95.6 %	0.4 %	4.0 %
config. A	97.6 %	95.7 %	0.3 %	3.9 %
config. B	2.4 %	89.0 %	3.2 %	7.7 %
shared hit	90.2 %	98.7 %	0.2 %	1.1 %
shared hit & A	100 %	98.7 %	0.2 %	1.1 %
shared hit & B	0 %	—	—	—
no shared hit	9.8 %	66.9 %	2.4 %	30.7 %
no shared hit & A	75.7 %	59.8 %	2.2 %	38.0 %
no shared hit & B	24.3 %	89.0 %	3.2 %	7.7 %
Conversion in Layer 1, First Hit in Layer 2				
total	9.1 %	86.2 %	9.9 %	3.9 %
In Total	100 %	95.6 %	1.2 %	3.3 %

Conversion in Layer

The overall fit convergence for photon conversion in layers is at 96.9% and therefore slightly lower than for conversion in the target. Most events have tracks with two transverse intersections (98.4%). For these events, convergence is at 97.0% while only 90.6% of the events in configuration B converged. Again, the dominant reason for fit failure is the inability to find the right kink angles.

If the two electron tracks from photon conversion in one of the detector layers have not separated enough, they hit the same pixel meaning the two tracks *share* their first hit. This happens in 94% of photon conversions in the layer. For those conversion events, the vertex fit converged 98.8% of the time. If the two tracks do not have a shared hit, convergence is only at 66.5%. In these cases, the initial vertex estimate can lie outside of the detector layer in which the first hits are detected. χ^2 is reduced by correcting the vertex fit to be even further outwards. This works as long as kink angles can be found to bend the tracks to these vertex positions. If the vertex position is probed too far outside, no kink angles can bend the tracks to force them to intersect with that position.

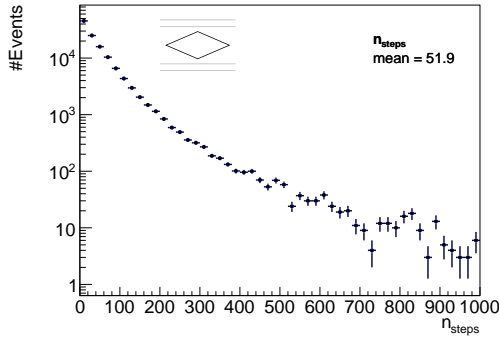
5.4.2. Number of Steps and Correction Size

The number of iterations required for the fit to converge n_{steps} and the size of the last vertex correction $|\vec{d}v_{\text{last}}|$ are important quantities to verify the fit performance. The iterative vertex fit is only considered converged if a vertex correction below 1 μm is achieved in one thousand or fewer iterations.

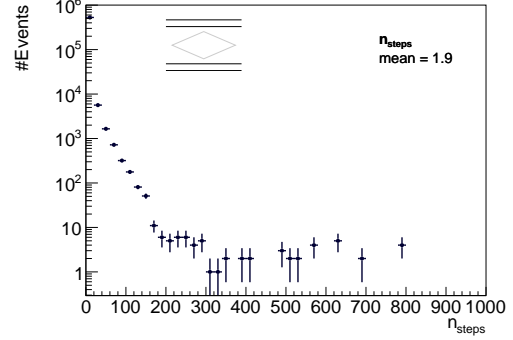
In figure 5.5, the distributions for n_{steps} and $|\vec{d}v_{\text{last}}|$ are shown for photon conversion in the stopping target and in the pixel detector layers. The average number of iterations needed for convergence in the target 51.9 is well below the limit of $n_{\text{steps}}^{\text{max}}$. The average vertex correction before convergence is 0.86 μm .

In the case of photon conversion in one of the layers, the first vertex correction is close to zero in many cases. Since these corrections are well below the threshold of $\delta_{\text{max}} = 1 \mu\text{m}$, the fit is considered converged in this case. This behaviour occurs for photon conversion events with shared hits. The continuous part of the distributions corresponds mostly to conversion events without shared hits.

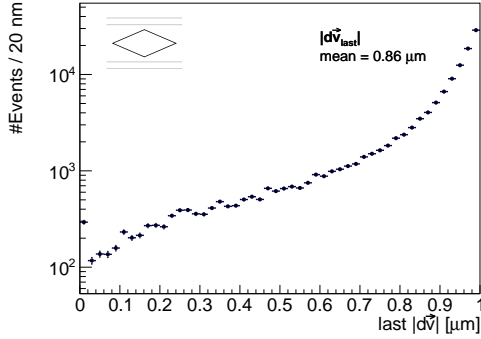
5. Photon Studies



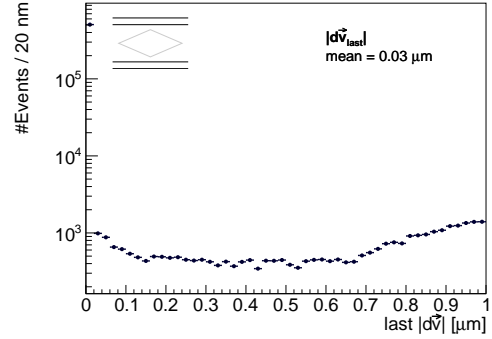
(a) Number of iterations before convergence in target.



(b) Number of iterations before convergence in layers.



(c) Last vertex correction before convergence in target.

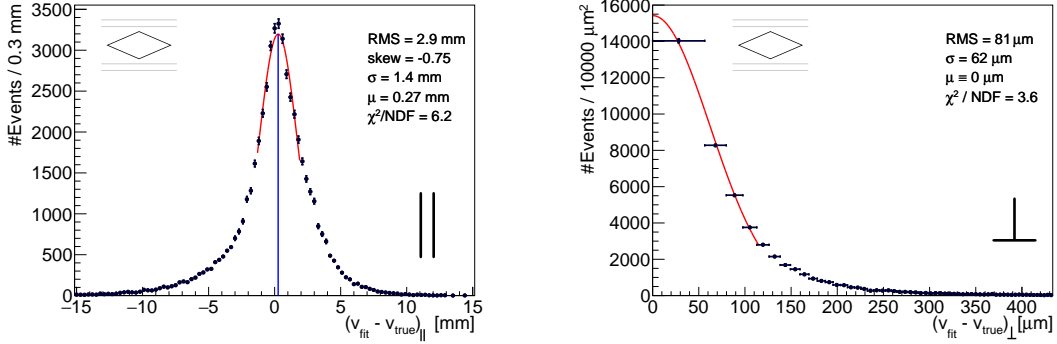


(d) Last vertex correction before convergence in layers.

Figure 5.5.: The number of iterations and the last vertex correction before convergence in the target and first two detector layers. Note that for conversion in the layers, almost all events are in the bins at $n_{\text{steps}} = 0$ and $|\vec{d}v_{\text{last}}| = 0$. The upper boundaries of $n_{\text{steps}} = 1000$ and $|\vec{d}v_{\text{last}}| = 1 \mu\text{m}$ are appropriate limits chosen.

5.4.3. Resolutions

A vertex position \vec{v}_{fit} that minimises the χ^2 -function is reconstructed using the vertex fit described in chapter 4. Various quantities can be reconstructed from the vertex position and the track parameters of the two electrons. Studies concerning these reconstructions are presented and compared to Monte Carlo truth information in the following section.



(a) Parallel part of the vertex position residuals. (b) Perpendicular part of the vertex position residuals. The binning is chosen so that each bin corresponds to an annulus of $10\,000\ \mu\text{m}^2$.

Figure 5.6.: Residuals of the vertex position for photon conversion in the target material, projected on the photon momentum (left) and on the plane transverse to it (right). The red lines show Gaussian fits. In 5.6a, the mean value from the Gaussian fit is marked with a blue line, in 5.6b, the mean value is fixed to $\mu \equiv 0$.

5.4.4. Spatial Resolution

The actual vertex position is of great interest and can be used for instance to identify displaced vertices from particles with finite lifetime. For photon conversion, the results differ significantly between conversion in the stopping target material and conversion in one of the pixel detector layers. Therefore, the resolutions for the vertex position are presented independently for these cases.

Photon Conversion in Target

As pointed out in section 5.3, the shape of the χ^2 -minimum suggests a difference between the photon direction and the transverse plane perpendicular to it. Distances projected on the photon momentum vector are denoted as *parallel* or with the symbol \parallel , while distances projected on the transverse plane are denoted as *perpendicular* or with the symbol \perp .

The vertex position residuals for photon conversion in the target are shown in figure 5.6. For the parallel part of the residuals, the Gaussian fit results in a

5. Photon Studies

standard deviation of $\sigma = 1.4$ mm, while the histogram has an RMS of more than two times the Gaussian standard distribution with $\sigma_{\text{RMS}} = 2.9$ mm. Gaussian fits are performed to obtain an estimate for the width of the distribution in the central region. Comparison of the standard deviation obtained by the Gaussian fits and the RMS of the two histograms shows that the tails of the distributions are more pronounced than described by a Gaussian distribution.

For the perpendicular part of the residuals, the binning is chosen so that each bin covers the same area of $10\,000\ \mu\text{m}^2$. Since the perpendicular part is non-negative by definition, a Gaussian distribution with a fixed mean of $\mu \equiv 0$ is used for the fit. Again, the RMS of the histogram of $\sigma_{\text{RMS}} = 81\ \mu\text{m}$ is larger than the fitted standard deviation of $\sigma = 62\ \mu\text{m}$, although these two values are closer than in the parallel part of the residuals.

Furthermore, the distribution of the parallel residuals is left-skewed with a skewness of

$$\frac{m_3}{m_2^{3/2}} = \frac{m_3}{\sigma^3} = -0.75, \quad (5.11)$$

where $m_i = \frac{\sum_{j=1}^n (x_j - \mu)^j}{n}$ is the i -th moment about the mean μ of a distribution.

Examination of the parallel part of the residuals for tracks in configuration A and B separately shows that the residual distribution is much more skewed for configuration A, i.e. the case that the tracks have two intersections in transverse projection (see figure B.1 in the appendix). The skewnesses for the two different configurations are as follows:

$$\text{Config. A : } \frac{m_3}{m_2^{3/2}} = -0.78 \quad (5.12)$$

$$\text{Config. B : } \frac{m_3}{m_2^{3/2}} = -0.12. \quad (5.13)$$

Not only is the residual distribution for configuration A more skewed than for configuration B, it is also broader. The RMS values for each histogram are:

$$\text{Config. A : } \sigma_{\text{RMS}} = 3.5 \text{ mm} \quad (5.14)$$

$$\text{Config. B : } \sigma_{\text{RMS}} = 1.7 \text{ mm}. \quad (5.15)$$

The broader and more asymmetric shape of the distribution for configuration A can be explained by the shape of the χ^2 -minima. In the case of two transverse intersections of the electron tracks, the χ^2 -minimum typically lies close to one of these points (see also figure 5.3). Looking at the two spherical coordinates φ and θ separately illustrates this. At the points of transverse intersection, by definition no scattering angles in φ have to be introduced to let the two tracks intersect. Scattering angles in θ are smaller for the intersection that is further away from the hit positions. This corresponds to the direction opposite of the photon momentum, i.e. negative values of $(\vec{v}_{\text{fit}} - \vec{v}_{\text{true}})_{\parallel}$. This produces the left-skewedness of the residual distribution in the configuration with two transverse intersections of the tracks (see figure B.1a). Of course, in the real fit procedure, correlations between the two scattering angles are taken into account.

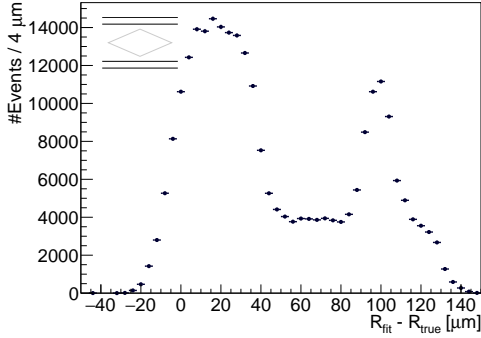
In the case of no transverse intersections (configuration B), the χ^2 -minimum typically is usually found near the point of transverse closest approach of the two tracks. Therefore, no direction along the photon momentum is preferred over the other and thus the residual distribution in figure B.1b is close to symmetric.

Photon Conversion in Layers

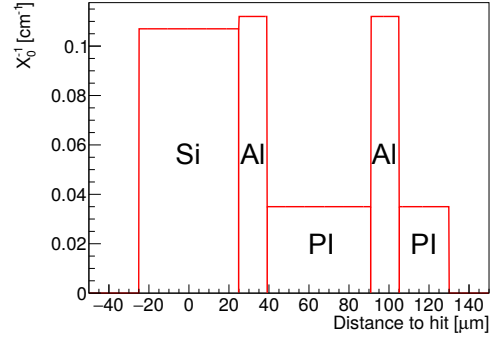
For shared hits, the fit converges in the position of this hit, which is in the centre of the silicon part of the pixel detector. The residuals of the vertex fit are determined by the detector geometry in this case. Therefore, the representation of the residuals is divided into the radial component $R = \sqrt{x^2 + y^2}$ (figure 5.7a) and the z -component (figure 5.7c and 5.7d).

For comparison, figure 5.7b shows the inverse radiation length of the pixel detector layer as it is implemented in the simulation. The origin is set in the centre of the silicon and the distance is measured in inwards direction. The pixel detector layer consists of a 50 μm silicon pixel detector simulated as pure silicon, an HDI simulated as two 14 μm aluminium layers separated by 52 μm polyimide (PI) and an additional 25 μm thin polyimide foil for mechanical support. The conversion probability density is proportional to the inverse of the radiation length X_0 , therefore one sees a clear correspondence between figures 5.7a and 5.7b. As the two innermost layers are an octagonal and a decagonal prism respectively, photons

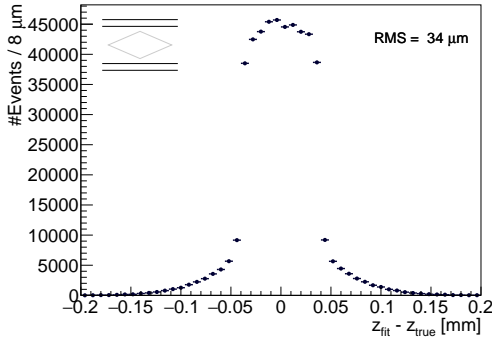
5. Photon Studies



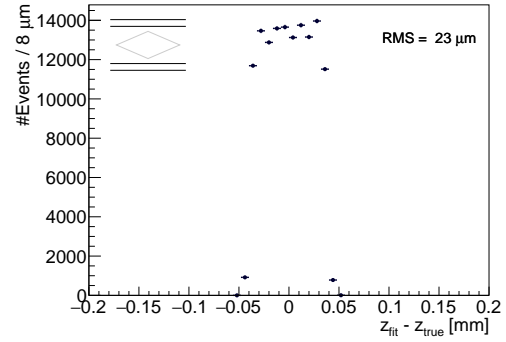
(a) Residuals in the **transverse** plane.



(b) Inverse radiation length across a pixel layer [7]. The origin is centred in the active silicon volume.



(c) Residuals in **z-direction**.



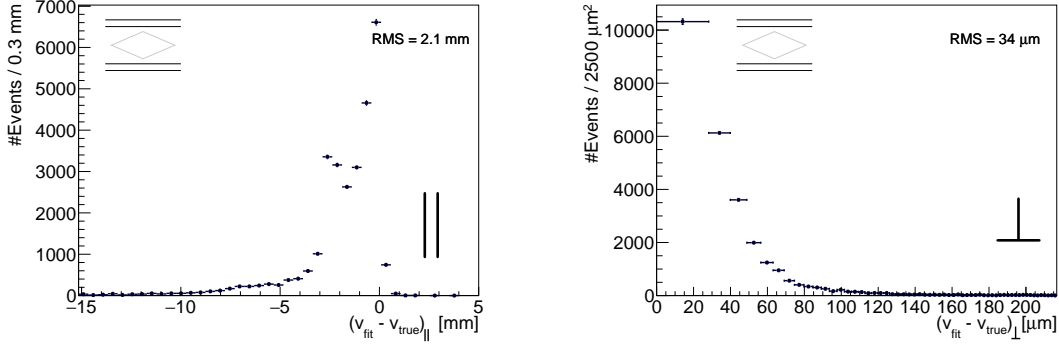
(d) Residuals in **z-direction** with a cut on $|\lambda_\gamma| < 0.1$.

Figure 5.7.: Residuals of the vertex fit for photon conversion in the pixel detector.

coming from the centre of the detector generally are not perpendicular to the pixel layers. For the innermost layer, the azimuthal impact angle is in the range of 67.5° to 112.5° . Therefore, the structures seen in figure 5.7b do not represent a purely horizontal cross section of the pixel layer as seen in in figure 5.7a, but an overlay of projections deviating by up to 22.5° from the perpendicular cross section.

As a minimum energy deposition of 5 keV in the silicon is required, the detector efficiency is dependent on the path length. In figure 5.7a, shorter path lengths in the silicon correspond to the left side of the histogram.

Figure 5.7c shows the residuals of the z -coordinate of the vertex position.



(a) Parallel part of the vertex position residuals. (b) Perpendicular part of the vertex position residuals. The binning is chosen so that each bin corresponds to an annulus of $2500 \mu\text{m}^2$.

Figure 5.8.: Residuals of the vertex position for photon conversion in the first or second layer, projected on the photon momentum (left) and on the plane transverse to it (right). Only conversion events without shared hits are selected.

Besides a broad peak in the interval between $-40 \mu\text{m}$ and $40 \mu\text{m}$, there are tails towards both sides. For figure 5.7d, an additional cut on the photon direction of $|\lambda_\gamma| < 0.1$ is applied to select photons with only little momentum in z -direction. With the additional cut, the tails from figure 5.7c vanish, indicating that they belong to events with small impact angles. One can directly relate the width of the distribution to the $80 \mu\text{m}$ pixel size of the detector. The RMS of $23 \mu\text{m}$ also matches the expected resolution obtained from a uniform distribution with a width of $80 \mu\text{m}$:

$$\sigma = 80 \mu\text{m} / \sqrt{12} \approx 23 \mu\text{m}. \quad (5.16)$$

Conversion in Layers Without Shared Hits

If a photon converts in one of the pixel detector layers and the tracks separate well enough, two neighbouring pixels can be hit. Similar to conversion in the target, the uncertainties are determined by the photon direction (see the residuals in figure 5.8). With very few exceptions, all residuals $(\vec{v}_{\text{fit}} - \vec{v}_{\text{mc}})_{\parallel}$ are negative. In the geometry of this study, negative residuals express a shift *inwards*. Since hit

5. Photon Studies

position uncertainties are not taken into account by the vertex fit, large scattering angles would be necessary to bend the tracks onto the true vertex position inside the layer. By moving the vertex position towards the inner part of the detector, the bending angles, and thus, χ^2 are reduced. The second peak at about -2 mm consists almost exclusively of events with configuration A. It can therefore be assumed that in these cases, two minima exist and the fit converges in the wrong one. Without a shared hit, the RMS of $\sigma_{\text{RMS}} = 2.1$ mm of the parallel part is significantly higher than with a shared hit. The assumption that the spatial uncertainty of the hit position is negligible does not hold for conversion inside the layers. A correct treatment of these cases would require a modified vertex fit taking hit uncertainties into account.

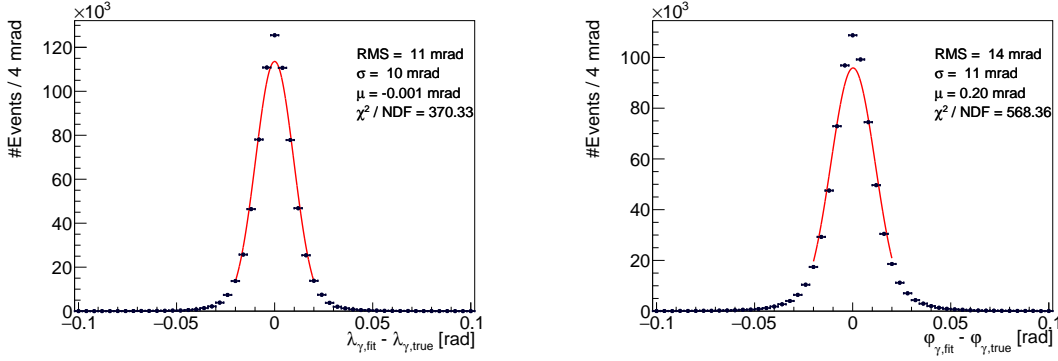
The residuals of the perpendicular part, shown in figure 5.8b with an RMS of $\sigma_{\text{RMS}} = 34$ μm are very small compared to the parallel part. The RMS is equal to the RMS in z -direction for shared hits, indicating that only the resolution parallel to the photon direction is affected by the absence of a shared hit for conversion in the layer.

5.4.5. Angular Resolution

Photon conversion vertices are generally displaced from the decay emitting the photon, e.g. π^0 Dalitz decays or in the search for $\mu \rightarrow e\gamma$. For full reconstruction of the original decay, the photon must be extrapolated back towards the vertex of the initial (radiative) decay. To suppress combinatorial backgrounds, a good angular resolution is desirable.

To reconstruct the direction of the photon, the electron and positron tracks are extrapolated back to the point of transverse closest approach to the reconstructed vertex position.

The residuals of the polar and azimuthal angles obtained this way are shown in figure 5.9. The standard deviations obtained by fitting normal distributions to the central part of the distributions are $\sigma_\lambda = 10$ mrad and $\sigma_\varphi = 11$ mrad. The RMS of the histograms are larger with $\sigma_\lambda^{\text{RMS}} = 11$ mrad and $\sigma_\varphi^{\text{RMS}} = 14$ mrad. The discrepancy of the standard deviations and the large χ^2 of the Gaussian fits match the optical impression that the distributions are indeed not Gaussian and the fits



(a) Residuals for the reconstructed polar angle λ . (b) Residuals for the reconstructed azimuthal angle φ .

Figure 5.9.: Residuals for the reconstruction of the photon direction. The red lines are Gaussian fits with the standard deviations given in the plots.

are not to be understood as anything more than an estimate for the width in the central part of the distribution.

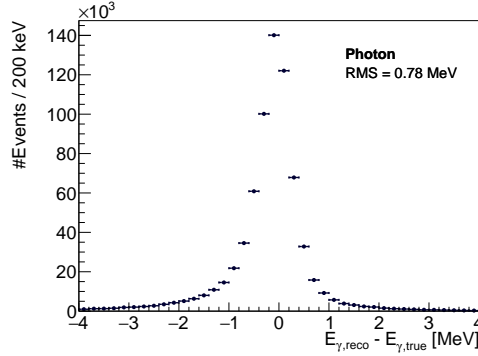
No difference in resolution has been observed between conversion in the target and in the pixel layers. Misreconstruction of the vertex position along the photon direction leads to misreconstruction of the directions of the individual tracks at the point of convergence.

5.4.6. Energy Resolution

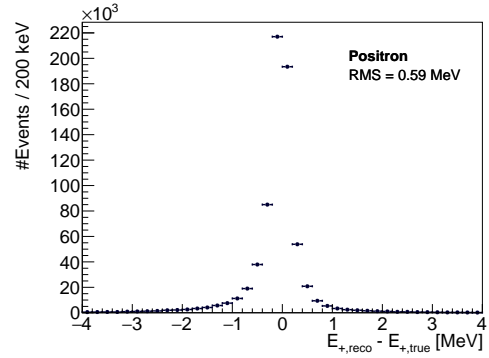
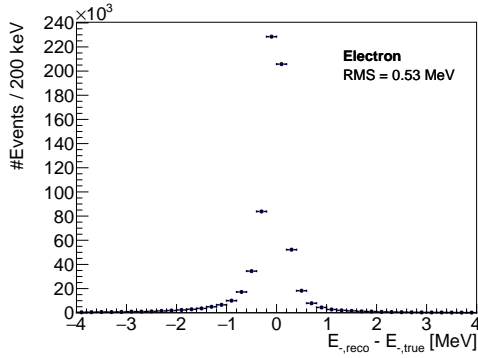
Reconstruction of the photon energy is necessary to reconstruct the total energy of an initial particle. In the decay $\mu \rightarrow e\gamma$, the photon would have an energy of half the muon mass. High precision is needed to distinguish signal from background events.

In the process of photon conversion in the Coulomb field of a nucleus, only a negligible amount of energy is transferred to the nucleus. Therefore, the photon energy E_γ can be directly reconstructed as the sum of the energies of the electron and positron $E_- = \sqrt{p_-^2 + m_e^2}$ and $E_+ = \sqrt{p_+^2 + m_e^2}$ with the respective momenta p_\pm and the electron mass m_e . The momenta are provided by the track reconstruction (see section 3.5).

5. Photon Studies



(a) Residuals for the reconstructed photon energy.



(b) Residuals for the electron energy provided by the track reconstruction. (c) Residuals for the positron energy provided by the track reconstruction.

Figure 5.10.: Residuals for the photon energy E_γ , the electron energy E_- and the positron energy E_+ .

The residual distribution of the photon energy is shown in figure 5.10a. The RMS is $\sigma_\gamma^{\text{RMS}} = 0.78 \text{ MeV}$. For the sake of completeness, figures 5.10b and 5.10c show the residual distributions for the electron and positron energies. Calculating the uncertainty one would expect from error propagation using the RMS of these momenta σ_\pm , one obtains

$$\sigma_\gamma = \sqrt{\sigma_+^2 + \sigma_-^2} \approx 0.79 \text{ MeV}, \quad (5.17)$$

which is close to the observed RMS. The vertex fit has no influence on the reconstruction of the energy, therefore uncertainties are solely due to track reconstruction.

Since the momentum resolution of electrons in Mu3e is limited by multiple Coulomb scattering, the energy resolution for photons is expected to be worse for lower photon energies.

5.4.7. Invariant Mass Resolution

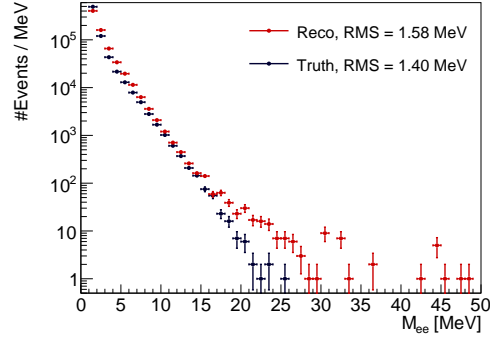
The invariant mass of an electron-positron system is of great interest and can be used for bump searches in π^0 Dalitz decays and for rejection of Bhabha scattering backgrounds (see section 5.5.2).

In the same way one reconstructs the momentum of the photon, one can reconstruct the invariant mass M_{ee} of the electron-positron system. Figure 5.11 shows both the true and the reconstructed distributions for this invariant mass M_{ee} of photon conversion events.

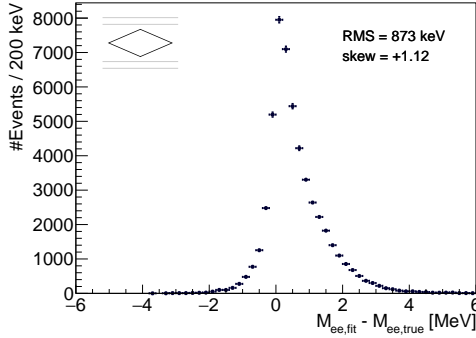
The residuals of the reconstructed invariant mass for conversion in the target and in the layer are shown in figure 5.11b and 5.11c, respectively. Both residual distributions are right-skewed with skewnesses of 1.14 and 1.95 for conversion in the target and in the layers, respectively. The invariant mass is reconstructed from the opening angle between the electron and the positron, which is close to zero. Only very small angular misreconstructions can actually decrease the invariant mass further. Large misreconstructions of the opening angle in either direction lead to a reconstructed invariant mass that is too large. Therefore, the residual distribution $M_{ee,fit} - M_{ee,true}$ is skewed towards positive values.

The RMS for the residual distributions for conversion in the target is 873 keV, while the RMS for conversion in the layer is at 513 keV. Since the vertex position is known with a higher precision for conversion in the layer, the invariant mass can be reconstructed with higher precision as well.

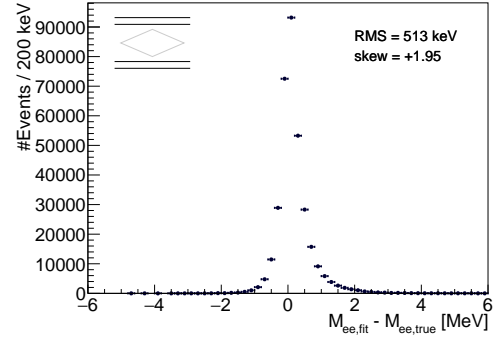
5. Photon Studies



(a) True and reconstructed invariant mass for the e^+e^- system, combined for conversion in the target and in the layer.



(b) Invariant mass residuals for conversion in the target.



(c) Invariant mass residuals for conversion in one of the layers.

Figure 5.11.: Distributions and residuals of the invariant mass of the electron-positron system.

5.4.8. Chi-squared Revisited

The χ^2 -distribution for one degree of freedom is expected to peak at $\chi^2 = 0$. For photon conversion in the stopping target material, the distribution shown in figure 5.12a matches that expectation. The vertex finding efficiency (shown in figure 5.12b) reaches 90 % for a cut at $\chi^2 = 6$.

Selecting events with a low χ^2 does not improve the vertex resolution (see figure 5.12c and B.2 through B.5 in the appendix). Instead, a stricter χ^2 -cut favours events with a broader and more asymmetric residual distribution of the

parallel part. With a cut of $\chi^2 < 1$, the skewness of the distribution is -0.88 (see figure B.2a), whereas the skewness lies closer to zero for looser cuts.

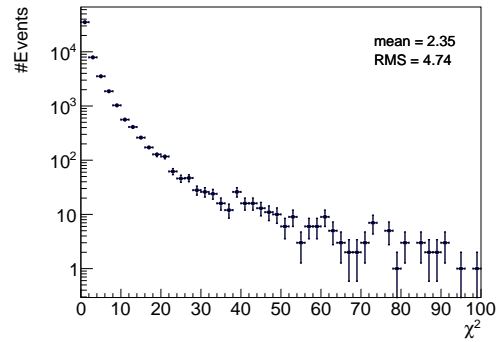
5.4.9. Summary

With a fit convergence in 95.6 % of all photon conversions with two reconstructed tracks, it is safe to say that the fit converges reliably.

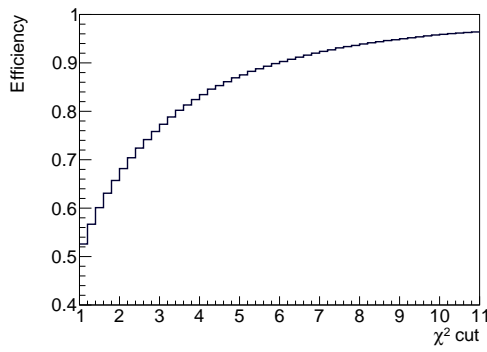
For photon conversion in the material of the stopping target, convergence is even better at 99.1 %. The spatial resolution perpendicular to the photon of well below $100\ \mu\text{m}$ is more than one magnitude better than in the direction parallel to the photon. Photon conversion in the pixel detector layers can be reconstructed with the vertex fit as well. In the case where the two tracks of the electron and the positron share hits, the fit converges in the position of the hit.

After reconstruction of the vertex position, different quantities can be reconstructed by extrapolation of the electron and positron tracks to the found vertex. The invariant mass of the electron-positron system can be reconstructed with a precision better than 1 MeV for conversion in the target and a precision of about 500 keV for conversion in the pixel layers. For the photon energy, no information about the fit position is necessary and its resolution is limited by the momentum resolution of the individual electron tracks. No difference between the angular resolution for convergence in the target and in the pixel layers has been observed. In both cases, the azimuthal and polar angle can be reconstructed with a precision of 10–15 mrad. The photon energies in this study are between 50 and 60 MeV.

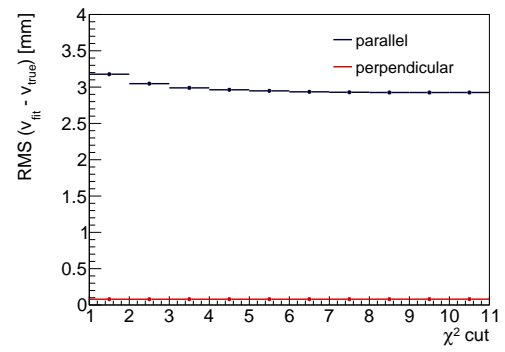
5. Photon Studies



(a) χ^2 -distribution.



(b) Efficiency.



(c) The RMS of the parallel and perpendicular parts of the residual distributions of the vertex position.

Figure 5.12.: Distribution of χ^2 of the MS vertex fit and vertex selection efficiency for different cuts on χ^2 .

5.5. Photons from Muon Decays in Mu3e

So far, all studies of the vertex fit were performed using a photon spectrum in the range of 50 to 55 MeV. In reality, most photons expected in the Mu3e experiment have energies below that. To account for this, vertices from photon conversion of photons from radiative muon decays $\mu \rightarrow e\nu\nu\gamma$ are reconstructed.

The Mu3e framework allows for generation of one guaranteed radiative muon decay per 50 ns time frame. Ten million of such frames are generated. The minimum photon energy for the generated decays is set to 20 MeV, since photons below that energy cannot produce two conversion electrons that reach the outermost detector layer and are thus outside of the acceptance. The branching ratio for radiative muon decays with $E_\gamma > 20$ MeV is calculated to be 0.44(12) % by Monte Carlo integration of the differential branching ratio of the radiative decay, normalised to 1.4(4) % at $E_\gamma > 10$ MeV [7]. Therefore, this sample corresponds to the amount of radiative decays one expects in a total of $2.27(65) \times 10^9$ muon decays. All simulated muons are polarised in negative z -direction which is also the direction of the magnetic field.

5.5.1. Geometrical Acceptance for Radiative Decays

Only in 406 out of 10^7 frames, both the electron and positron from the photon conversion have transverse momenta large enough to produce hits in all four detector layers of the central detector. Conversion events where the electron and the positron share the first hit of their respective tracks are not considered. Also, an extension of the track reconstruction allowing reconstruction of tracks starting in the second layer is not implemented in this study. If these two features are implemented, photon reconstruction is extended by a factor of 9.56 (see table 5.2, the cases considered here make up 10.46 % of all reconstructable events).

Therefore, one can expect $9.56 \cdot (406 \pm 20)$ reconstructable radiative muon decays per $2.27(65) \times 10^9$ beam muons. The probability that a single polarised muon decays emitting a high-energetic photon that converts both conversion electrons being reconstructable is equal to $(1.69 \pm 0.49) \times 10^{-6}$. The dominant uncertainty stems from the branching ratio of the radiative muon decay.

5. Photon Studies

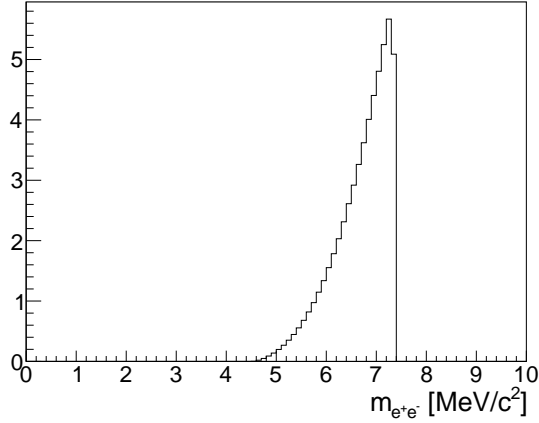


Figure 5.13.: Histogram of the simulated true invariant mass of e^+e^- pairs from Bhabha scattering of Michel positrons on electrons in the target material.

This estimation does not include tracking and vertex fitting inefficiencies. Parity violation in muon decays causes the positron to be preferably emitted in the direction of the muon spin. The beam polarisation in Mu3e is expected to be around 85 %, which would increase the amount of photons emitted in transverse direction compared to this study. Also, only tracks starting in the first detector layer are considered.

5.5.2. Bhabha Scattering Background

One important background for photon vertex finding is Bhabha scattering of positrons (for instance from $\mu \rightarrow e\nu\nu$) on electrons in the detector material. The signature of Bhabha scattering is essentially the same as for a conversion event: An electron and a positron coming from the same vertex in material with a typically small opening angle. However, Bhabha pairs have an invariant mass between 4.5 MeV and 7.4 MeV (see figure 5.13). With a resolution in the order of 1 MeV, some amount of smearing is to be expected. This has to be studied in further detail when estimating sensitivities to specific phenomena involving photon emission events. Rejection of photons with reconstructed invariant masses between 4.5 MeV and 7 MeV causes a loss of 5.2 % of true photon conversion events.

5.5.3. Internal Conversion Background

The combination of the lower-momentum positron and the electron from the radiative muon decay with internal conversion also has the same signature as photon conversion: one electron and one positron originating at the same vertex.

Unlike photon conversion, these decays can only occur in places irradiated by the muon beam of Mu3e, which is mostly the stopping target. A small amount of muons is expected to be stopped in the material of the innermost pixel detector layer. Therefore, internal conversion is most importantly a possible source of background for photon conversion in the target with a small share of muons stopped in the innermost pixel detector layer.

The angular distribution of these pairs is dictated by the polarisation of the muon beam. The angular distribution for photon conversion depends on the effective thickness of the material the conversion takes place in. It is possible to suppress these background events in the reconstruction. If a second positron can be traced to the same vertex, the event can be rejected as a photon candidate.

6. Dalitz Decay Studies

This chapter presents first studies that investigate whether studies of neutral pion Dalitz decays $\pi^0 \rightarrow ee\gamma$ are feasible with the Mu3e detector.

For studies involving Dalitz decays, all three decay particles have to be reconstructed and a common vertex must be found. Electrons and positrons are reconstructed as tracks in Mu3e, and the possibility to reconstruct photons in the Mu3e detector is discussed in chapter 5.

In the following chapter, an estimation for the acceptance of Dalitz decays is given and the reconstruction of the decay vertex from just the electron and the positron is studied. The resolution of the invariant mass of the pair is studied, which is crucial for studies of the TFF and for searches for dark photons in Dalitz decays. Furthermore, different approaches for the combination of the two electrons and the reconstructed photon are discussed.

6.1. Simulation

Baseline of these studies is the (unmodified) version of the Mu3e detector as described in chapter 3.3. Neutral pions are generated on the stopping target via primary particles with the same stopping distribution a muon beam would have. Simulated are kinematics for the two production channels discussed in chapter 2.3. Pions produced via the charge exchange reaction (CEX) $\pi^- + p \rightarrow \pi^0 + n$ have a kinetic energy of 2.88 MeV and are isotropically emitted. If pions are produced in association with the Δ^{++} resonance $\pi^+ + p \rightarrow \pi^0 + \Delta^{++}$, they have a forward momentum of 49 MeV (see also section 2.3).

Simulating pions this way also brings the same inefficiencies that are expected for a muon beam in Mu3e: Some primary particles do not reach the stopping target or pass the target without being stopped. Furthermore, a small fraction of primary

6. Dalitz Decay Studies

particles produces the pions in-flight. Since the kinematics are defined in the rest system of the primary particles, pions produced in-flight have a small boost in positive z -direction.

Backgrounds from the charged pion beams or Δ baryons and beam contamination with electrons or muons are not simulated. Only Dalitz decays are simulated, therefore none of the pions decay into two photons.

6.2. Acceptance for Dalitz Decays

Acceptance for Dalitz decays can be divided into two parts: the geometric acceptance of the electron-positron pair, and the successful reconstruction of the photon. Four tracks in total are expected for one complete Dalitz decay with photon conversion. Since the Mu3e detector is optimised for low material budget, the probability for a photon to convert is fairly low. The estimation of acceptance in the following section is factored and calculated individually for the Dalitz pair and the photon.

6.2.1. Geometric Acceptance of the Electron-Positron Pair

Similar to section 5.5.1, ten million 50 ns time frames with one pion each are simulated. Particles with momenta below 5 MeV are omitted in the simulation since they are not within the range of acceptance. Therefore, it can occur that only one of the two Dalitz electrons is simulated for one Dalitz decay. Finally, one can count how many frames have two Dalitz electron tracks that produce at least four

Table 6.1.: Geometric acceptance of the Mu3e detector for the electron-positron pair from $\pi^0 \rightarrow e^+e^-\gamma$. Shown are results for the kinematics of CEX reaction and pion production in association with Δ^{++} baryons.

	CEX	Δ resonance
simulated	10 000 000	10 000 000
decays on target	7 802 747	7 800 523
two tracks	7 128 175	7 134 673
both have four hits	3 579 333	3 383 101
acceptance fraction	$(45.87 \pm 0.02) \%$	$(43.37 \pm 0.02) \%$

hits, which is the minimum number of hits to reconstruct a track. The acceptance fraction f is then given as the following ratio:

$$f = \frac{\# \text{ frames with two Dalitz electrons with four hits}}{\# \text{ frames with a Dalitz decay}}. \quad (6.1)$$

The geometric acceptance for Dalitz pairs with kinematics corresponding to CEX and the production via the Δ resonance is summarised in table 6.1. In both cases, the acceptance is more than 40%. For CEX kinematics, the acceptance is slightly higher with $(45.87 \pm 0.02)\%$ compared to $(43.37 \pm 0.02)\%$ from pions created in association with Δ baryons. Note that these results do not take tracking and vertex finding efficiency into account.

6.2.2. Acceptance Including Photons

The full reconstruction of Dalitz decays requires not only reconstruction of the electrons, but of the photon as well. The reconstruction of photons in the Mu3e detector is covered in chapter 5. Without any modifications to the detector, the acceptance for photons is well below one percent, mainly due to the small conversion probability inside the detector. The results in table 6.2 suggest a very low acceptance fraction.

It is to be noted that in this analysis, none of the aforementioned improvements are utilised. Therefore, all tracks have a hit in the innermost pixel detector layer and shared hits are not considered. This corresponds to photon conversion in the target and 6% of the conversions in the innermost layer or 10.6% of what would be detectable with the aforementioned improvements of track reconstruction (see table 5.2). This results in a factor of 9.56, which accounts for the improvements.

6. Dalitz Decay Studies

Table 6.2.: Geometric acceptance of the Mu3e detector for the photon from $\pi^0 \rightarrow e^+e^-\gamma$ for the kinematics corresponding to the two main production channels. The corrected fraction takes improved track reconstruction into account.

	CEX	Δ resonance
simulated	10 000 000	10 000 000
decays on target	7 802 747	7 800 523
two conv. tracks	10 472	11 165
both have four hits	2 157	2 127
acceptance fraction	$(0.0276 \pm 0.0006) \%$	$(0.0273 \pm 0.0006) \%$
corrected fraction	$(0.264 \pm 0.006) \%$	$(0.261 \pm 0.006) \%$

6.3. Dalitz Pair Vertex Fit

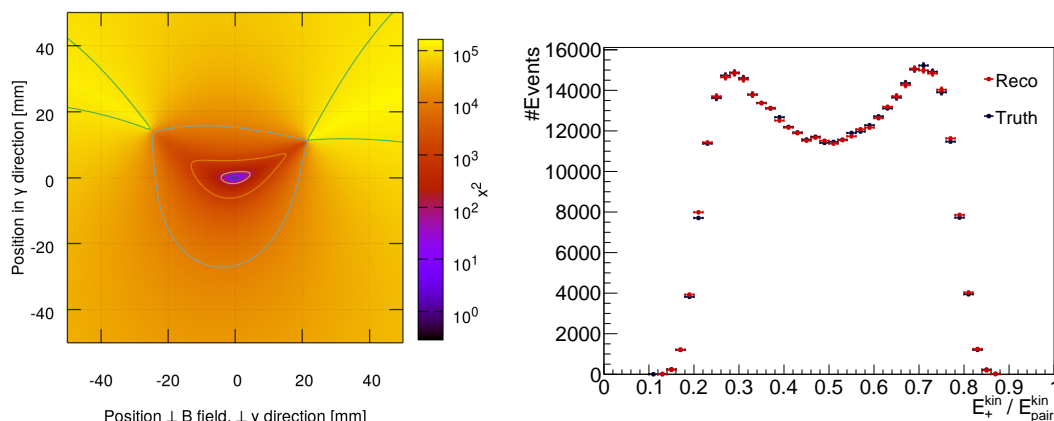
For finding the vertex of the decay $\pi^0 \rightarrow ee\gamma$ without information from the photon, the vertex fit algorithm described in chapter 4 is applied on the electron-positron pair. In principle, the results from chapter 5 apply to the reconstruction of the electron-positron pair from Dalitz decays.

Dalitz pairs are often asymmetric with one electron having significantly more kinetic energy than the other. The ratio of the kinetic energy of the positron E_+^{kin} to the kinetic energy of the pair $E_{\text{pair}}^{\text{kin}}$ is shown in figure 6.1b.

A χ^2 -map in the fashion of section 5.3 is shown in figure 6.1a. The χ^2 -minimum is close to the true decay vertex, which lies in the origin of this map. Since the opening angle between the two tracks at the vertex is 134.5° , the χ^2 -minimum is not elongated in the direction of the total momentum.

6.3.1. Vertex Resolution

For low invariant masses, the two Dalitz electrons are very parallel. As discussed in chapter 5, this causes the uncertainties parallel to the (virtual) photon momentum to be significantly larger than perpendicular to it. The higher the invariant mass, the larger opening angle between the two particles becomes. Larger opening angles increase precision parallel to the momentum of the electron-positron system (see figure 6.2, and C.3 and C.4 in the appendix)). The parallel vertex resolutions vary



(a) χ^2 map for a Dalitz decay with an invariant mass of the e^+e^- system of $M_{ee} = 71.85$ MeV. The opening angle between the electron and the positron is 134.5° . The decay vertex is at $(0,0)$. See also section 5.3.

(b) Energy-partition parameter $x = E_+^{\text{kin}}/E_{\text{pair}}^{\text{kin}}$ of the Dalitz decay. Note that the drop for $x < 0.3$ and $0.7 < x$ is due to the geometric acceptance of the single electron tracks.

Figure 6.1.: Reconstruction of the electron-positron pairs from Dalitz decays.

between less than 1 mm and up to over 4 mm for small invariant masses.

The perpendicular part of the resolution (also shown in figure 6.2) is always in the order of $200\ \mu\text{m}$ with only a small dependence on the invariant mass. As shown in figure C.5 and C.6 in the appendix, the vertex resolution is worst for invariant masses between 60 MeV and 80 MeV.

6.3.2. Invariant Mass

A Dalitz pair stems from internal conversion of a highly virtual photon. Therefore, the invariant mass of a Dalitz pair (shown in figure 6.3a) can generally be much higher than the invariant mass of conversion of a real photon with an upper limit of the pion mass. The residual distribution has an RMS of 1.64 MeV and is slightly right-skewed with a skewness of 0.54 (see 6.3b). This is mainly due to events with small invariant masses and correspondingly small opening angles between the two electrons (see figures C.1 and C.2 in the appendix). Misreconstruction of an opening angle close to zero leads to an overestimation in both directions. For

6. Dalitz Decay Studies

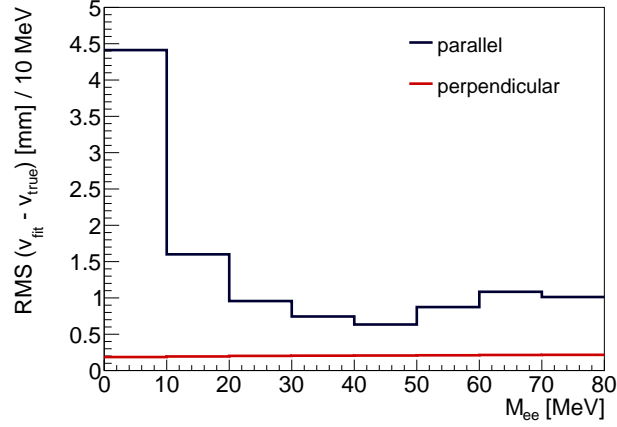


Figure 6.2.: The RMS of the residual distribution of the vertex resolution parallel and perpendicular to the total momentum of the e^+e^- system as a function of the invariant mass M_{ee} .

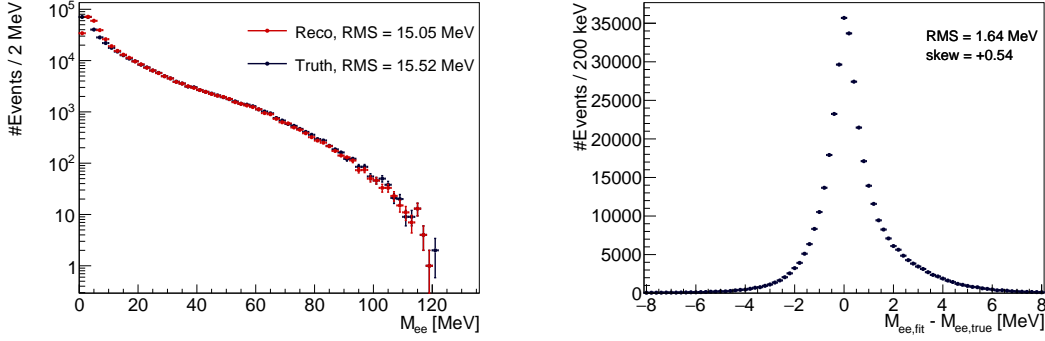
events with an invariant mass of larger than 10 MeV, the residual distribution is left-skewed.

6.4. Reconstruction of Pion Decays

Full reconstruction of the Dalitz decay is necessary to identify the pion and to suppress backgrounds. The energies of all three particles must add up to the total energy of the pion, the momenta must add up to the momentum expected from the production mechanism and the invariant mass of all three particles must match the rest mass of the pion.

After reconstruction of the photon, e.g. the way studied in chapter 5, a common vertex for the photon and the two electrons from the Dalitz decay has to be found.

The two electron tracks and the photon can be combined with using a modified multiple scattering vertex fit that allows for straight tracks for the photon. Reconstruction of the photon has an angular uncertainty of 10–14 mrad and a spatial uncertainty of 60–80 μm perpendicular to the photon momentum. For a significant displacement of the photon conversion vertex, the same assumptions as for the multiple scattering vertex fit can be made for the photon: The position is known with a very high precision and the only source of uncertainty is an angular



(a) Reconstructed and true invariant mass. (b) Residuals of the invariant mass.

Figure 6.3.: Spectrum and residuals of the invariant mass of the electron-positron pair from Dalitz decays.

uncertainty. That position and the angular uncertainty are provided by the photon reconstruction. For short extrapolation lengths of less than 6 mm, the spatial uncertainty is the dominant part of the uncertainty when extrapolating and cannot be neglected anymore.

Implementation of such a modified vertex fit that takes spatial uncertainties of the photon position into account and allows for straight tracks exceeds the scope of this thesis and remains to be done in future studies.

6.5. Signal vs. Background

Besides accidental background from combination of unrelated tracks, the most important background is the dominant pion decay $\pi^0 \rightarrow \gamma\gamma$. If one of these photons converts in the target region, the signature of one electron, one positron and one photon is present (see figure 6.4).

Photon conversion can only occur near material with a probability which is proportional to the effective thickness of the material for small distances and thin material. This implies displaced vertices compared to the beam profile as well as a dependence of the effective thickness of converter material. For a thin converter parallel to the z -axis, photon would be enhanced by a factor of $1/\cos \lambda$. Dalitz decay vertices can only lie within the region where the pions are produced, since

6. Dalitz Decay Studies

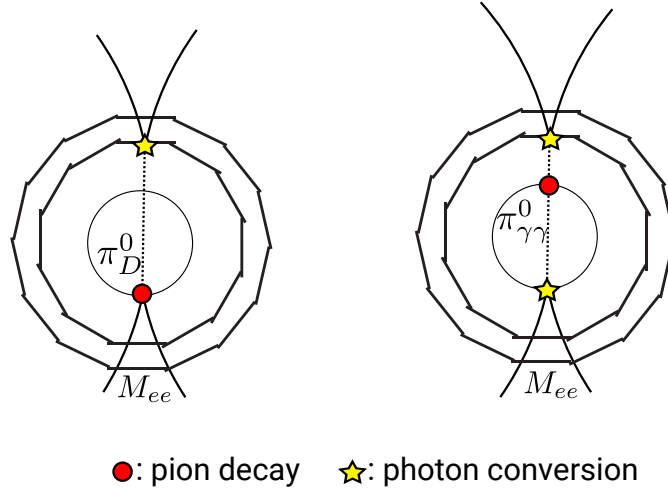
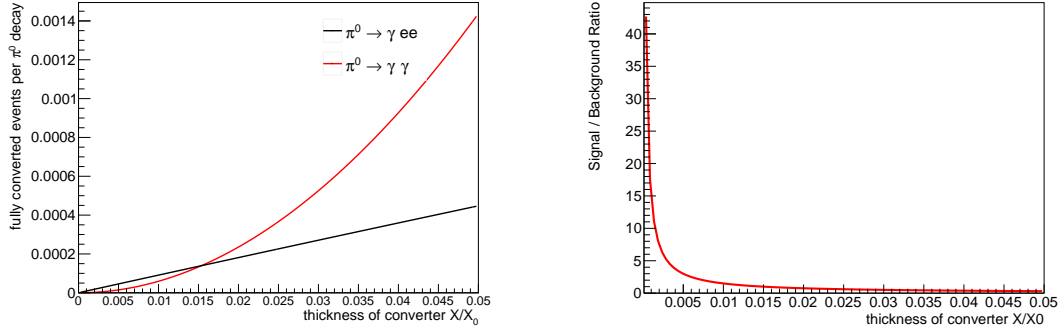


Figure 6.4.: The signal from a Dalitz decay (left) in a detector like Mu3e can be mimicked by the dominant pion decay $\pi^0 \rightarrow \gamma\gamma$ if one of the photons decays in the target region (right).

pions decay promptly.

For the reconstruction of a Dalitz decay, only one photon has to convert. Assuming the same conversion probability for all photons, the probability that both photons from the dominant decay $\pi^0 \rightarrow \gamma\gamma$ is suppressed quadratically. With a branching ratio of the Dalitz decay $\mathcal{BR} = 1.174(30)\%$, the dominant pion decay is enhanced by a factor of 84. By taking these two effects into account, one can calculate the amount of fully converted pion decays as a function of the thickness of a converter X/X_0 (see figure 6.5a). A thin converter suppresses background events effectively. Up to $X/X_0 \approx 0.015$, one would actually observe more Dalitz decays than fully converted background decays. The ratio of signal over background events is shown in figure 6.5b. The converter thickness needs to be optimised: A low ensures a pure signal while the rate of Dalitz decays increases approximately linear with the thickness.

The expected invariant mass spectrum for a converter thickness of $1\% X_0$ is shown in figure 6.6. For studies of the invariant mass spectrum, the contribution from $\pi^0 \rightarrow \gamma\gamma$ needs to be considered.



- (a) The amount of fully converted pions as a function of the material budget. (b) Ratio of fully converted Dalitz decays over fully converted background decays

Figure 6.5.: The amount of fully converted pion decays as a function of the thickness of photon converter material. The Dalitz decay $\pi^0 \rightarrow ee\gamma$ has a branching ratio of $\mathcal{BR} \approx 1.2\%$. Background decays $\pi^0 \rightarrow \gamma\gamma$ are suppressed quadratically for thin photon converters.

6.6. Conclusion

The acceptance for electron-positron pairs from Dalitz decays in the Mu3e detector lies between 40 and 50%. However, the probability to reconstruct the photon of a Dalitz decay is only about 0.26%. Taking these probabilities and the branching ratio of the Dalitz decay into account, the rate of Dalitz decays is at about 1.4×10^{-4} compared to the rate of produced pions.

Production of neutral pions in the Mu3e detector requires a target with an abundance of photons. Furthermore, to increase the rate of observable Dalitz decays, the photon conversion probability has to be increased. A liquid hydrogen target enclosed in a metal container would serve both these purposes without any modifications to the layout of the pixel detector layers. The design of such a target has to be optimised for a high conversion rate while maintaining an acceptable amount of background.

6. Dalitz Decay Studies

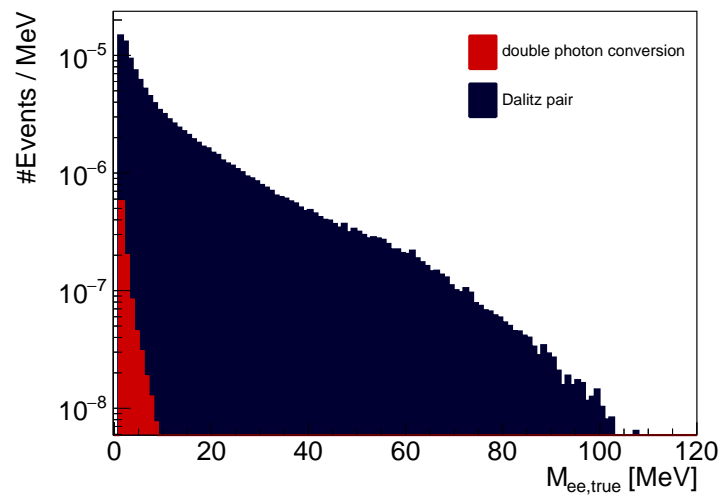


Figure 6.6.: The expected invariant mass spectrum for π^0 decays beneath a converter with a thickness of $1\text{‰} X_0$. Even though 84 times more dominant decays $\pi^0 \rightarrow \gamma\gamma$ occur, full conversion is suppressed by a factor of $9/7 \cdot 0.001$.

Part III.
Discussion

7. Discussion

The goal of the Mu3e experiment is to search for the charged lepton flavour violating (cLFV) decay $\mu^+ \rightarrow e^+e^-e^+$ with an unprecedented sensitivity of one in 10^{16} muon decays. Four barrel-shaped layers of silicon pixel sensors and two timing detector systems are used to track electrons⁽¹⁾ emerging from the target region, where the incident muons are stopped and decay at rest. The Mu3e detector is optimised for electrons with energies up to half the muon mass $m_\mu/2 \approx 53 \text{ MeV}$ (in natural units).

Only charged particles can be reconstructed in the Mu3e detector. If a photon converts to an electron-positron pair and these two particles are reconstructed, one can reconstruct the photons themselves. The opening angle between the two tracks from the electron and positron from photon conversion is small, which poses a difficulty for reconstruction. A characteristic opening angle for photon conversion is $\Theta \approx m_e/E_\gamma$, where m_e is the electron mass and E_γ is the photon energy.

With reconstructed photons in Mu3e, a wide range of tests of the Standard Model of particle physics and searches for physics beyond the Standard Model can be performed. Examples are the search search for cLFV decay $\mu^+ \rightarrow e^+\gamma$ and precision measurements of the Dalitz decay of the neutral pion $\pi^0 \rightarrow e^+e^-\gamma$.

Within the scope of this thesis, an algorithm is developed to reconstruct these events. This vertex reconstruction procedure is based on a linearised three-dimensional vertex fit, treating multiple Coulomb scattering (MS) as the only source of uncertainty. To account for nonlinearities and to improve vertex finding performance, this vertex fit is performed iteratively.

⁽¹⁾In this thesis, the term *electron* is used for both the negative electron e^- and its antiparticle, the positron e^+ .

7.1. Summary and Discussion

The vertex fit for two-prong signatures is implemented and tested using simulated photon conversion events and is furthermore applied to study the primary electron-positron pairs from simulated Dalitz decays $\pi^0 \rightarrow e^+e^-\gamma$.

Photon conversion can be reconstructed both in the passive and active material of the detector provided that the tracks of both conversion electrons are reconstructed.

In the passive part of the detector, spatial resolution for the reconstructed vertex position is determined by the direction of the photon. The largest uncertainty is parallel to the photon momentum with an uncertainty of up to about 3 mm. This is expected due to the fact that the electron tracks are very parallel. On the other hand, the uncertainty of the vertex position in directions perpendicular to the photon direction is well below 100 μm . Overestimation of the vertex corrections due to linearisation can lead to oscillations of the vertex position, that are countered by damping the corrections if an oscillation is detected. Single large overestimation of the correction can also lead to intermediate vertex positions outside of the detector for which the fit fails. This is prevented by limiting the magnitude of the vertex corrections by regularisation. An optimised regularisation scale of 1 mm is chosen. Combining these two countermeasures leads to a convergence efficiency of more than 99% for photon convergence in the muon stopping target.

For conversion in the pixel detector layers—at least when the two conversion electrons share a hit—the vertex fit converges in the position of the hit. This is the best vertex position estimate given the information of the tracks. In six percent of the conversions inside the first layer, the two tracks do not share a hit. The vertex position perpendicular to the photon can be reconstructed with a high precision of about 30 μm in this case, while the resolution parallel to the photon is 2 mm. In this case, the assumption in the fit of dominating uncertainties due to multiple Coulomb scattering is not fulfilled. Uncertainties are actually dominated by the spatial uncertainty of the hit position.

For extrapolation of a photon over distances of more than 6 mm, the dominant uncertainty is the angular uncertainty which is in the order of 10–15 mrad. Extrapolation over shorter distances is dominated by the spatial uncertainty of the

convergence position.

Quantities such as the invariant mass of the electron-positron pair can be reconstructed from the track parameters and the vertex position for further analysis. Reconstruction of the invariant mass of photon conversion pairs is possible with resolutions between 500 keV for conversion in the layers and 900 keV for conversion in the muon stopping target. The reconstructed invariant mass can be used to distinguish photon conversion from Bhabha scattering, which is a typical source of background for many decays.

Recently, the track reconstruction has been extended to allow for reconstruction of tracks starting in the second detector layer [31]. This extension is employed in this thesis. By reconstruction of these tracks the amount of reconstructable photon conversion events is increased by about 75 % from photon conversion in the second layer.

7.2. Outlook

The vertex fit as it is implemented in this thesis is well suited to reconstruct photon conversion events, but there is potential for improvement in reconstruction of the vertex position component parallel to the photon momentum. A simple solution to that would be to constrain the vertex position to be in material, although for this, detailed knowledge of the distribution of material in the detector is required. A more elegant solution would be the reconstruction of that component from the centres of the osculating circles of the two tracks.

Another improvement of the vertex fit can be achieved by taking spatial uncertainties of the hit positions into account. This allows for proper treatment of cases in which photon conversion takes place close to the pixel layers.

As of now, the implementation of the vertex fit features no optimisation of speed. Features that guarantee convergence in ill-defined configurations, namely Tikhonov regularisation and damping, slow down convergence of the fit by scaling down the vertex corrections if found necessary. For the case of shared hits, the fit procedure brings no improvement over searching for and choosing these hits as the vertex position, thus fitting can be avoided.

The reconstruction of photon conversion events can be used to identify the

7. Discussion

distribution of material inside the Mu3e detector. First studies on material mapping are already performed using the vertex fit procedure developed in this thesis [31].

Photon reconstruction is also required in the search for the cLFV decay $\mu \rightarrow e\gamma$ with a modified version of the Mu3e detector. Such modifications have been proposed in [27]. A new proposal foresees a dedicated double-layer of silicon pixel detectors with a photon converter at a radius large enough that no positrons from the target can reach this layer. To reconstruct electron tracks in just two layers, a modified track reconstruction allowing for the reconstruction of recurling tracks is necessary. If such an extension of the track reconstruction is realised, further studies of photon conversion vertex reconstruction based on these tracks need to be performed. The advantages of a dedicated photon converter are the higher yield compared to conversion in the low material Mu3e detector, and the possibility to constrain the vertex position to the converter material.

In addition, the branching fraction of the radiative muon decay $\mu^+ \rightarrow e^+\bar{\nu}_\mu\nu_e\gamma$ could be measured using this setup. In contrast to $\mu^+ \rightarrow e^+\gamma$, the photon and the electron of radiative decays are not monoenergetic. Background rejection is only possible via vertex constraints, so these measurements probably have to be performed with a lower muon rate than used in the search for $\mu \rightarrow eee$.

As a part of this thesis, neutral pions and Dalitz decays $\pi^0 \rightarrow e^+e^-\gamma$ are implemented in the Mu3e simulation. Further studies on the experimental setup for TFF measurements of neutral pions have to be concluded to determine the competitiveness of Mu3e compared to other experiments. Necessary modifications include a (hydrogen) target to produce neutral pions inside the detector. The hydrogen is contained in a metal container, which could at the same time serve as a photon converter. A linearised vertex fit with multiple scattering could also be used for the reconstruction of the rare decays $\pi^0 \rightarrow e^+e^-e^+e^-$ and $\pi^0 \rightarrow e^+e^-$.

Furthermore, the programme developed in this thesis has been successfully used for preliminary studies on the reconstruction of displaced decay vertices of dark photons [31]. The sensitivity for a bump search for dark photons in the invariant mass spectrum of the e^+e^- system of Dalitz decays using the photon reconstruction presented in this thesis has yet to be evaluated. Apart from combinatorial backgrounds, no background is to be expected for larger invariant masses. Bhabha scattering events do not contribute to the invariant mass spectrum above about

7 MeV and photon conversion is strongly suppressed at larger invariant masses.

Reconstruction of photons is an important tool for many searches for physics beyond the Standard Model as well as precision measurements that can be performed using the Mu3e detector. This thesis demonstrates the feasibility of using a linearised multiple scattering vertex fit to reconstruct photon conversion events as well as other two-prong signatures.

Part IV.
Appendix

A. Additional Calculations for the Vertex Fit

Several calculations are necessary to perform the multiple scattering vertex fit. In the Mu3e experiment, tracks have low momenta of less than 53 MeV and are highly bent in the 1 T magnetic field. The bending of the tracks creates nonlinearities which have to be taken into account when calculating the scattering angles at the first layer as a function of the vertex position $\vec{\alpha}_i \equiv \vec{\alpha}_i(\vec{v}) = (\Theta_{\text{MS},i}, \Phi_{\text{MS},i})^T$ and an explicit form of the Jacobian matrices \mathbf{J}_i .

Due to the special geometry and choice of coordinates, the weight matrices are diagonal and given by

$$\mathbf{W}_i = \begin{pmatrix} \sigma_{\Theta_i}^{-2} & 0 \\ 0 & \sigma_{\Phi_i}^{-2} \end{pmatrix} = \sigma_{\text{MS},i}^{-2} \cdot \begin{pmatrix} 1 & 0 \\ 0 & \sin^2 \theta_i \end{pmatrix} \quad (\text{A.1})$$

with $\sigma_{\text{MS},i}$ obtained from equation 4.2.

A.1. Calculating the Scattering Angles

In the following, a way of calculating the scattering angles is given by [19].

A.1.1. Transverse Scattering

The scattering angle Φ_{MS} is defined as the difference between the track directions before and after scattering (see figure A.1)

$$\Phi_{\text{MS}} := \varphi_1 - \varphi_0. \quad (\text{A.2})$$

A. Additional Calculations for the Vertex Fit

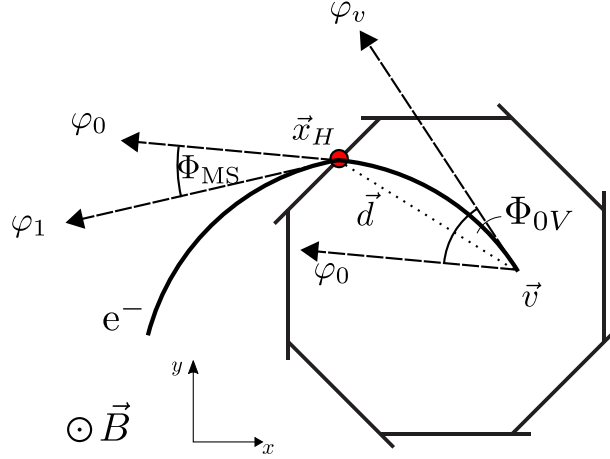


Figure A.1.: Sketch of a track scattering on the first layer in the transverse view. Shown are the vertex position \vec{v} and hit position \vec{x}_H , as well as directions at the vertex (φ_v) before (φ_0), and after scattering (φ_1). The vector \vec{d} between vertex and hit position and the scattering angle Φ_{MS} are also shown.

φ_0 depends on the probed vertex position, and φ_1 is obtained from the track reconstruction.

To obtain φ_0 , the bending angle Φ_{0V} can be defined as the difference of azimuthal angles at the first layer and at the vertex:

$$\Phi_{0V} = \varphi_0 - \varphi_v. \quad (\text{A.3})$$

This bending angle can be obtained by solving the following transcendental function [30]:

$$\sin^2 \frac{\Phi_{0V}}{2} = \frac{d^2}{4R^2} + \frac{z^2}{R^2 \Phi_{0V}^2} \sin^2 \frac{\Phi_{0V}}{2} \quad (\text{A.4})$$

where $d = \left| \vec{d}_{12} \right|$ is the transverse component of the distance vector $\vec{d} = \vec{x}_H - \vec{v}$ and $z = \left(\vec{d} \right)_3$ is the longitudinal component. The other components of \vec{d} can be denoted as $x = \left(\vec{d} \right)_1$ and $y = \left(\vec{d} \right)_2$. The 3D track radius R is given by the reconstructed track momentum p and the magnetic field B : $R = \frac{p}{B}$. When Φ_{0V}

A.1. Calculating the Scattering Angles

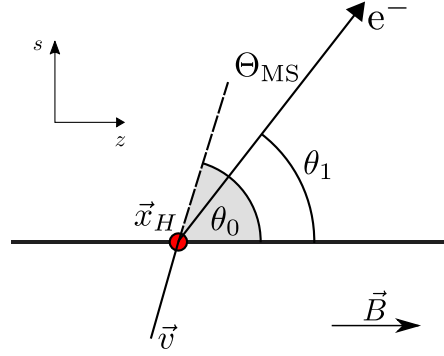


Figure A.2.: Sketch of longitudinal scattering. Since the polar angle θ is an invariant under motion in a homogeneous magnetic field, it can be assumed that the angle does not change before the particle reaches the first layer. The scattering angle Θ_{MS} is given by the difference of angles after (θ_1) and before scattering (θ_0).

has been obtained, the missing azimuthal angle φ_0 is given as

$$\phi_0 = \frac{\Phi_{0V}}{2} + \zeta \quad (\text{A.5})$$

where $\zeta := \angle \vec{d}$ denotes the azimuthal angle of the distance vector \vec{d} . Combining A.2 and A.5, the azimuthal scattering angle is finally given by

$$\Phi_{\text{MS}} = \phi_1 - \zeta - \frac{\Phi_{0V}}{2}. \quad (\text{A.6})$$

A.1.2. Longitudinal Scattering

Similar to the definition of Φ_{MS} , one can define

$$\Theta_{\text{MS}} := \theta_1 - \theta_0 \quad (\text{A.7})$$

as the difference of polar angles after and before scattering (see figure A.2). Under the assumption that no energy is lost in the scattering process, θ_0 can be expressed as

$$\cos \theta_0 = \frac{z}{R\Phi_{0V}}. \quad (\text{A.8})$$

A. Additional Calculations for the Vertex Fit

The longitudinal scattering angle is then given by

$$\Theta_{\text{MS}} = \theta_1 - \arccos \frac{z}{R\Phi_{0V}}. \quad (\text{A.9})$$

A.2. First Derivatives of Scattering Angles

The derivatives of the 2D bending angle Φ_{0V} with respect to

$$d = \sqrt{(x_H - \vec{v}_x)^2 + (y_H - \vec{v}_y)^2} \quad (\text{A.10})$$

$$= \sqrt{x^2 + y^2} \quad (\text{A.11})$$

$$\text{and } z = z_H - \vec{v}_z \quad (\text{A.12})$$

can be calculated from A.4, yielding

$$\frac{\partial \Phi_{0V}(\vec{v})}{\partial d} = \frac{\Phi_{0V}^2 d}{(\Phi_{0V}^2 R^2 - z^2) \sin \Phi_{0V} + 4z^2 \frac{\sin^2(\Phi_{0V}/2)}{\Phi_{0V}}} \quad (\text{A.13})$$

$$\frac{\partial \Phi_{0V}(\vec{v})}{\partial z} = \frac{4z \sin^2(\Phi_{0V}/2)}{(\Phi_{0V}^2 R^2 - z^2) \sin \Phi_{0V} + 4z^2 \frac{\sin^2(\Phi_{0V}/2)}{\Phi_{0V}}}. \quad (\text{A.14})$$

The derivatives $\frac{\partial \Phi_{0V}(\vec{v})}{\partial x}$ and $\frac{\partial \Phi_{0V}(\vec{v})}{\partial y}$ are obtained by substituting:

$$\frac{\partial d}{\partial x} = \frac{x}{d} \quad (\text{A.15})$$

$$\frac{\partial d}{\partial y} = \frac{y}{d}. \quad (\text{A.16})$$

Finally, the derivatives with respect to \vec{v} are obtained, using

$$K = (\Phi_{0V}^2 R^2 - z^2) \sin \Phi_{0V} + 4z^2 \frac{\sin^2(\Phi_{0V}/2)}{\Phi_{0V}}$$

A.2. First Derivatives of Scattering Angles

First Derivatives of Φ_{MS}

$$\frac{\partial \Phi}{\partial v_x} = \frac{x}{2K} \Phi_{0V}^2 - \frac{y}{d^2} \quad (\text{A.17})$$

$$\frac{\partial \Phi}{\partial v_y} = \frac{y}{2K} \Phi_{0V}^2 + \frac{x}{d^2} \quad (\text{A.18})$$

$$\frac{\partial \Phi}{\partial v_z} = \frac{2z}{K} \sin^2 \frac{\Phi_{0V}}{2} \quad (\text{A.19})$$

First Derivatives of Θ_{MS}

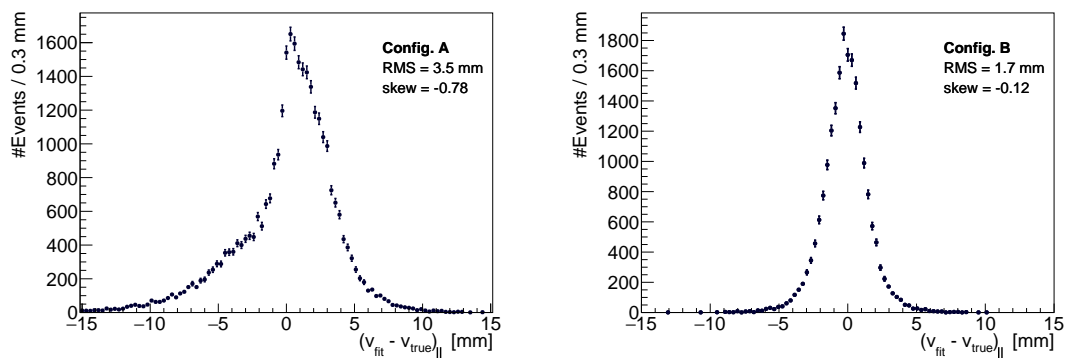
$$\frac{\partial \Theta_{\text{MS}}}{\partial v_x} = \frac{xz\Phi_{0V}}{K \sqrt{\Phi_{0V}^2 R^2 - z^2}} \quad (\text{A.20})$$

$$\frac{\partial \Theta_{\text{MS}}}{\partial v_y} = \frac{yz\Phi_{0V}}{K \sqrt{\Phi_{0V}^2 R^2 - z^2}} \quad (\text{A.21})$$

$$\frac{\partial \Theta_{\text{MS}}}{\partial v_z} = \frac{1}{\sqrt{\Phi_{0V}^2 R^2 - z^2}} \left[\frac{4z^2 \sin^2 \frac{\Phi_{0V}}{2}}{K \Phi_{0V}} - 1 \right] \quad (\text{A.22})$$

B. Additional Figures for Photons

Parallel Part of Spatial Residuals for Different Configurations



- (a) Configuration A, i.e. two transverse in- (b) Configuration A, i.e. no transverse inter-
tersections. sections.

Figure B.1.: Parallel part of the residuals of the reconstructed vertex position for photon conversion for the two possible configurations of the tracks.

Spatial Resolutions for Different Chi-Squared Cuts (Parallel Part)

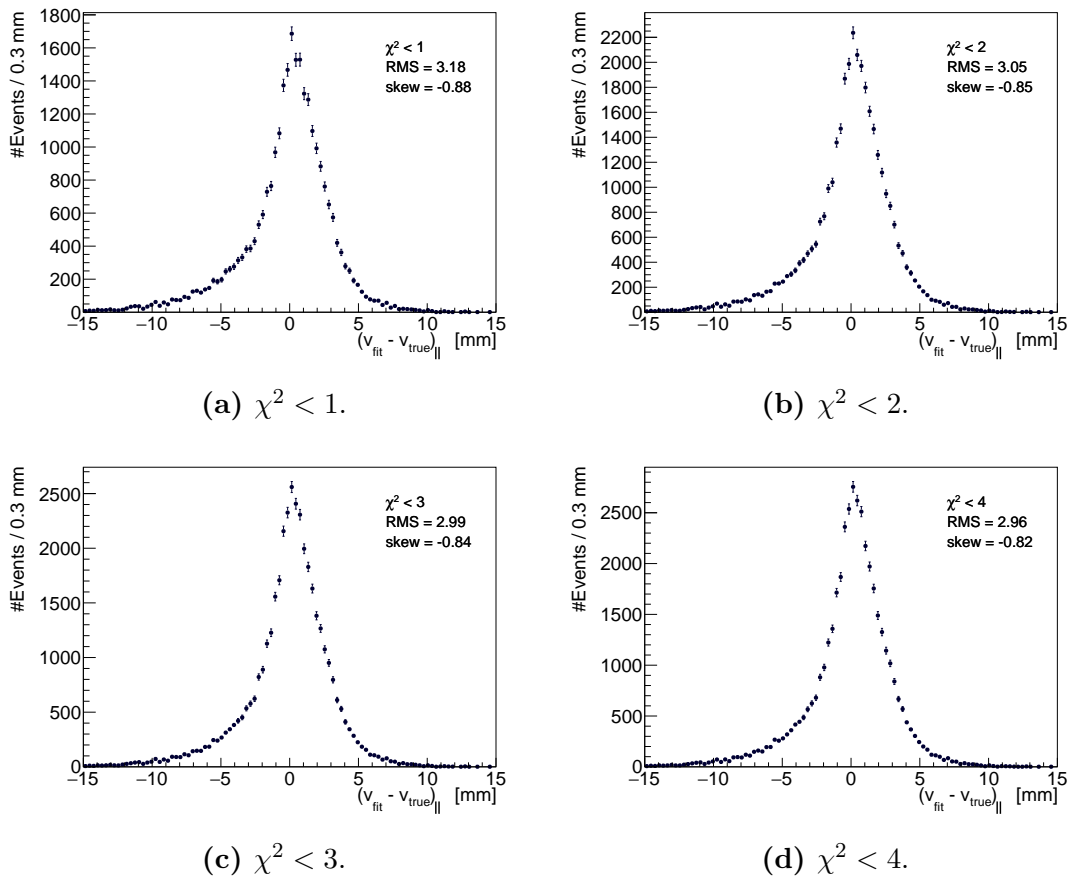
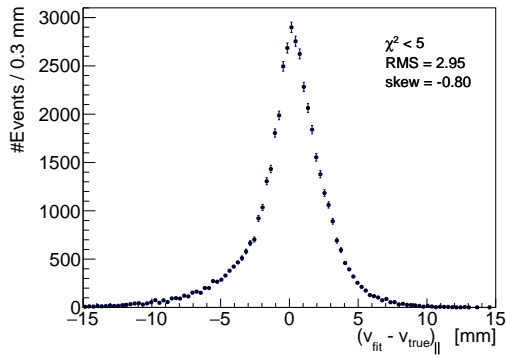
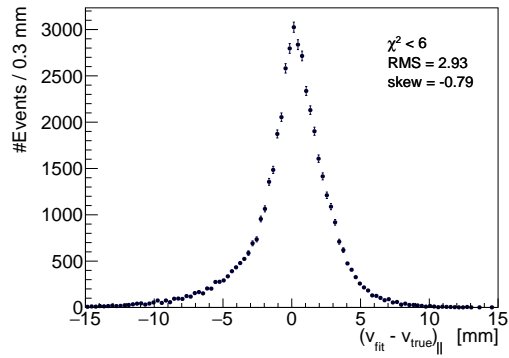


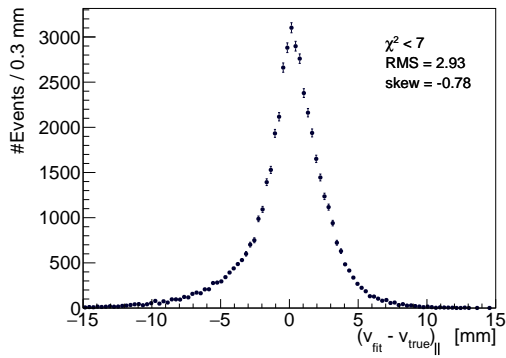
Figure B.2.: Parallel part of the residuals of the reconstructed vertex position for photon conversion for different cuts on χ^2 .



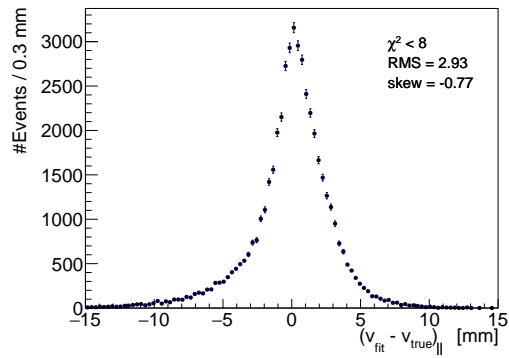
(a) $\chi^2 < 5$.



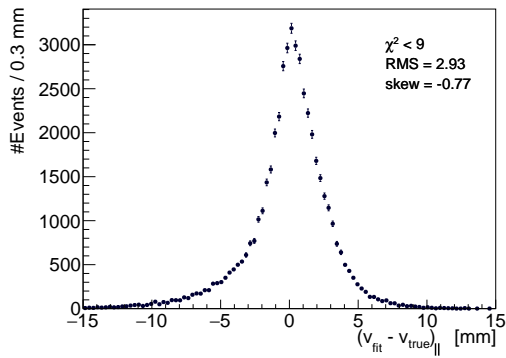
(b) $\chi^2 < 6$.



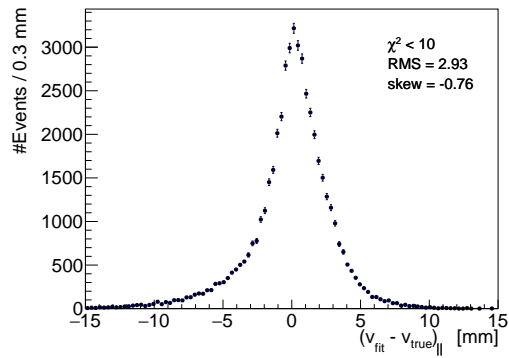
(c) $\chi^2 < 7$.



(d) $\chi^2 < 8$.



(e) $\chi^2 < 9$.



(f) $\chi^2 < 10$.

Figure B.3.: Parallel part of the residuals of the reconstructed vertex position for photon conversion for different cuts on χ^2 .

Spatial Resolutions for Different Chi-Squared Cuts (Perpendicular Part)

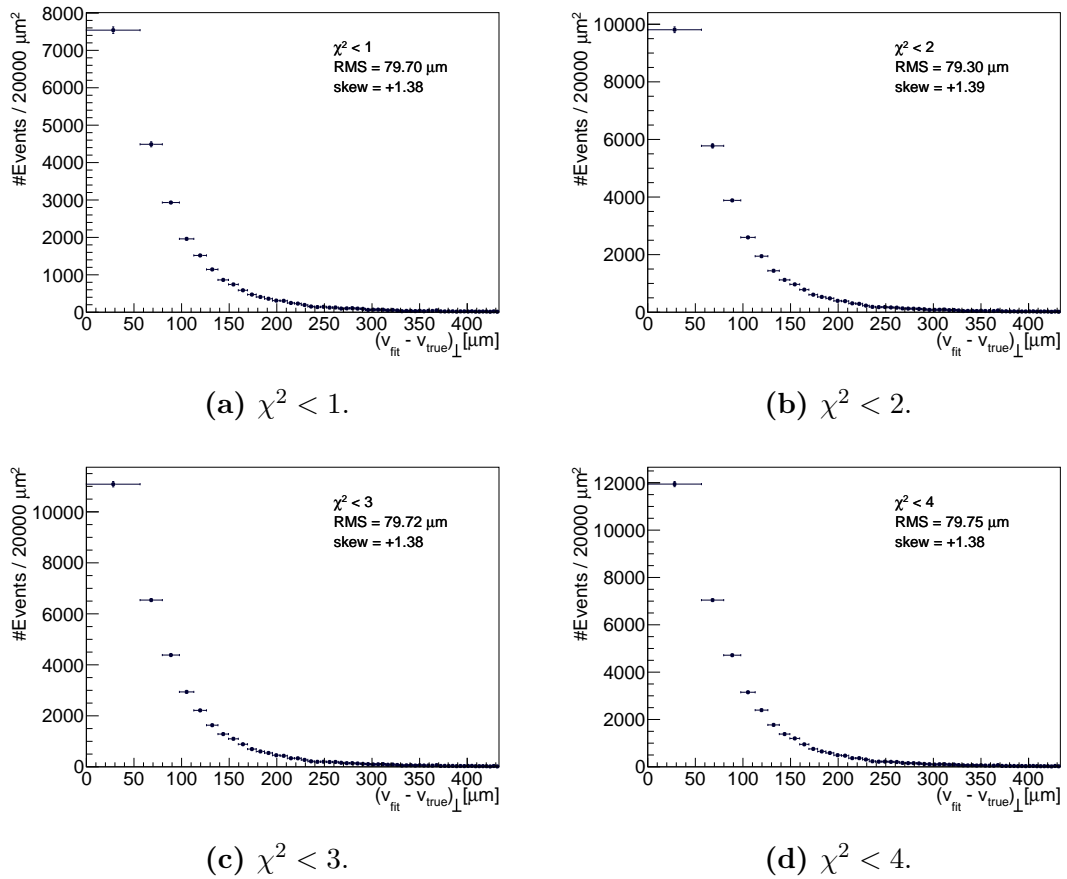
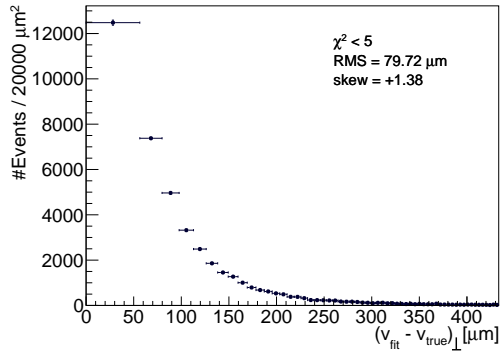
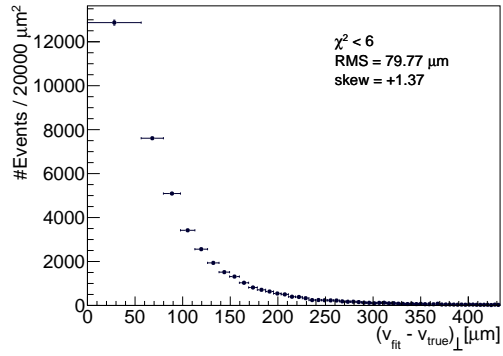


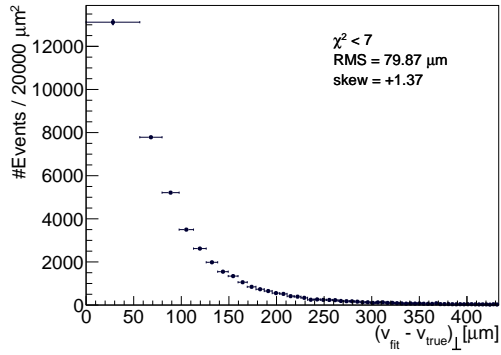
Figure B.4.: Perpendicular part of the residuals of the reconstructed vertex position for photon conversion for different cuts on χ^2 .



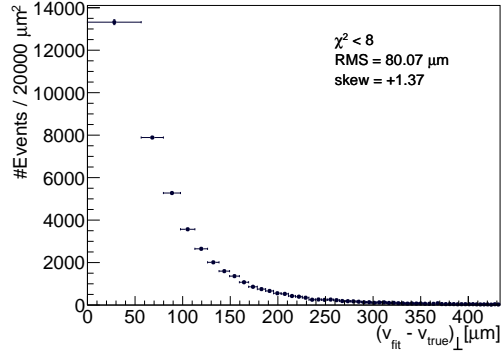
(a) $\chi^2 < 5$.



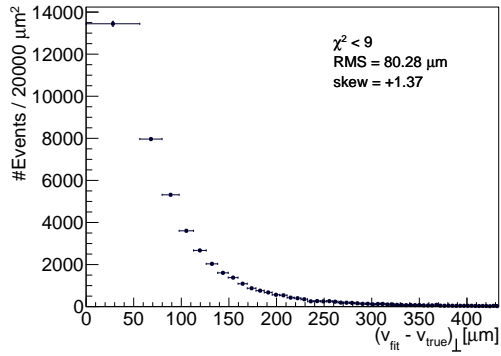
(b) $\chi^2 < 6$.



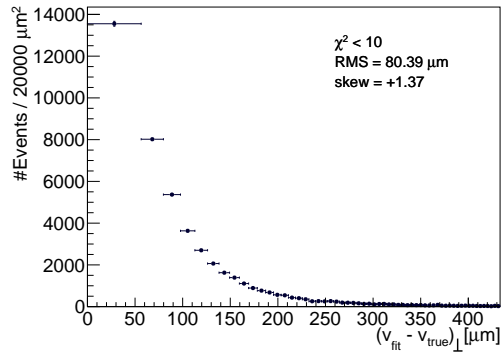
(c) $\chi^2 < 7$.



(d) $\chi^2 < 8$.



(e) $\chi^2 < 9$.



(f) $\chi^2 < 10$.

Figure B.5.: Perpendicular part of the residuals of the reconstructed vertex position for photon conversion for different cuts on χ^2 .

C. Additional Figures for Dalitz Pairs

Invariant Mass Resolution for Pions

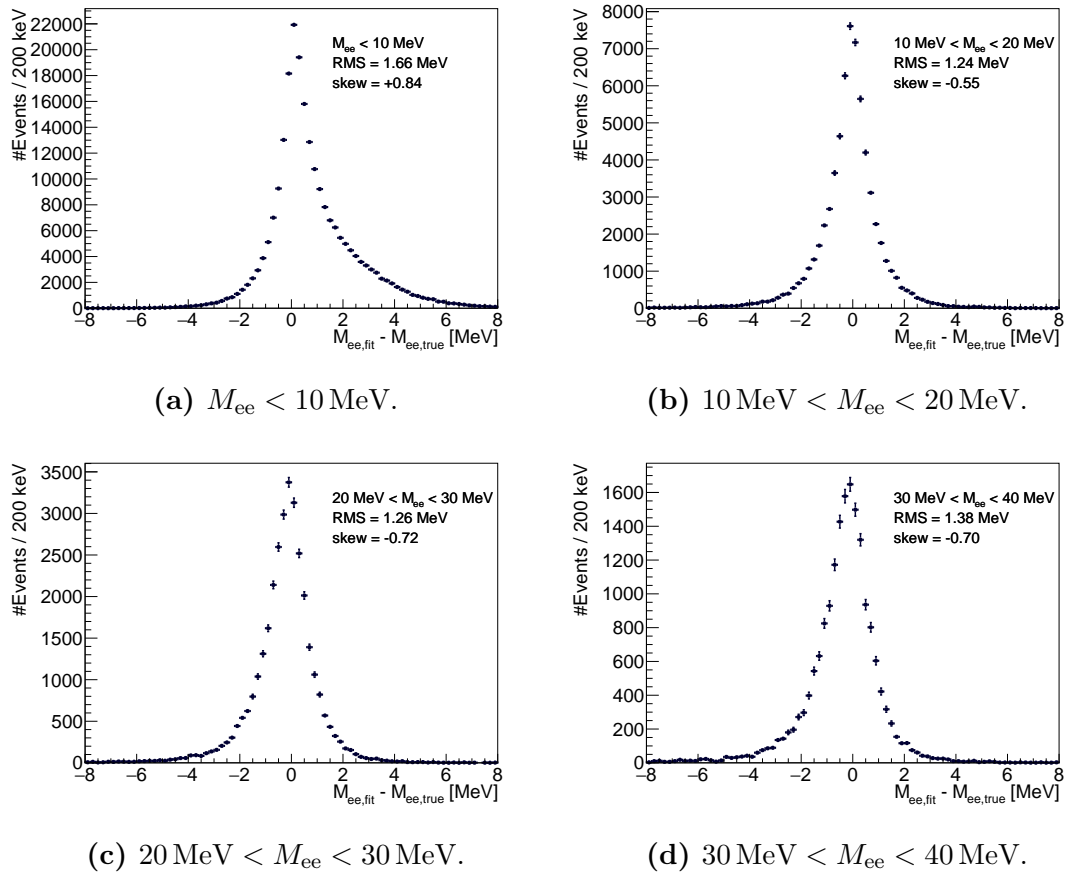
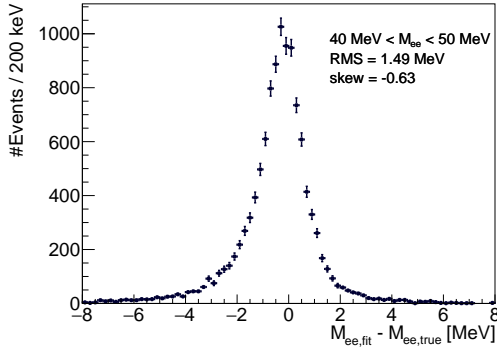
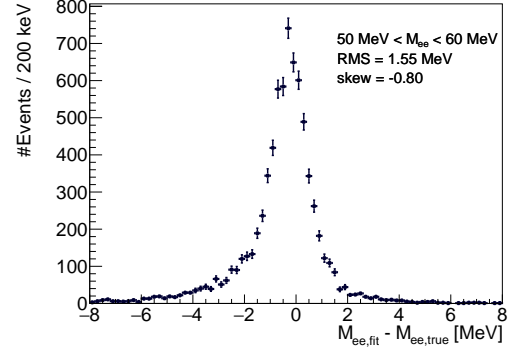


Figure C.1.: Residuals of the reconstructed invariant mass of the e^+e^- pair from Dalitz decays for invariant mass intervals up to 40 MeV.

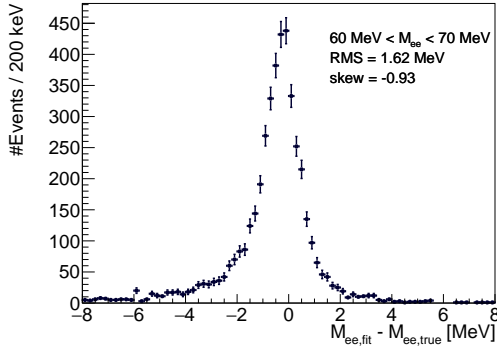
C. Additional Figures for Dalitz Pairs



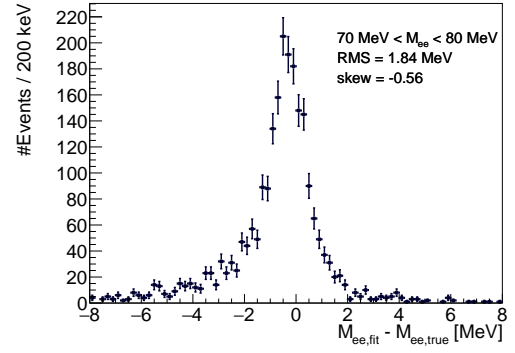
(a) 40 MeV < M_{ee} < 50 MeV.



(b) 50 MeV < M_{ee} < 60 MeV.



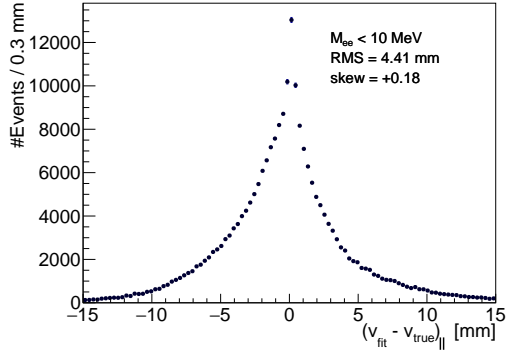
(c) 60 MeV < M_{ee} < 70 MeV.



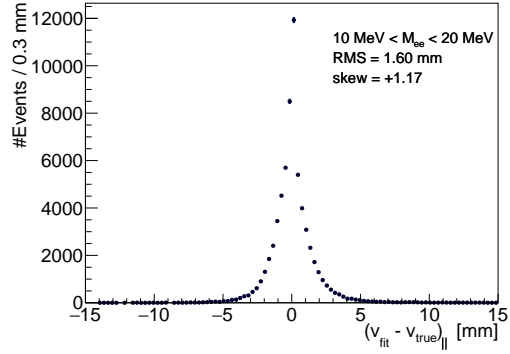
(d) 70 MeV < M_{ee} < 80 MeV.

Figure C.2.: Residuals of the reconstructed invariant mass of the e^+e^- pair from Dalitz decays for invariant mass intervals up to 80 MeV.

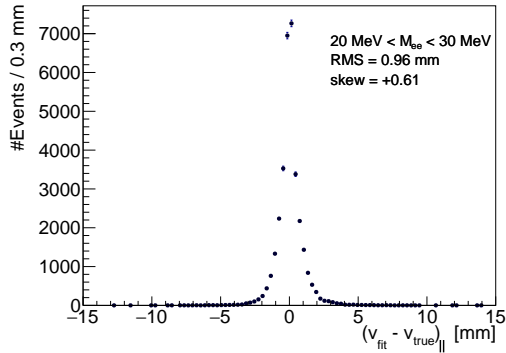
Vertex Position Residuals



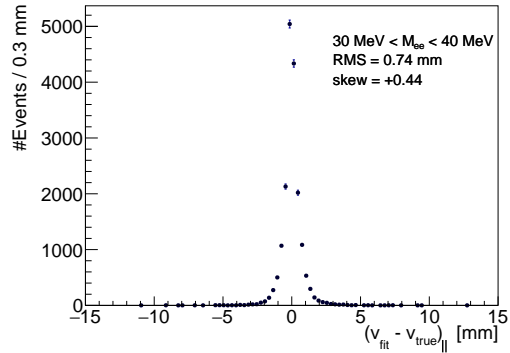
(a) $M_{ee} < 10$ MeV.



(b) $10 \text{ MeV} < M_{ee} < 20$ MeV.



(c) $20 \text{ MeV} < M_{ee} < 30$ MeV.



(d) $30 \text{ MeV} < M_{ee} < 40$ MeV.

Figure C.3.: Parallel part of the residuals of the vertex position of Dalitz decays for invariant mass intervals up to 40 MeV.

C. Additional Figures for Dalitz Pairs

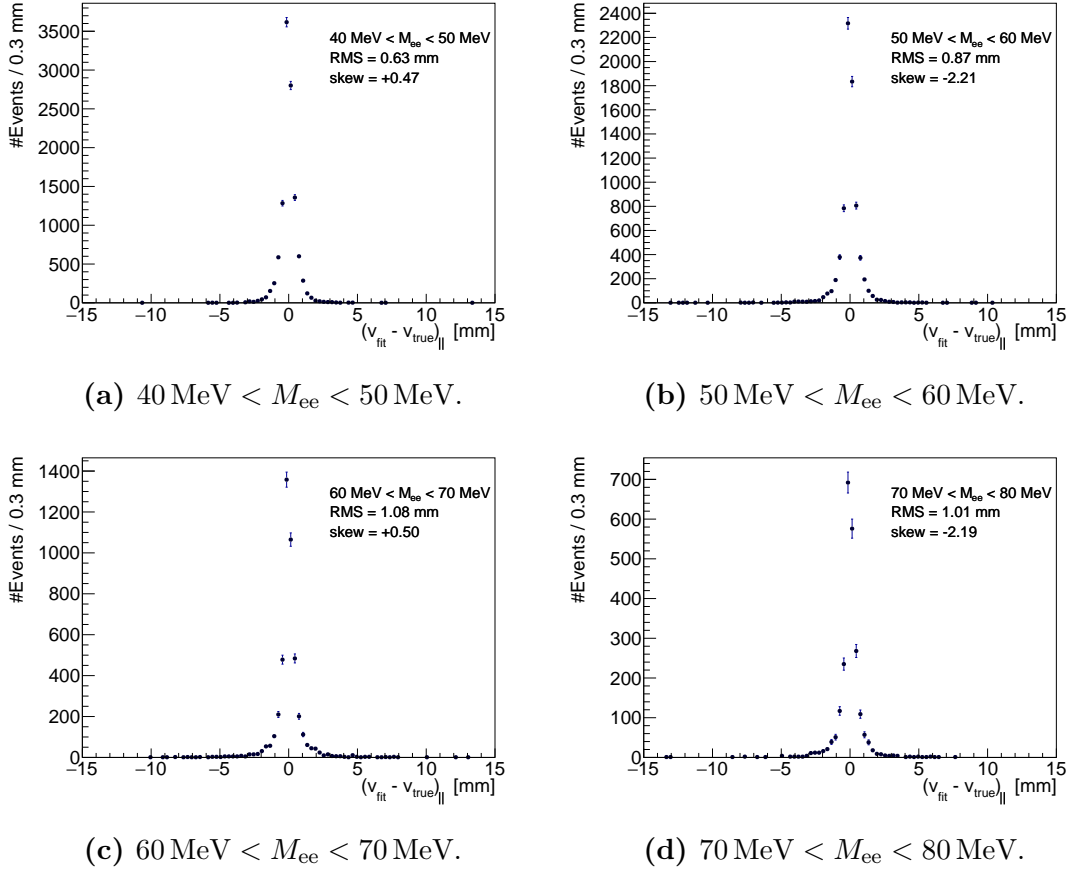
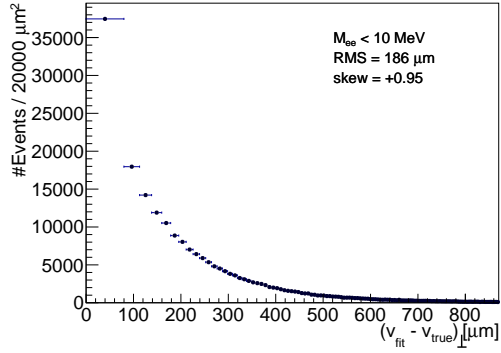
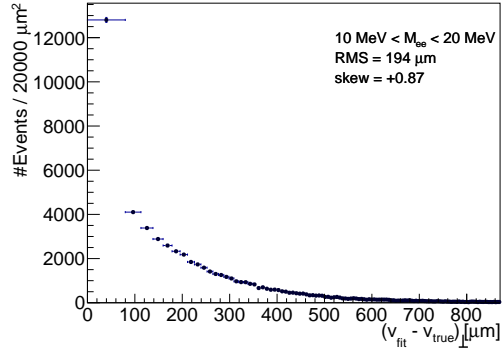


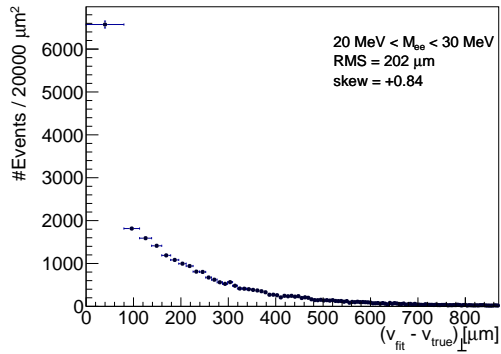
Figure C.4.: Parallel part of the residuals of the vertex position of Dalitz decays for invariant mass intervals up to 80 MeV.



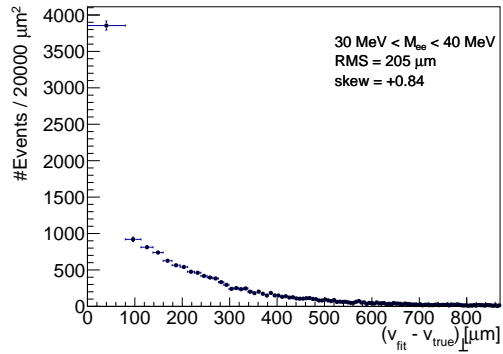
(a) $M_{ee} < 10 \text{ MeV}$.



(b) $10 \text{ MeV} < M_{ee} < 20 \text{ MeV}$.



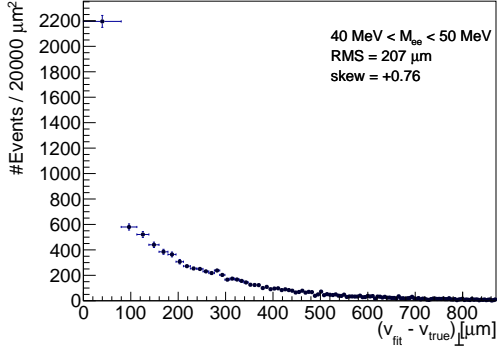
(c) $20 \text{ MeV} < M_{ee} < 30 \text{ MeV}$.



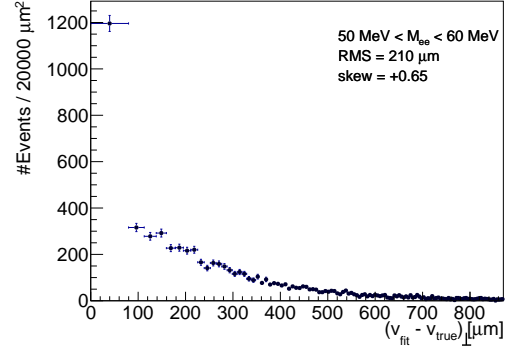
(d) $30 \text{ MeV} < M_{ee} < 40 \text{ MeV}$.

Figure C.5.: Perpendicular part of the residuals of the vertex position of Dalitz decays for invariant mass intervals up to 40 MeV. Binning is chosen such that each bin corresponds to an annulus of $20\,000 \mu\text{m}^2$.

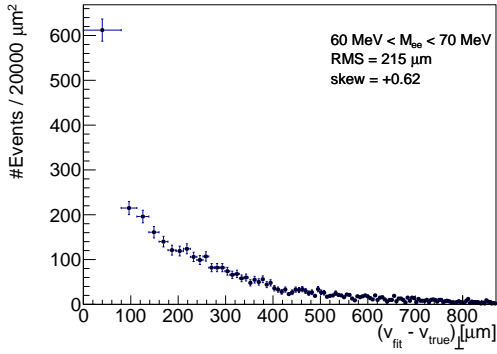
C. Additional Figures for Dalitz Pairs



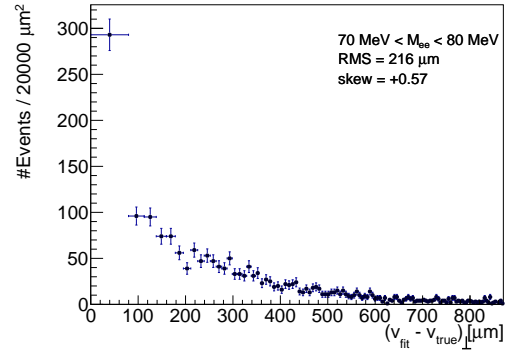
(a) $40 \text{ MeV} < M_{ee} < 50 \text{ MeV}$.



(b) $50 \text{ MeV} < M_{ee} < 60 \text{ MeV}$.



(c) $60 \text{ MeV} < M_{ee} < 70 \text{ MeV}$.



(d) $70 \text{ MeV} < M_{ee} < 80 \text{ MeV}$.

Figure C.6.: Perpendicular part of the residuals of the vertex position of Dalitz decays for invariant mass intervals up to 80 MeV. Binning is chosen such that each bin corresponds to an annulus of $20\,000 \mu\text{m}^2$.

Bibliography

- [1] H. Augustin et al. *Mu3e Experiment: Technical Design of the Phase I*. Dec. 2016.
- [2] Mark Levinson. *Particle Fever*. 2013.
- [3] Y. Fukuda et al. “Evidence for oscillation of atmospheric neutrinos”. In: *Phys. Rev. Lett.* 81 (1998), pp. 1562–1567.
- [4] F.P. An et al. “Observation of electron-antineutrino disappearance at Daya Bay”. In: *Phys.Rev.Lett.* 108 (2012), p. 171803. DOI: 10.1103/PhysRevLett.108.171803.
- [5] Q. R. Ahmad et al. “Measurement of the charged current interactions produced by B-8 solar neutrinos at the Sudbury Neutrino Observatory”. In: *Phys. Rev. Lett.* 87 (2001), p. 071301.
- [6] Mark Thomson. *Modern Particle Physics*. Cambridge, U.K.: Cambridge University Press, 2013. ISBN: 978-1-107-03426-6.
- [7] C. Patrignani et al. “Review of Particle Physics”. In: *Chin. Phys.* C40.10 (2016), p. 100001. DOI: 10.1088/1674-1137/40/10/100001.
- [8] Kaoru Hagiwara et al. “ $(g - 2)_\mu$ and $\alpha(M_Z^2)$ re-evaluated using new precise data”. In: *J. Phys.* G38 (2011), p. 085003. DOI: 10.1088/0954-3899/38/8/085003.
- [9] Mauro Raggi and Venelin Kozhuharov. “Results and perspectives in dark photon physics”. In: *Riv. Nuovo Cim.* 38.10 (2015), pp. 449–505. DOI: 10.1393/ncr/i2015-10117-9.
- [10] J. Spuller et al. “A Remeasurement of the Panofsky Ratio”. In: *Phys. Lett.* B67 (1977), pp. 479–482. DOI: 10.1016/0370-2693(77)90449-X.

Bibliography

- [11] C. Lazzeroni et al. *Measurement of the π^0 electromagnetic transition form factor slope*. Tech. rep. CERN-EP-2016-323. Geneva: CERN, Dec. 2016.
- [12] D. W. Joseph. “Electron pair creation in π^+p capture reactions from rest”. In: *Il Nuovo Cimento (1955-1965)* 16.6 (1960), pp. 997–1013. ISSN: 1827-6121. DOI: 10.1007/BF02860383.
- [13] J. R. Batley et al. “Search for the dark photon in π^0 decays”. In: *Phys. Lett. B* 746 (2015), pp. 178–185. DOI: 10.1016/j.physletb.2015.04.068.
- [14] Claus Grupen and Boris A. Shwartz. *Particle detectors*. eng. 2. ed. Cambridge monographs on particle physics, nuclear physics, and cosmology ; 26. New York, NY: Cambridge University Press, 2008. ISBN: 0-521-84006-6 ; 978-0-521-84006-4.
- [15] U. Bellgardt et al. “Search for the decay $\mu^+ \rightarrow e^+e^+e^-$ ”. In: *Nuclear Physics B* 299.1 (1988), pp. 1–6. ISSN: 0550-3213. DOI: [http://dx.doi.org/10.1016/0550-3213\(88\)90462-2](http://dx.doi.org/10.1016/0550-3213(88)90462-2).
- [16] T. Prokscha et al. “A New High-Intensity, Low-Momentum Muon Beam for the Generation of Low-Energy Muons at PSI”. In: *HFI/NQI 2004: Proceedings of the 13th International Conference on Hyperfine Interactions and 17th International Symposium on Nuclear Quadrupole Interactions (HFI/NQI 2004) Bonn, Germany, 22–27 August 2004*. Ed. by K. Maier and R. Vianden. 2005, pp. 812–815. ISBN: 978-3-540-30924-6. DOI: 10.1007/3-540-30924-1_129.
- [17] S. T. Petcov. “The Processes $\mu \rightarrow e\gamma$, $\mu \rightarrow ee\bar{e}$, $\nu' \rightarrow \nu\gamma$ in the Weinberg-Salam Model with Neutrino Mixing”. In: *Sov. J. Nucl. Phys.* 25 (1977). [Erratum: *Yad. Fiz.*25,1336(1977)], p. 340.
- [18] S. Bachmann et al. *Letter of Intent for an Experiment to Search for the Decay $\mu \rightarrow eee$* . 2012.
- [19] Sebastian Schenk. “A Vertex Fit for Low Momentum Particles in a Solenoidal Magnetic Field with Multiple Scattering”. Bachelor Thesis. Physikalisches Institut der Universität Heidelberg, 2012.

- [20] Rashid M. Djilkibaev and Rostislav V. Konoplich. “Rare Muon Decay $\mu^+ \rightarrow e^+e^-e^+\nu_e\bar{\nu}_\mu$ ”. In: *Phys. Rev.* D79 (2009), p. 073004. DOI: 10.1103/PhysRevD.79.073004.
- [21] Yannick Ulrich. *Monte Carlo Programs for Muon Decays at NLO*. 2016. URL: <https://indico.psi.ch/contributionDisplay.py?contribId=257&sessionId=25&confId=3914>.
- [22] Ivan Perić. “A novel monolithic pixelated particle detector implemented in high-voltage {CMOS} technology”. In: *Nuclear Instruments and Methods in Physics Research Section A: Accelerators, Spectrometers, Detectors and Associated Equipment* 582.3 (2007), pp. 876–885. ISSN: 0168-9002. DOI: <http://dx.doi.org/10.1016/j.nima.2007.07.115>.
- [23] A. M. Baldini et al. “Search for the lepton flavour violating decay $\mu^+ \rightarrow e^+\gamma$ with the full dataset of the MEG experiment”. In: *The European Physical Journal C* 76.8 (2016), p. 434. ISSN: 1434-6052. DOI: 10.1140/epjc/s10052-016-4271-x.
- [24] A. M. Baldini et al. *MEG Upgrade Proposal*. 2013.
- [25] Yoshitaka Kuno and Yasuhiro Okada. “Muon decay and physics beyond the standard model”. In: *Rev. Mod. Phys.* 73 (2001), pp. 151–202. DOI: 10.1103/RevModPhys.73.151.
- [26] André Schöning. *Mu3e-Gamma Proposal*. Mu3e External Meeting, 15 Feb 2017.
- [27] Chih-hsiang. Cheng, Bertrand Echenard, and David G. Hitlin. “The next generation of $\mu \rightarrow e\gamma$ and $\mu \rightarrow 3e$ CLFV search experiments”. In: *Proceedings, Community Summer Study 2013: Snowmass on the Mississippi (CSS2013): Minneapolis, MN, USA, July 29-August 6, 2013*. 2013.
- [28] *piE1 beam line*. March 2017. URL: <https://www.psi.ch/smus/pie1>.
- [29] *piM1 beam line*. March 2017. URL: http://aea.web.psi.ch/beam2lines/beam_pim1.html.

Bibliography

- [30] Niklaus Berger et al. “A new three-dimensional track fit with multiple scattering”. In: *Nuclear Instruments and Methods in Physics Research Section A: Accelerators, Spectrometers, Detectors and Associated Equipment* 844 (2017), pp. 135–140. ISSN: 0168-9002. DOI: <http://dx.doi.org/10.1016/j.nima.2016.11.012>.
- [31] Caren Kresse. “Track Reconstruction of Photon Conversion Electrons from Displaced Vertices in the Mu3e Detector”. Master Thesis. 2017.
- [32] M. Valentan, M. Regler, and R. Fruhwirth. “Generalization of the Gluckstern formulas II: Multiple scattering and non-zero dip angles”. In: *Nucl. Instrum. Meth.* A606 (2009), pp. 728–742. DOI: [10.1016/j.nima.2009.05.024](https://doi.org/10.1016/j.nima.2009.05.024).
- [33] Sebastian Schenk Moritz Kiehn. *Scattering Vertex Fit Notes*. Internal Note. 2016.
- [34] G. Cowan. *Statistical Data Analysis*. Oxford science publications. Clarendon Press, 1998. ISBN: 9780198501558. URL: <https://books.google.de/books?id=ff8ZyW0n1JAC>.
- [35] Moritz Kiehn. “Pixel Sensor Evaluation and Track Fitting for the Mu3e Experiment”. PhD thesis. 2016.
- [36] William H. Press et al. *Numerical Recipes 3rd Edition: The Art of Scientific Computing*. 3rd ed. New York, NY, USA: Cambridge University Press, 2007. ISBN: 0521880688, 9780521880688.
- [37] *MINUIT*. URL: <https://root.cern.ch/root/html534/TMinuit.html>.

Danksagungen

An dieser Stelle möchte ich mich gern bei all denjenigen bedanken, die mich im letzten Jahr unterstützt haben.

Zuallererst möchte ich Herrn Prof. André Schöning dafür danken, dass er mir dieses interessante Thema Masterarbeit angeboten hat. Insbesondere möchte ich mich dafür bedanken, dass er es mir ermöglicht hat, einen Vortrag beim externen Kollaborationsmeeting in Wengen zu halten und diverse Workshops und Konferenzen zu besuchen.

Ganz besonders möchte ich Ann-Kathrin Perrevoort für ihre Betreuung und konstante Hilfsbereitschaft bedanken. Ohne ihre Unterstützung jeglicher Art wäre diese Arbeit nicht möglich gewesen.

Bei Caren Kresse möchte ich mich für das tolle Büroklima bedanken, wenn wir zusammen über gemeinsame Probleme gerätselt haben, oder uns die Probleme des jeweils anderen zu eigen gemacht haben. Es war immer hilfreich, jemanden neben sich sitzen zu haben, dem keine Frage zu doof war um darüber zu diskutieren.

Außerdem möchte ich mich bei allen Mitgliedern von Mu3e bedanken, die immer hilfsbereit waren und für ein tolles Arbeitsklima gesorgt haben. Ob aus Heidelberg, aus Mainz oder aus Zürich, ob am Kaffeetisch, im Softwaremeeting oder in Wengen, das letzte Jahr war wirklich schön in dieser Gruppe. Insbesondere danke ich denjenigen, die diese Arbeit Korrektur gelesen haben.

Ein großer Dank gebührt selbstverständlich auch meiner Familie, die mich über das ganze Studium hinweg immer unterstützt hat.

Zuletzt möchte ich mich auch bei Alex Pösch dafür bedanken, dass er selbst zu später Stunde noch seine Hilfe bei der Fertigstellung dieser Masterarbeit angeboten hat.

Erklärung:

Ich versichere, dass ich diese Arbeit selbstständig verfasst habe und keine anderen als die angegebenen Quellen und Hilfsmittel benutzt habe.

Heidelberg, den (Datum)